High-Resolution MHD Spectroscopy of External Kinks in a Tokamak Plasma

Daisuke Shiraki

Columbia University

2012

ABSTRACT

High-Resolution MHD Spectroscopy of External Kinks in a Tokamak Plasma

Daisuke Shiraki

This thesis describes the first results of passive and active MHD spectroscopy experiments on the High Beta Tokamak-Extended Pulse (HBT-EP) device using a new array of magnetic diagnostics and coils. The capabilities of the HBT-EP experiment are significantly extended with the installation of a new adjustable conducting wall, high-power modular control coil arrays, and an extensive set of 216 magnetic sensors that allow simultaneous high-resolution detection of multimode MHD phenomena. The design, construction, and calibration of this system are described. The capability of this new magnetic diagnostic set is demonstrated by biorthogonal decomposition analysis of passive measurements of rotating resistive wall modes (RWMs). A strong multimode effect is detected for the first time in HBT-EP plasmas consisting of the simultaneous existence of $m/n = 3/1$ and $6/2$ RWMs which cause the plasma to evolve in a non-rigid multimode manner. Additional mode numbers as high as $n = 3$ are also observed. Active MHD spectroscopy experiments using a "phase-flip" resonant magnetic perturbation (RMP) are able to excite a clear three-dimensional response. By adjusting the helicity of the magnetic field applied by the control coils, the driven plasma response is shown to be predominantly resonant field amplification. When the amplitude of the applied field is not too large, the driven resonant response appears linear, independent of the presence of background MHD phenomena and consistent with the predictions of single-helicity modeling of kink mode dynamics. The spatial structures of both the naturally rotating kink mode and the externally driven response are observed to be identical, while the temporal dynamics are consistent with the independent evolution of each mode. The phase-flip driven plasma response is measured as a function of edge safety factor, plasma rotation, and the amplitude of the applied magnetic perturbation. As the RMP amplitude increases, the plasma response is shown to be linear, saturated, and ultimately, disruptive.

Contents

List of Figures

List of Tables

Acknowledgments

I am indebted to many people for the completion of this thesis. I am grateful to Professors Mike Mauel and Jerry Navratil for taking me on as a student in their research group. Working on HBT-EP over the last six years has been an incredible learning experience, and I feel that it has prepared me well for my future career. I would like to thank Jeremy Hanson and Royce James for passing on their knowledge of the experiment to me, and for allowing me to interfere with their work to begin my own research projects. I have enjoyed many helpful discussions about my work with Dave Maurer over the years, and these were always helpful and encouraging during the stressful and frustrating times which are routine occurrences in scientific research. The technical help of Nick Rivera and Jim Andrello were also essential parts of completing my thesis work, and I owe many of my experimental skills to them. I would also like to thank Jim Bialek for his time over the years providing VALEN results in support of this work. Of course, this work was not solely an individual effort, and I thank my fellow HBT-EP students for their role in helping me complete this thesis. Outside of my scientific work, I am grateful to Paul Brenner, Mike Frei, Mary Lee, and Adriana Navarro-Chan for the wonderful times at Apt 5B, which was such an important part of the last six years for me. I would also like to thank all of my friends both here and at home (of which there are too many to list), who have made my time here in New York so memorable and enjoyable. I doubt that my time here would have been worth it without all of these great memories. And finally, I would like to thank my parents and family for their continual support and encouragement in pursuing a PhD, and this thesis is dedicated to them.

Chapter 1

Introduction

The promise of controlled nuclear fusion as a potential energy source has motivated much of plasma physics research in the last 60 years. Currently, the plasma physics community is in the process of building the ITER device, the first experiment capable of confining a plasma dominated by alpha particle heating [1]. This leap to the burning plasma regime will require expansion of the achievable plasma operating space, for which equilibrium, stability, and transport considerations require detailed understanding and control of 3D fields in tokamak plasmas. The work in this thesis is motivated by this need for improved understanding of 3D tokamak physics.

1.1   Fusion

The production of energy from the fusion of light nuclei is an attractive alternative to today's energy technologies. Based on considerations of fuel abundancy and practically achievable temperatures, the most likely candidate reaction is between the stable heavy isotopes of hydrogen:

$$D + T \rightarrow He + n + 17.6 \text{ MeV} \tag{1.1}$$

Achieving significant rates of this nuclear reaction by overcoming the Coulomb repulsion between the D and T ions requires temperatures of $\gtrsim 10$ keV, even after accounting for quantum tunneling and the high-energy tail of the Maxwellian distribution. At such high temperatures ($\sim 10^8$ K), the hydrogen gas is fully ionized and in the plasma state. One important parameter of such a plasma is the energy confinement time, defined as the ratio of the total energy to the power loss: $\tau_E \equiv W_{th}/P_{loss}$. Then, a simple power balance analysis [2] shows that a minimum condition for self-sustained heating of a DT plasma is given by:

$$n\tau_E > 1.5 \times 10^{20} \text{ s/m}^3 \tag{1.2}$$

where n is the ion density of the plasma. This is known as the Lawson criterion for ignition. A slightly more useful form of this condition, for the temperatures T in our range of interest, is given by:

$$nT\tau_E > 5 \times 10^{21} \text{ keV·s/m}^3 \tag{1.3}$$

although the exact value on the right hand side will depend on the details of the temperature and density profiles of the plasma. This condition for the "fusion triple product" could be met, for example, with values of $n = 10^{20}$ m^{-3}, $T = 10$ keV, and $\tau_E = 5$ s. Each of these experimental values have been achieved individually, but the challenge remains to achieve all three conditions simultaneously. Nonetheless, the achieved fusion triple product has increased by 6 orders of magnitude over the last 60 years of fusion research [2] and remains only one order of magnitude away from reaching the burning plasma regime.

1.2 Magnetic Confinement

The extreme temperatures of fusion plasmas precludes the confinement of such plasmas by any material means. Fortunately, the Lorentz interaction ($\vec{F} = q\vec{v} \times \vec{B}$) between charged particles and magnetic fields makes it possible to magnetically confine such plasmas. A charged particle in a uniform magnetic field is confined in the perpendicular direction to

within a Larmor radius $r_L = \dfrac{mv_\perp}{qB}$, so that only parallel confinement along the field line is needed. The obvious solution of bending the field lines into circles to confine a toroidal plasma achieves this since the field lines close on themselves, but the resulting curvature and non-uniformities in field strength introduce particle drifts across the field lines. It is possible to have these particle drifts average out to zero if the field lines are made to spiral helically rather than in simple circles. This helical property of the confining magnetic field is known as rotational transform, and most magnetic confinement concepts rely on this to achieve equilibrium.

When the rotational transform is created by a combination of fields generated by external coils and by a plasma current driven in the toroidal direction (the long way around the torus), this configuration is known as a tokamak. This configuration is shown in Figure 1.1. Note
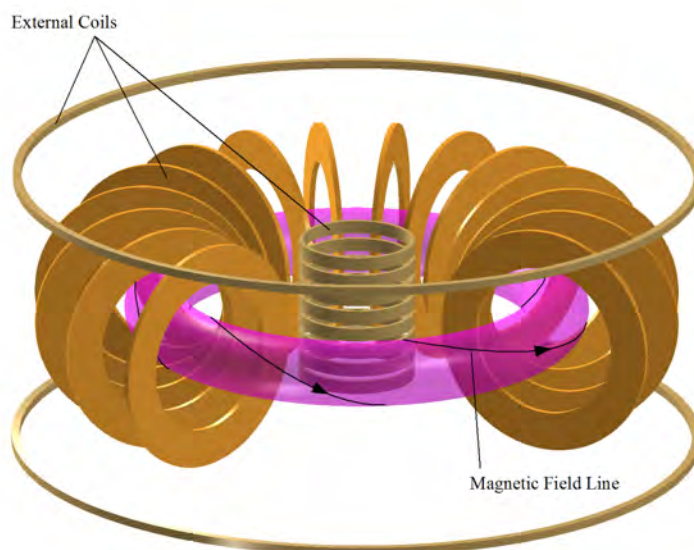
Figure 1.1: Tokamak confinement geometry, which is an axisymmetric configuration.

that the nominal tokamak plasma is axisymmetric. Due to its early success in confinement, the tokamak is currently the most developed and well-studied magnetic confinement concept.

The pitch of a helical field line in a tokamak plasma is measured by the safety factor, q,

which is the ratio of the number of times a field line travels around the plasma toroidally to the number of times it travels poloidally (the short way around the torus). As its name implies, higher values of q often leads to better stability of the plasma. However, under certain conditions, rational values of $q = m/n$ inside or near the plasma edge can lead to resonant instabilities. Thus the safety factor plays an important role in determining the stability limits in tokamaks.

Another important factor is the plasma beta, defined as the ratio of kinetic pressure to magnetic pressure:

$$\beta = \frac{p}{B^2/2\mu_0} \tag{1.4}$$

which is a measure of the efficiency of magnetic confinement. Since the fusion power density at fixed B scales as β^2, it is desirable to operate at high beta. However, the onset of instability places limits on the achievable plasma beta. Many of these instabilities can be understood by modeling the plasma as a single conducting fluid, a theory known as magnetohydrodynamics (MHD). Many such MHD instabilities present stability limits, but the external kink mode often places the most stringent beta limit on tokamak plasmas [3]. In this instability, the edge region of the plasma suffers a helical distortion with poloidal and toroidal mode numbers m and n which satisfy the resonance condition $q = m/n$ at some surface near the plasma edge. An example of a $m/n = 3/1$ perturbation is shown in Figure 1.2. When the equilibrium becomes unstable to the external kink, this 3D perturbation grows very rapidly (usually over several microseconds) and leads to a loss of confinement and a termination of the plasma, in an event known as a disruption. However, the presence of a nearby conducting wall will tend to stabilize the external kink due to induced eddy currents which oppose the growth of the perturbation. It is only the decay of these eddy currents on the resistive timescale of the wall (often on the order of milliseconds), which allows the mode to grow. In such cases, the instability is referred to as the Resistive Wall Mode (RWM) [4].

The onset of these external kinks was observed [5] to limit the plasma beta to the empirical
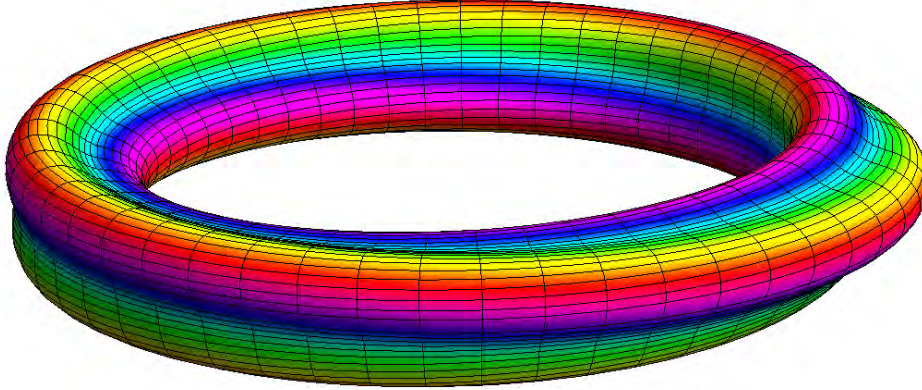
Figure 1.2: A $m/n = 3/1$ perturbation to an axisymmetric equilibrium.

limit:

$$\beta(\%) < 3.5 I_p/aB \ [\text{MA/m·T}] \tag{1.5}$$

where I_p is the plasma current, a is the plasma minor radius, and B is the toroidal field. Such scalings, named after its discoverer, are called Troyon scalings. Thus the normalized plasma beta $\beta_N = \dfrac{\beta(\%)}{I_p/aB}$ is introduced, with the resulting beta limit expressed as $\beta_N < 3.5$. Much of the research in MHD control today is in extending this type of beta limit, often through the use of 3D fields.

1.3   3D Fields in Tokamaks

Many theoretical [6, 7, 8] and experimental [9, 10, 11] studies have shown that the application of an appropriately phased 3D field through magnetic feedback control can reduce or even suppress the external kink entirely. A successful burning plasma experiment will require operation at high β_N, making the physics of magnetic feedback crucial.

Even when plasmas operate below maximum beta, 3D fields can be useful for the study of the plasma through its MHD modes. This technique is known as MHD spectroscopy [12, 13],

and can include passive MHD spectroscopy which passively measures MHD modes, as well as active MHD spectroscopy which excites a MHD response by probing the plasma with an external field. These techniques have been used to measure the plasma's approach towards RWM stability boundaries [14, 15] or to test models of 3D tokamak equilibria [16, 17].

In addition to feedback and MHD spectroscopy of RWMs, topics ranging from Edge Localized Mode control [18, 19], neoclassical tearing mode control [20, 21], error-field correction [22, 23, 24], rotation physics [25, 26], and disruption mitigation [27] make 3D fields in tokamaks an essential topic for the ability to access the burning plasma regime.

1.4 HBT-EP Experiment

The High Beta Tokamak-Extended Pulse (HBT-EP) experiment, shown in Figure 1.3, studies the physics and control of beta limiting instabilities such as the external kink. It is a small,
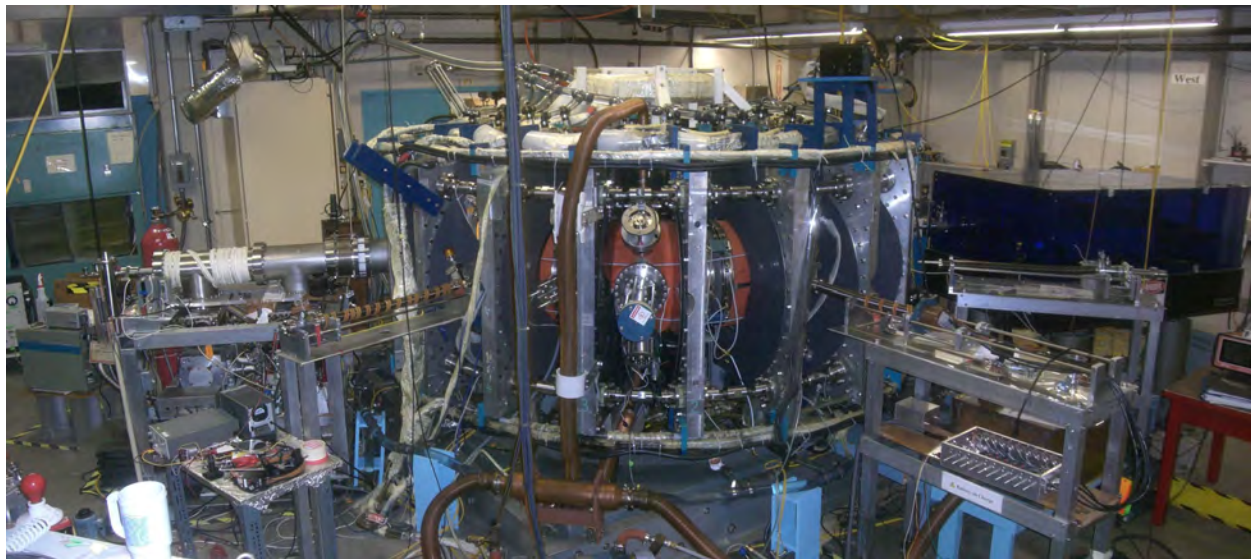
Figure 1.3: The HBT-EP experiment.

high aspect-ratio, ohmically heated tokamak with a close-fitting conducting wall for passive stabilization of fast MHD instabilities [28]. The plasma has a circular cross-section defined by two sets of fixed poloidal limiters. The HBT-EP experiment is unique because of its

adjustable conducting wall, which can be moved relative to the plasma surface in order to change the plasma-wall coupling and the resulting RWM growth rate [29]. Typical values of key experimental parameters are summarized in Table 1.1.

Parameter		Typical Values
Plasma current	I_p	15 kA
Electron temperature	T_e	100 eV
Electron density	n_e	10^{19} m^{-3}
Toroidal field	B_T	0.33 T
Major radius	R	0.92 m
Aspect ratio	R/a	6
Pulse length	τ	6 ms

Table 1.1: Typical HBT-EP experimental parameters.

The current diagnostic set on HBT-EP includes an extensive set of 216 Mirnov coils, plasma current and poloidal Fourier harmonic Rogowski coils, 7 poloidal flux loops, a loop voltage detector, a soft X-ray diode with a midplane chord view, optical spectrometer, a 20-channel D_α photodiode array, and a 20 element internal magnetic probe. HBT-EP also has three independent sets of 40 control coils, for the application of external fields in open-loop programming and closed-loop feedback configurations. Induced currents in these control coils allow additional measurements of fluctuating radial fields. Finally, a movable bias probe allows the control of the plasma rotation at the edge by exerting a $j \times B$ torque on the plasma.

Chapter 2

Physics of the External Kink Mode

The passive and active MHD spectroscopy work in this thesis study the current driven external kink mode. Many of the properties of these external kinks can be understood through ideal MHD stability analysis. Ideal MHD theory and linear stability analysis of the kink mode are reviewed, and the properties of the external kink which can be determined from this theory are described. Finally, a more detailed model for kink mode dynamics developed by Fitzpatrick and Aydemir, combined with the Boozer formalism for feedback equations, is presented for modeling of external kinks in HBT-EP plasmas.

2.1 Ideal MHD

Ideal MHD theory [30] has been extremely successful in predicting the stability limits of tokamak plasmas as well as many other magnetic confinement schemes. The MHD model is the theory of conducting fluids coupled with electromagnetic fields, which can be derived as a linear combination of individual fluid equations for the electron and ion species. The equations of ideal MHD are:

Mass conservation:
$$\frac{\partial \rho}{\partial t} + \vec{\nabla} \cdot (\rho \vec{v}) = 0 \tag{2.1}$$

Momentum conservation:
$$\frac{d\vec{v}}{dt} = -\vec{\nabla} p + \vec{j} \times \vec{B} \tag{2.2}$$

Energy conservation:
$$\frac{d}{dt} \left(\frac{p}{\rho^\gamma} \right) = 0 \tag{2.3}$$

Generalized Ohm's law:
$$\vec{E} + \vec{v} \times \vec{B} = 0 \tag{2.4}$$

Low frequency Maxwell's eqns:
$$\vec{\nabla} \times \vec{E} = -\frac{\partial \vec{B}}{\partial t} \tag{2.5}$$

$$\vec{\nabla} \times \vec{B} = \mu_0 \vec{j} \tag{2.6}$$

$$\vec{\nabla} \cdot \vec{B} = 0 \tag{2.7}$$

where $\frac{d}{dt} = \frac{\partial}{\partial t} + \vec{v} \cdot \vec{\nabla}$ is the total derivative which gives the rate of change of quantities in the fluid frame. The variables of the model are the fluid mass density ρ, pressure p, fluid velocity $\vec{v}$, current density $\vec{j}$, the electric field $\vec{E}$, and the magnetic field $\vec{B}$. γ is the ratio of specific heats, usually taken to be 5/3. The generalized Ohm's Law gives the electric field in the reference frame of the (non-relativistically) moving fluid, which is zero for the perfectly conducting fluid modeled by ideal MHD. Thus Equation 2.2 says that the dynamics of the ideal MHD fluid are governed by a balance between inertial, pressure, and magnetic forces.

MHD equilibrium for a static ($\vec{v} = 0$) plasma is described by the time-independent limit of the MHD equations:

$$\vec{\nabla} p = \vec{j} \times \vec{B} \tag{2.8}$$

$$\vec{\nabla} \times \vec{B} = \mu_0 \vec{j} \tag{2.9}$$

$$\vec{\nabla} \cdot \vec{B} = 0 \tag{2.10}$$

Such equilibria are necessarily in force-balance, but the resulting solution may or may not be a stable one. The essential problem of MHD stability takes the form of perturbation theory on these equilibrium solutions, to determine the linear stability of the configuration.

2.2 Stability of the External Kink

Basic MHD stability theory is discussed here inasmuch as it explains the properties of the external kink mode. A far more complete treatment of the subject can be found in [30] and [31].

Linear stability analysis consists of expansion of all variables in the form $p = p_0 + p_1$ or $\vec{j} = \vec{j}_0 + \vec{j}_1$, where the zeroth order terms satisfy MHD equilibrium

$$\vec{\nabla} p_0 = \vec{j}_0 \times \vec{B}_0 \tag{2.11}$$

$$\vec{\nabla} \times \vec{B}_0 = \mu_0 \vec{j}_0 \tag{2.12}$$

$$\vec{\nabla} \cdot \vec{B}_0 = 0 \tag{2.13}$$

and the first order terms represent a small perturbation of this equilibrium. Then each of Equations 2.1-2.7 are expanded so that, for example, the statement of momentum conservation (Equation 2.2) becomes:

$$(\rho_0 + \rho_1)\frac{d(\vec{v}_0 + \vec{v}_1)}{dt} = -\vec{\nabla}(p_0 + p_1) + (\vec{j}_0 + \vec{j}_1) \times (\vec{B}_0 + \vec{B}_1) \tag{2.14}$$

The terms of each such expansion which are first order in the perturbation are kept. We define the displacement vector $\vec{\xi}$ by the relation $\vec{v}_1 = \frac{\partial \vec{\xi}}{\partial t}$, so that Equation 2.14 becomes:

$$\rho\frac{d^2\vec{\xi}}{dt^2} = -\vec{\nabla} p_1 + \vec{j} \times \vec{B}_1 + \vec{j}_1 \times \vec{B} \tag{2.15}$$

where the "0" subscripts for the equilibrium quantities have been dropped. All other first order terms besides $\vec{\xi}$ are then expressed in terms of $\vec{\xi}$ using the linearized forms of the other MHD equations, to give the linearized momentum equation entirely in terms of the displacement:

$$\rho\frac{d^2\vec{\xi}}{dt^2} = \vec{F}(\vec{\xi}) \tag{2.16}$$

where the resulting $\vec{F}$ is called the force operator. Then the change in potential energy of

the system due to the displacment $\vec{\xi}$ is:

$$\delta W(\vec{\xi}) = -\frac{1}{2} \int \vec{F}(\vec{\xi}) \cdot \vec{\xi} d^3 x \qquad (2.17)$$

If this is negative for any $\vec{\xi}$, then that displacement will grow exponentially and the original zeroth order equilibrium is unstable. This statement of the stability problem is known as the Energy Principle. The change in potential energy δW can be further divided into fluid, surface, and vacuum terms: $\delta W = \delta W_F + \delta W_S + \delta W_V$, where the δW_F can be written in the intuitive form:

$$\delta W_F = \frac{1}{2} \int_P d^3 x \left[\frac{\left| (\vec{\nabla} \times (\vec{\xi} \times \vec{B}))_\perp \right|^2}{\mu_0} + \frac{B^2}{\mu_0} \left| \vec{\nabla} \cdot \vec{\xi}_\perp + 2\vec{\xi}_\perp \cdot \vec{\kappa} \right|^2 + \gamma p \left| \vec{\nabla} \cdot \vec{\xi} \right|^2 \right.$$
$$\left. - 2(\vec{\xi}_\perp \cdot \vec{\nabla} p)(\vec{\kappa} \cdot \vec{\xi}_\perp^*) - j_\parallel (\vec{\xi}_\perp^* \times \vec{b}) \cdot (\vec{\nabla} \times (\vec{\xi} \times \vec{B}))_\perp \right] \quad (2.18)$$

Here, $\vec{b}$ is the unit vector along $\vec{B}$ (or $\vec{B} = B\vec{b}$), $\vec{\kappa} = \vec{b} \cdot \vec{\nabla}\vec{b}$ is the curvature of $\vec{B}$, and * denotes complex conjugation.

Equation 2.18 is particularly useful because each of its terms has a physical interpretation which illuminates the physics behind many possible MHD modes. The first term represents the energy required to bend magnetic field lines, and is the dominant source of potential energy for the shear Alfvén wave. The second term represents magnetic field compression, and is the source for the compressional Alfvén wave. The third term represents the energy of plasma compression, and is the source of energy for sound waves. All three of these terms are non-negative, meaning that they are always stabilizing effects. However, the last two terms can be positive or negative, so that they may have stabilizing or destabilizing effects. The $\vec{\nabla} p$ term represents a pressure-drive for instabilities, while the $j_\parallel$ term represents a current based instability drive.

The MHD modes studied in this thesis are current-driven external kink modes, where the dominant drive for the instability comes from the $j_\parallel$ term in Equation 2.18. This requires

a large plasma current to enhance this term. The external kink resonates with a rational surface near the edge of the plasma, so the instability drive is increased when there are large currents and gradients at the edge. Such a broad current profile can be achieved by a rapid plasma breakdown which accumulates current in the edge regions. Due to the resonance between the kink and the rational surface near the edge, the dominant structure of the kink will be a resonant helical perturbation with poloidal and toroidal mode numbers $m/n = q_* \equiv \dfrac{aB_0}{R_0 B_p}$. The stabilizing nature of the field line bending term means that the long wavelength modes, which minimize the field line bending, should be the most unstable ones. While shorter wavelength (higher wavenumber) modes which are resonant may still exist, they are expected to be more stable due to the higher energy required for the increased bending of the field lines. Finally, because of the external nature of these modes, there will be significant magnetic interaction with the nearby conducting wall, and the mode should grow on the L/R magnetic diffusion time of the wall.

2.3 Fitzpatrick-Aydemir Model

While many of the properties of the external kink mode can be captured by ideal MHD, a more realistic simulation of the dynamics of the kink mode requires a more complete model. Effects such as plasma rotation [4], kinetic effects [32], or energy dissipation through coupling to other MHD waves [33] can affect the stability and evolution of the external kink. Fitzpatrick and Aydemir have developed a model of external kink dynamics including the effects of plasma rotation and dissipation, the presence of wall eddy currents, and external coils [34, 35]. In this formulation, the dynamics of the mode are described by the perturbed poloidal flux outside of the plasma, $\Psi(r, \theta, \phi, t)$. The magnetic field is related to this flux by

$$\vec{b} = \vec{\nabla}\Psi \times \hat{\phi}/R \tag{2.19}$$

In the high aspect-ratio limit, a cylindrical approximation can be used by substituting $\phi \rightarrow z/R$. If we then restrict ourselves to a single-helicity model, we have

$$\Psi(r, \theta, z, t) = Re \left[\psi(r, t) e^{i(m\theta + nz/R)} \right] \tag{2.20}$$

In the vacuum region where $\vec{j} = 0$, Ampere's law takes the form of Laplace's equation, $\nabla^2 \psi = 0$, which has solutions

$$\psi(r, t) \propto f(t) r^{\pm m} \tag{2.21}$$

Let the plasma edge be located at $r = a$ and the wall at $r = b$. Since we have the boundary condition $\psi(\infty) = 0$, we have only the decaying solution r^{-m} for $r > b$, but both solutions exist in the region $a < r < b$. If we define $\psi_a(t) = \psi(r = a, t)$ and $\psi_w(t) = \psi(r = b, t)$, then the solution to Laplace's equation can be written as:

$$\psi(r, t) = \begin{cases} \psi_a(t) \dfrac{(r/b)^m - (r/b)^{-m}}{(a/b)^m - (a/b)^{-m}} + \psi_w(t) \dfrac{(r/a)^m - (r/a)^{-m}}{(b/a)^m - (b/a)^{-m}}, & \text{for } a < r < b \\ \psi_w(t) \left(\dfrac{r}{b}\right)^{-m}, & \text{for } b < r \end{cases} \tag{2.22}$$

Thus the state of the system is defined completely by the complex vector

$$\vec{y}(t) = \begin{pmatrix} \psi_a(t) \\ \psi_w(t) \end{pmatrix} \tag{2.23}$$

The Fitzpatrick-Aydemir model describes the evolution of this state vector $\vec{y}$ as a function of time.

The Fitzpatrick-Aydemir dynamical model has been combined [36, 37] with the Boozer formalism for feedback equations for the RWM [8, 38, 39, 40], and this model has been used to model previous HBT-EP results [41, 42, 43]. In this model, the evolution of the kink is described by:

$$\frac{d\vec{y}}{dt} = A \cdot \vec{y} + \vec{R}\psi_c \tag{2.24}$$

where

$$A = \begin{pmatrix} (1 - \bar{s} + i\bar{\alpha}) \left(\dfrac{\gamma_{MHD}^2}{\nu_d}\right) & -\dfrac{\gamma_{MHD}^2}{\nu_d \sqrt{c}} \\ \dfrac{\gamma_w \sqrt{c}}{1 - c} & -\dfrac{\gamma_w}{1 - c} \end{pmatrix} \tag{2.25}$$

and

$$\vec{R} = \begin{pmatrix} -c_f \gamma_{MHD}^2/\nu_d \\ \gamma_w[1 - cc_f/(1-c)] \end{pmatrix} \tag{2.26}$$

Here, $\bar{s}$ is the dimensionless Boozer stability parameter, normalized such that $\bar{s} = 0$ corresponds to the no-wall limit and $\bar{s} = 1$ corresponds the ideal wall limit [8]. $\bar{\alpha} = \dfrac{-\nu_d \Omega}{\gamma_{MHD}^2}$ is a dimensionless torque parameter introduced by Boozer [38], which is proportional to ν_d, the energy dissipation rate due to non-ideal effects. Several physical mechanisms for this dissipation in HBT-EP plasmas have been proposed, including charge exchange with cold neutrals and neoclassical flow damping [42]. γ_{MHD} is an ideal MHD growth rate, γ_w is the inverse wall time of the resonant field, and Ω is the plasma rotation. The plasma-wall coupling is given by the parameter c, and c_f is the coupling of external coils with the plasma, relative to the plasma-wall coupling. The effects of the external coils are described by $\psi_c(t)$, which is the flux due to the coils, calculated at the wall radius.

These various model parameters are estimated for HBT-EP plasmas from a combination of experiment and modeling. The finite-element electromagnetic code VALEN [44] is used to calculate the RWM dispersion relation, which is used to fit for the model parameters γ_w, c, and γ_{MHD}. The rotation Ω is determined from experimental measurements of mode rotations in HBT-EP plasmas. The dissipation parameter ν_d is estimated in HBT-EP plasmas from previous work which measured the resonant field amplification as a function of the stability parameter $\bar{s}$ [41]. This work showed that HBT-EP plasmas must be in the 'high-dissipation' regime, resulting in a large torque parameter $\bar{\alpha}$. These estimated values are summarized in Table 2.1.

With the values of the parameters listed in Table 2.1, the two eigenvectors of A are

$$\vec{y}_1 = \begin{pmatrix} 0.999 \\ 0.048e^{-1.49i} \end{pmatrix} \tag{2.27}$$

Parameter		Typical Values
Stability parameter	$\bar{s}$	0.97
Torque parameter	$\bar{\alpha}$	2.3
Dissipation parameter	ν_d	450 ms^{-1}
Ideal MHD growth rate	γ_{MHD}	100 ms^{-1}
Inverse wall time	γ_w	3.4 ms^{-1}
Rotation	Ω	8 kHz
Plasma-wall coupling	c	0.258
Plasma-coil coupling	c_f	0.8

Table 2.1: Estimated values of parameters in the Fitzpatrick-Aydemir model for HBT-EP plasmas.

$$\vec{y}_2 = \begin{pmatrix} 0.67e^{1.66i} \\ 0.74 \end{pmatrix} \tag{2.28}$$

with characteristic frequencies $\lambda_1 = (-0.49 + 2\pi 7.7i)$ ms^{-1}, and $\lambda_2 = (-4.8 + 2\pi 0.34i)$ ms^{-1}. The first eigenmode has almost no flux at the wall, and is slowly damped and rapidly rotating ($\tau \approx 2$ ms, $f \approx 7.7$ kHz). We refer to this eigenmode as the "plasma mode". The second eigenmode has comparable flux at both the plasma and the wall, and is strongly damped and slowly rotating ($\tau \approx 0.2$ ms, $f \approx 0.34$ kHz). We refer to this eigenmode as the "wall mode".

This eigenmode basis will be important for physical interpretation of the measured plasma response in Chapter 6, where this model of kink mode dynamics will be used to model the plasma response to applied external fields and its interaction with the kink mode.

Chapter 3

Upgrades to the HBT-EP Experiment

The HBT-EP experiment has been upgraded to study the effects of 3D magnetic fields on MHD stability and multimode instability control [45]. This includes a new conducting wall, three modular control coil arrays with increased coverage and power, as well as a new high-accuracy, high-resolution magnetic diagnostic set. The design, construction, installation, and calibration of these various systems are described. The result of the upgrade is a system with the ability for high-speed, high-accuracy application and measurement of 3D magnetic structures with unprecedented detail in a tokamak device.

3.1   Conducting Wall

The new HBT-EP conducting wall is the third generation stabilizing wall installed on the device. The first generation wall consisted of 20 identical 1 cm thick aluminum shells for the demonstration of passive kink stabilization [46], and the second generation wall replaced every other toroidal section with 0.2 cm thick stainless steel shells for the implementation of smart-shell [9] and mode-control [47, 48] RWM feedback techniques. The newest wall is designed for the study of the physics and control of multimode MHD phenomena.

Like the two previous generations, the new HBT-EP wall consists of 20 independent

shell segments, shown schematically in Figure 3.1. Construction of the wall began with
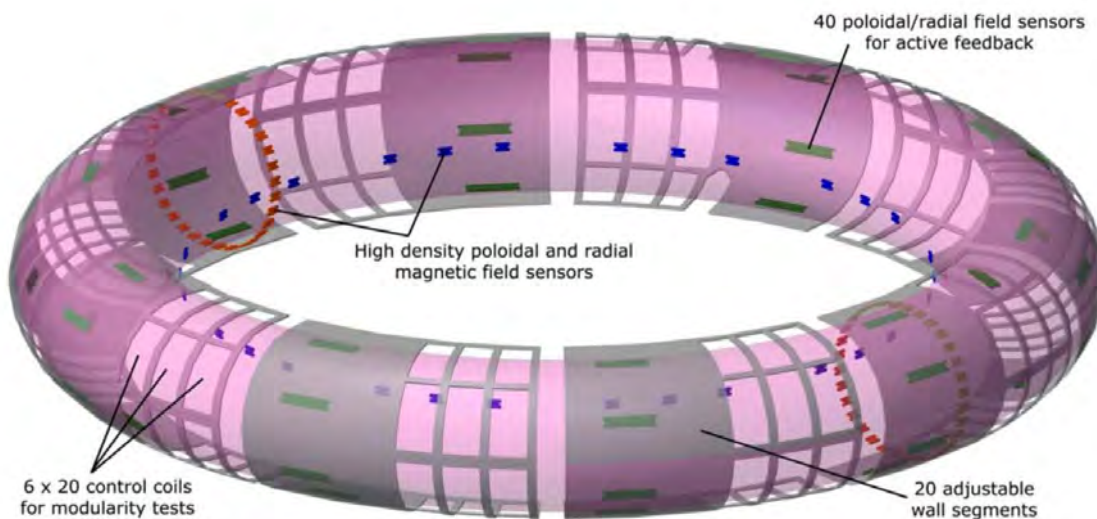
Figure 3.1: Schematic of the new conducting wall and magnetic diagnostic system in the upgraded HBT-EP system.

the spinning of three 3/16 inch thick 316 stainless steel sheets into continuous toroidally symmetric rings. These rings were annealed at 1850 °F to relieve the residual stresses from the spinning process, in order to minimize the mechanical deformation which would occur during later machining. Each of the rings were then laser-cut into ten 33° toroidal segments, with window-pane cutouts for the mounting of control coils, as shown in Figure 3.2. There are two rows of three control coil cutouts spaced 5° apart toroidally, leaving a 18° continuous segment. Most of the shells are of this standard design with only the control coil cutouts, but several shells were custom designed with minor modifications for diagnostic access. After machining, the individual shells were electropolished to reduce outgassing after installation in the vacuum chamber. Then, the continuous portion of each shell was electroplated with copper (as can be seen in Figure 3.2) to adjust the L/R diffusive wall time, which sets the RWM growth rate. The nominal copper thickness was chosen to be a uniform 5 mil layer
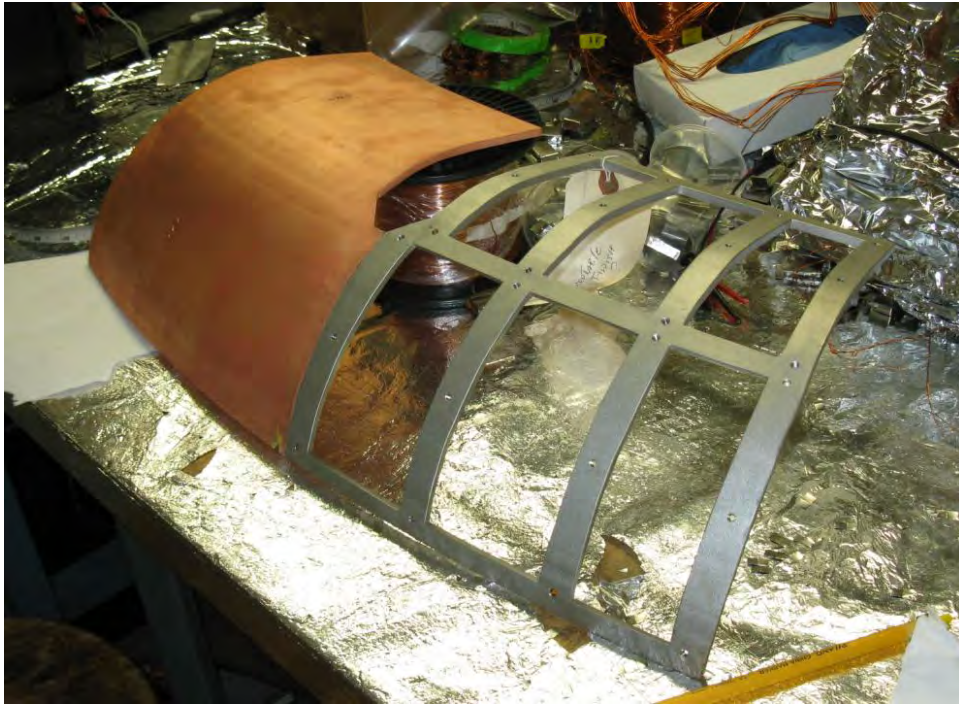
Figure 3.2: An individual machined wall segment with electroplated copper. The window-pane cutouts on the right side of the shell are for the control coil windings. This particular shell contains a custom cutout for an optical sightline in the middle of the shell.

(2.5 mil on each side of the shell) based on VALEN modeling, to set the walltime for the $n = 1$ RWM to be $\sim 400 \, \mu$s. Finally, the entire shell was electroplated with a 0.3 mil coating of chrome to reduce copper sputtering from interactions with any scrape-off layer plasma. In total, 26 shell segments were manufactured from the three toroidal rings, including spare pieces.

Although the design value of the copper plating was a uniform thickness of 5 mils, it is known from bench electromagnetic as well as optical microscope measurements that there is significant variation in the thickness of the copper plating from shell to shell, with the general trend being that there is excess copper on most shells. The relative thicknesses of the copper between shells were inferred by measuring the inductance of a small coil placed on various points along the surface of the shell, where the effective inductance of the coil is reduced

based on the conductivity of the nearby shell. Absolute measurements of the copper thickness were taken for a few shells by optical microscope measurements of destructive samples cut out of the shells. In addition, micrometer and microscope measurements indicate that there is more copper near the edge of each shell, giving a "hollow" profile to the copper thickness, rather than the uniform thickness as designed. Final selection of the 20 installed shells from the 26 constructed shells was made based on a combination of the measured electromagnetic properties, and dimensional consistency as determined by bench measurements, as well as by installation in a spare vacuum chamber segment.

Finally, a significant metrology effort was undertaken to ensure accurate alignment and installation of the shells in the tokamak. Due to both the annealing process during the construction as well as the careful metrology and installation, the alignment of the new wall is significantly improved over the previous generation wall and is comparable to the accuracy of the first generation thick aluminum wall. Metrology indicates that maximum radial deviations on most shells are under 5 mm, or 3% of the nominal wall radius [49]. Shells with larger deviations were positioned so as to ensure there was no interference with the last closed flux surface of the plasma. A combination of ROMER coordinate-measuring machine, laser scanning, and custom metrology equipment were used for this process. With the final installation geometry of the new wall, all shell segments can be moved outward by up to 4 cm in the minor radius direction, which varies the normalized wall radius from 1.07 to 1.33 to change the plasma-wall coupling.

3.2 Control Coils and Power Supplies

The new shells are instrumented with three sets of 40 independently powered control coils of varying toroidal extent, with any one of the three sets being energized at one time. Each of the three sets are distributed in a 4×10 array, allowing the application of a variety of 3D fields. The coils of each array cover either one, two, or three of the 5° wide control coil

cutouts, resulting in coils of 5° , 10° , or 15° toroidal extent. These angular widths of the coils were chosen to span the 10° port plug size of the ITER experiment. The differing toroidal extents of the three control coil sets allows a systematic study of the effect of sideband harmonics and their interaction with other stable or unstable MHD modes during $n = 1$ feedback and other experiments [50].

The winding configuration of each coil set is shown in Figure 3.3, where the overlapping red, blue, and green coils are the small, medium, and large coils respectively. The large and
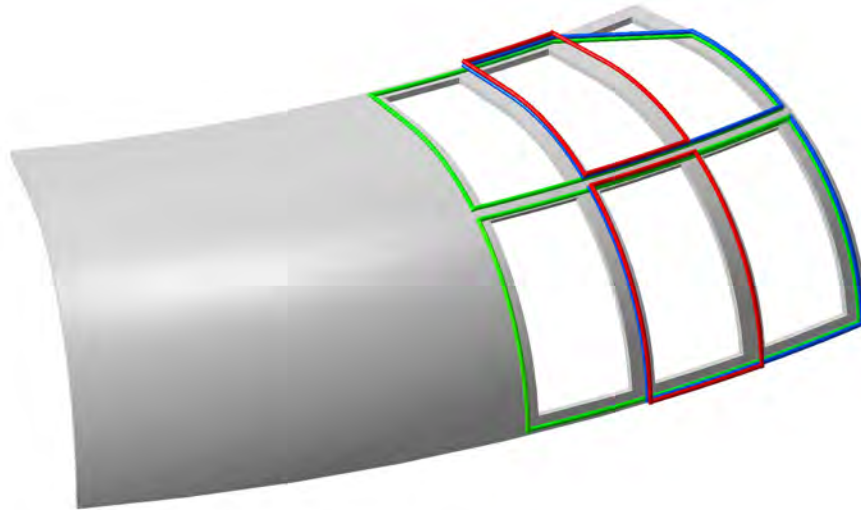
Figure 3.3: Winding pattern of the small (red), medium (blue), and large (green) control coil arrays.

medium coils at the top of the shell skip a corner (as shown) to avoid hitting the vacuum chamber when the shells are withdrawn. For the work in this thesis, only the large 15° coils are used. This largest of the three control coil arrays covers 25% of the plasma surface. The coils in this large coil set each have 12 turns of 24 AWG Kapton wire, resulting in a L/R time of $\approx 110\ \mu$s.

Five high-speed (1 MS/s update rate) FPGA-based controllers, each with eight independent 16-bit analog outputs (40 total outputs), are used to drive the control coils. The

FPGA control signals are amplified by a set of 20 dual-channel 2.5 kW audio amplifiers. The maximum deliverable control coil current in this system is ~ 45 A, as set by a circuit protection fuse. Each of the 40 coil currents are monitored with a 0.1 Ω shunt resistor.

3.3   Magnetic Diagnostics

The magnetic diagnostic system of HBT-EP was completely rebuilt, with the construction and installation of 216 new sensors. The sensors are Mirnov coils [51] oriented to measure the poloidal and radial components of the equilibrium and fluctuating magnetic fields. Construction of the sensors consists of 10-20 turns of 30 AWG Kapton wire around a machined Teflon form. The Teflon forms are of two types, with large (106 mm $\times$ 20 mm) "feedback" sensors and small (26 mm $\times$ 15 mm) "high-density" sensors. It is easy to show from Faraday's law that the signal in a Mirnov coil is:

$$V(t) = -NA\frac{\partial B(t)}{\partial t} \tag{3.1}$$

where N is the number of turns and A is the cross-sectional area of the probe, provided that the probe size is much smaller than the typical length scales of the magnetic field being measured. Since we are studying long wavelength MHD phenomena, this assumption is valid. Thus the sensitivity of each sensor is determined by its NA value.

These sensors are mounted on the conducting shells as well as on other internal structures built specifically for the magnetics. The distribution of these sensors within the machine is shown in Figure 3.1, along with the relative positions of the control coils and conducting wall. The Mirnov coils are arranged in three main diagnostic sets. The first is the set of large feedback sensors, which are mounted on the shells and arranged in a 4×10 array like the control coils. The poloidal placement of these sensors is the same as the centers of the control coils, while their toroidal placement is halfway between the control coils on either side, to minimize direct coupling. Each of these feedback sensors measure both the radial and

poloidal field, and are shown in green in Figure 3.1. The high-density sensors are divided into a toroidal array and a pair of poloidal arrays. The toroidal array is located slightly below the midplane on the high-field side of the machine, with 30 spatial points. These toroidal array sensors are not spaced evenly in toroidal angle because they are mounted on custom mounting brackets. All 30 probes measure the poloidal field, but only 10 of them measure the radial field as well. The toroidal array is shown in blue in Figure 3.1. The two poloidal arrays are located 180° apart toroidally, and are shown in orange in Figure 3.1. The two poloidal arrays are identical and have 32 probes each, with every probe measuring the poloidal field and with every other probe measuring the radial field. The outboard portion of each poloidal array is mounted directly on the conducting shells, while the remaining sensors on the inboard side are mounted on a custom support constructed of 1/16 inch thick stainless steel. Figures 3.4 and 3.5 show the installed poloidal and toroidal arrays in the HBT-EP device. Several of the feedback sensors are also visible in both photographs. All sensors are covered by a 2.5 mil thick stainless steel shield to protect them from any scrape-off layer plasma.

The output voltage of each Mirnov coil (Equation 3.1), which is proportional to the time-derivative of the magnetic field, is pre-amplified with an analog RC filter. The feedback sensor amplifiers have a gain of 10, while the high-density sensor amplifiers have a gain of 100 due to their small NA values leading to low signal levels. All amplifiers have a time constant of $RC = 200$ μs, which is comparable to the timescale of our signals, so that the signals are only partially integrated. However, this manages to lower all signal levels to within the ± 10 V input range of the digitizers. The partial integration of the analog circuit is completed numerically to correct for the transfer function of the amplifiers and convert all signals to equal the magnetic field itself [52].

Finally, in order to store the vast amount of data collected by this large new diagnostic set, the data-acquisition system has also been upgraded with 288 new differential digitizer
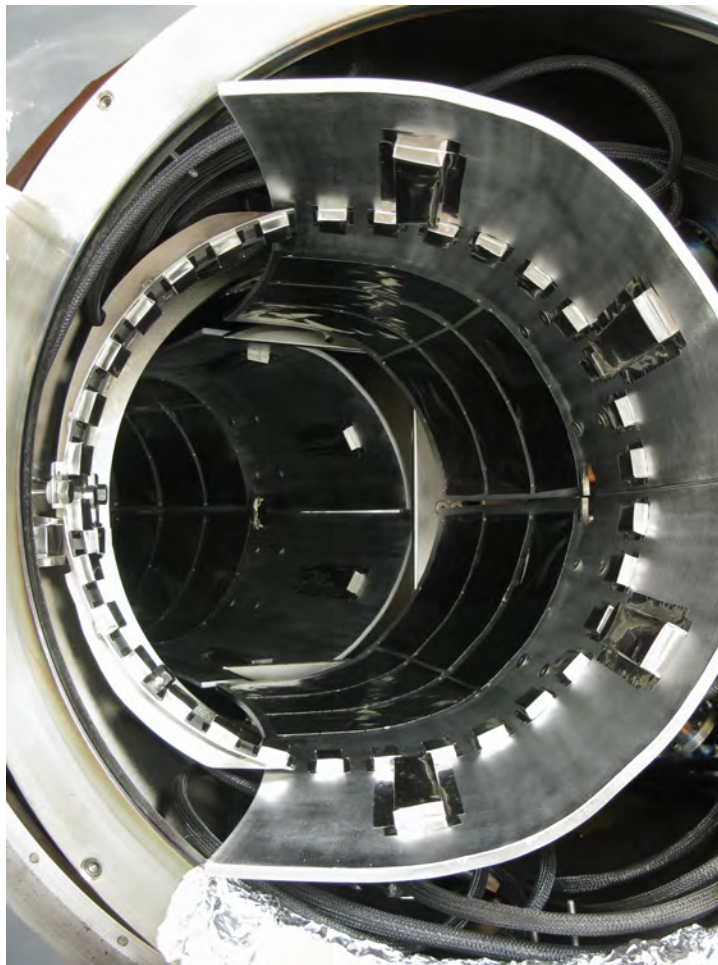
Figure 3.4: High-density poloidal array after installation.

channels with ± 10 V, 16-bit input and 500 kHz sampling.

3.4   Bench Calibrations

The NA value of each sensor was bench calibrated using a large Helmholtz coil. The coil radius was 22.5 cm, resulting in less than 0.5% spatial variation of the magnetic field over the sensor volume. The 4 kHz Helmholtz coil current was measured with a commercial $+1/-0$% accuracy Rogowski coil, and low signal levels were compensated for by averaging over many hundreds of periods. Thus it turns out that the ultimate limit on the precision of

Figure 3.5: One section of the high-density toroidal array (upper left) after installation.

the calibration is set not by our ability to measure the NA, but by actual changes in the NA value itself. This could be caused, for example, by looseness of the wires in the sensor, or deformation of the Teflon form of the sensor itself. Several modifications were made to the sensor design to minimize this problem, however it still presents the largest uncertainty in the calibration. This results in a different measured NA each time the sensor is handled and placed in the Helmholtz coil, and would also result in a different value upon final installation in the machine. To quantify this uncertainty, each sensor was calibrated three or more times, to give a range of measured NA values.

Figure 3.6 shows the results of this calibration for the poloidal field feedback sensors. The measured NA from each iteration of the calibration is plotted for each sensor. The solid line is the mean NA from all iterations of all sensors. The horizontal dotted lines are separated by $1/20^{\text{th}}$ of this mean value, where 20 is the nominal number of turns for this sensor type.
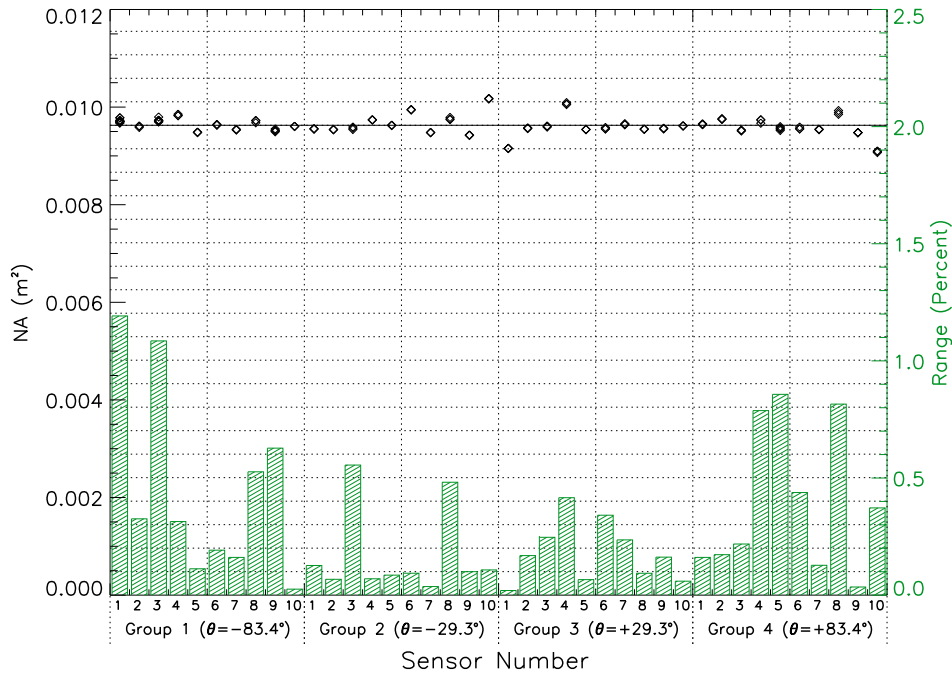
Figure 3.6: Bench calibration results for the set of poloidal field feedback sensors.

Thus it can be seen that some sensors, such as sensor 10 from Group 2, have an extra turn of wire. The green bars indicate the range, in percentages, of the measured NA over the three (or more) iterations. Thus most of the poloidal field feedback sensors have less than 0.5% variation in measured NA, with the highest value being 1.2%. The median and maximum values of these NA ranges are listed in Table 3.1, along with those for all other sensor types.

Sensor Type	Median Range (%)	Max Range (%)
Feedback Poloidal	0.17	1.1
Feedback Radial	0.14	0.7
High-density Poloidal	0.46	1.9
High-density Radial	0.18	0.6

Table 3.1: Summary of bench NA calibration results.

Chapter 4

In-Situ Magnetics Calibration

Accurate measurements of the 3D spatial structure of the magnetic field requires the physical locations of each sensor to be precisely known. In addition, since the magnetic diagnostics measure the component of the magnetic field in a certain direction, the orientation of these probes is also important. A unique in-situ magnetic diagnostic calibration technique was implemented on HBT-EP during an up-to-air period. Based on the measured coupling between a sensor and several calibration coils, the position of that sensor can be deduced. Since the calibration coils are built near the nominal location of the plasma current centroid, the technique is referred to as a "copper plasma".

4.1   Copper Plasma Construction

The HBT-EP copper plasma consists of four single-turn rings of 1/4 inch copper rod. Three of the rings are at the machine midplane. One of these has a major radius of 92 cm to match the nominal plasma radius, with the other rings at plus or minus one inch. The fourth ring also has 92 cm major radius and is located 0.75 inch below the midplane. This configuration as installed is shown in Figure 4.1. The rings are mounted in a G10 structure which is supported off of the close-fitting conducting wall of HBT-EP. The copper plasma assembly

is built in eight toroidal segments to allow installation through the vacuum chamber ports.
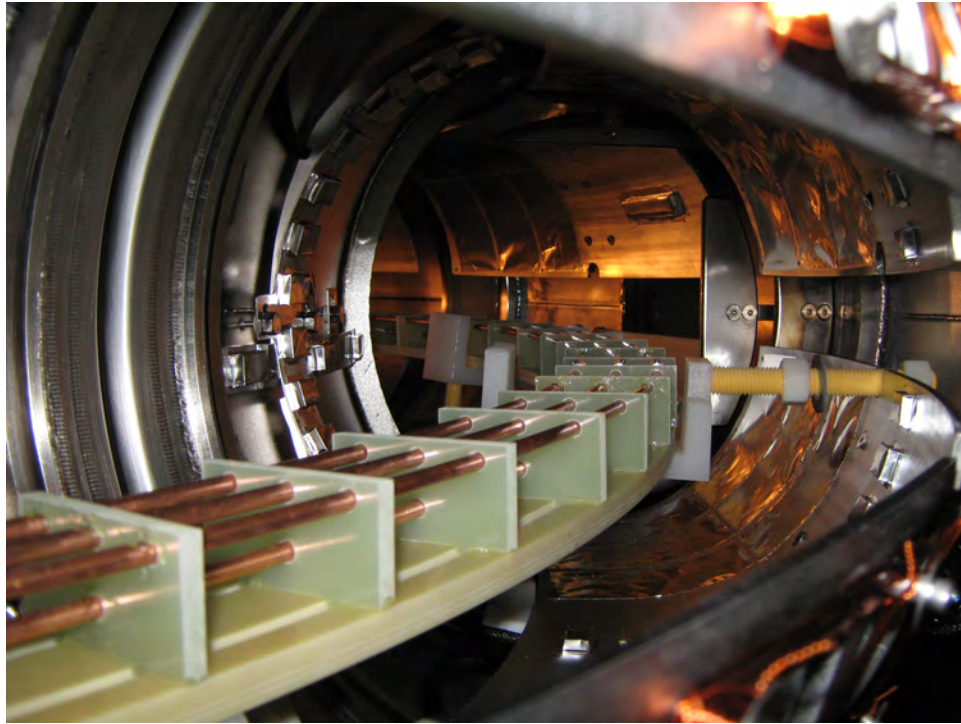
Figure 4.1: Copper plasma in the HBT-EP vacuum chamber.

The rings are energized individually with HBT-EP's vertical field (VF) capacitor bank consisting of a 15 kV, 60 μF start bank and a 450 V, 0.22 F power-crowbar bank to produce a step-like waveform. Currents up to 5 kA were driven in the copper plasma. In comparison, the plasma current of HBT-EP plasmas are of order 15 kA.

The radial and vertical alignment of the copper plasma was measured to be within 3 mm of the design, which is less than the minor radius of the copper conductor. The dominant alignment errors are $n = 1$, as shown in Figure 4.2, corresponding to a shift and a tilt of the assembled copper plasma.
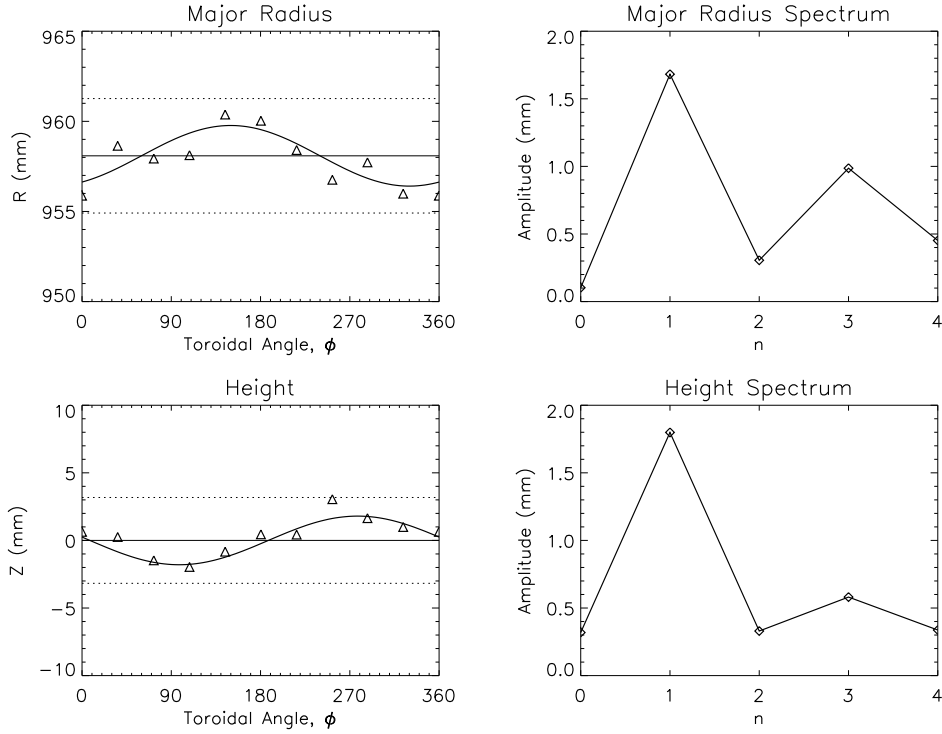
Figure 4.2: Measured alignment of installed copper plasma assembly, overplotted with the best-fit $n = 1$ component. The dashed lines in the left plots represent the physical extent of the conductor itself. Fourier decomposition shows that the major deviations are $n = 1$, corresponding to a shift and a tilt.

4.2 Response Function Technique

Accurate measurement of the sensor-coil couplings require careful consideration of eddy current effects. This is done as follows. The signal s in a given magnetic sensor can be related to the current I in a copper plasma of major radius R_i by a response function [53]:

$$s(t, R_i) = \int_0^t \frac{dI}{d\tau} \cdot r(t - \tau; R_i) d\tau \tag{4.1}$$

The response function r can be found by deconvolution. It represents the sensor response to an ideal step-function applied to the coil. Several examples of measured response functions on HBT-EP are shown in Figure 4.3. In the absence of eddy currents in nearby conducting structures, the response function itself is a step-function with height equal to the time-

independent Green's function for the particular coil-sensor pair. If eddy currents are present, the response function will differ from this step-function due to the fields created by the eddy currents. As these eddy currents decay, the response function approaches the vacuum response, so that the asymptotic value equals the time-independent Green's function:

$$G_{meas}(R_i) = \lim_{t \to \infty} r(t; R_i) \tag{4.2}$$

Thus we are able to experimentally measure the vacuum coupling between each coil and sensor. We can also compute this value if we know the exact geometry of the sensor:

$$G(\rho, \theta; \xi_1, \xi_2, R_i) = \frac{\vec{B}(\rho, \theta; I, R_i) \cdot \hat{n}(\xi_1, \xi_2)}{I} \tag{4.3}$$

where the position of the sensor is described in toroidal coordinates (ρ, θ, ϕ), and the orientation of the sensor is parameterized by two Euler angles (ξ_1, ξ_2). The Green's function is independent of ϕ due to the axisymmetry of the system.

In addition, the difference between the response function and a step-function gives the eddy current contribution to the sensor signal. As the response function asymptotes, this difference goes to zero, representing the eddy current decay. We can fit one or several time-constants to this decay and therefore measure the eddy current decay time. With the copper plasma on HBT-EP, this decay is well-represented with a single-pole model, as shown in Figure 4.4.

In addition, once the response function is known for a coil/sensor pair, we can use the convolution in Equation 4.1 to predict the signal s for any $I(t)$, not just the one used to calculate the response function. This is demonstrated in Figure 4.5, where the previously calculated response function is used to predict the measured signal for a much more rapid ($\sim$ 5 kHz) oscillating copper plasma current created by ringing the VF start bank. The response function is seen to accurately predict the sensor signal.
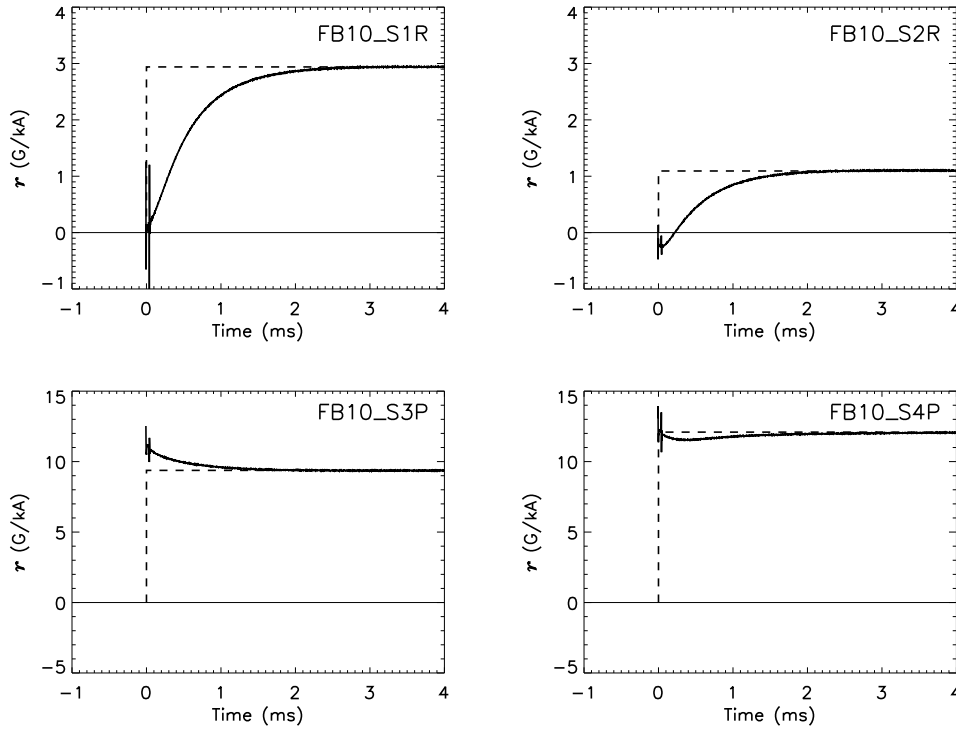
Figure 4.3: Examples of HBT-EP response functions with the copper plasma located at $R = 92$ cm and $z = 0$. The top two examples are radial sensors, and the bottom two are poloidal sensors. Also shown (dashed) are the ideal step responses which would be seen in the absence of eddy currents.

4.3   Comparison with Metrology

The new conducting wall and the magnetic diagnostic set were measured with a ROMER coordinate measuring machine. With the measured sensor and coil positions, as well as the known spatial structure of the dipole field created by the copper plasma, the expected Green's function for all sensor-coil pairs can be calculated (Eq. 4.3). This can be compared to the measured Green's function from the response function technique (Eq. 4.2), as shown in Figure 4.6. The larger discrepancy at $\phi = 230°$ is due to the error field from the leads to the copper plasma which were located at that toroidal section. For all other sensors, the agreement is excellent. In contrast, the nominal values would be constant across toroidal
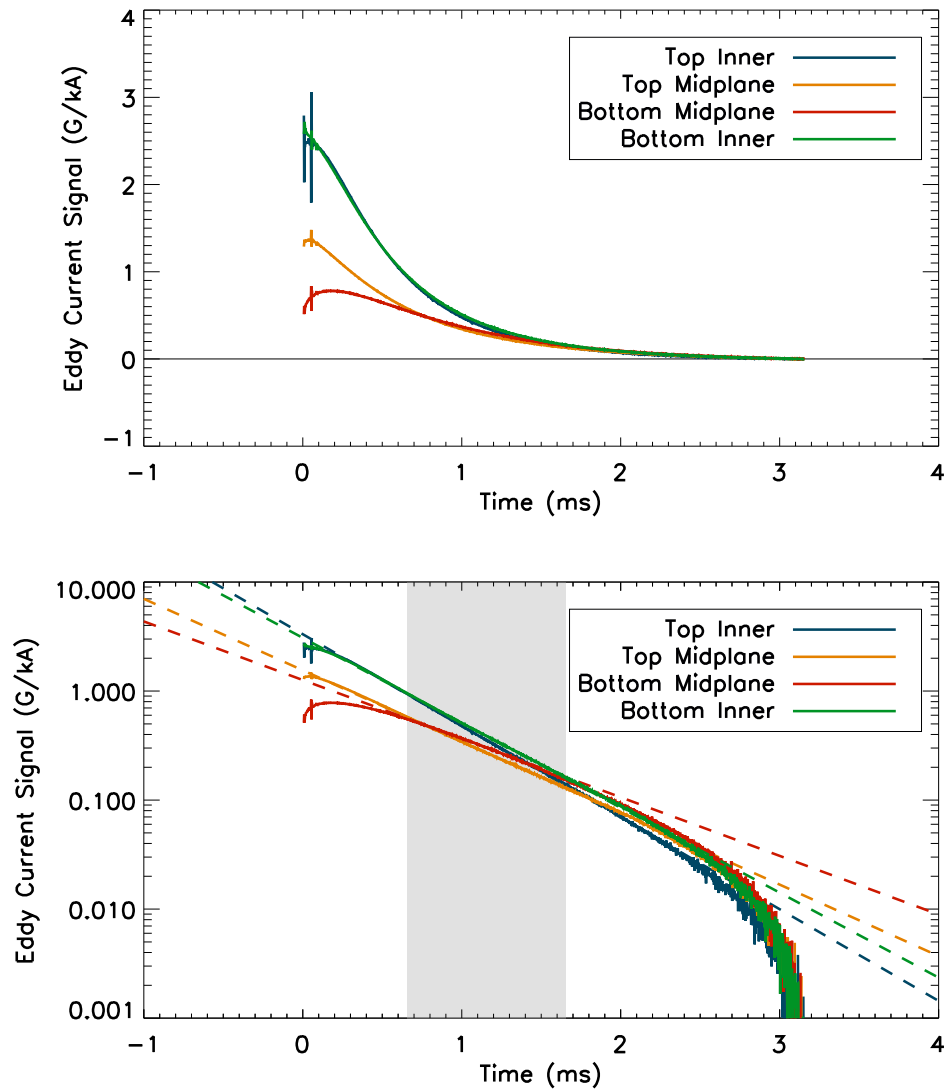
Figure 4.4: Eddy current contribution to the response function, for four radial feedback sensors. The single-pole fits are shown in the bottom plot (dahsed lines), where the decay time is fit over the highlighted period.

angle. This demomstrates that the spread in measured signal across sensors can be accounted for by displacements and misalignments of the sensors.
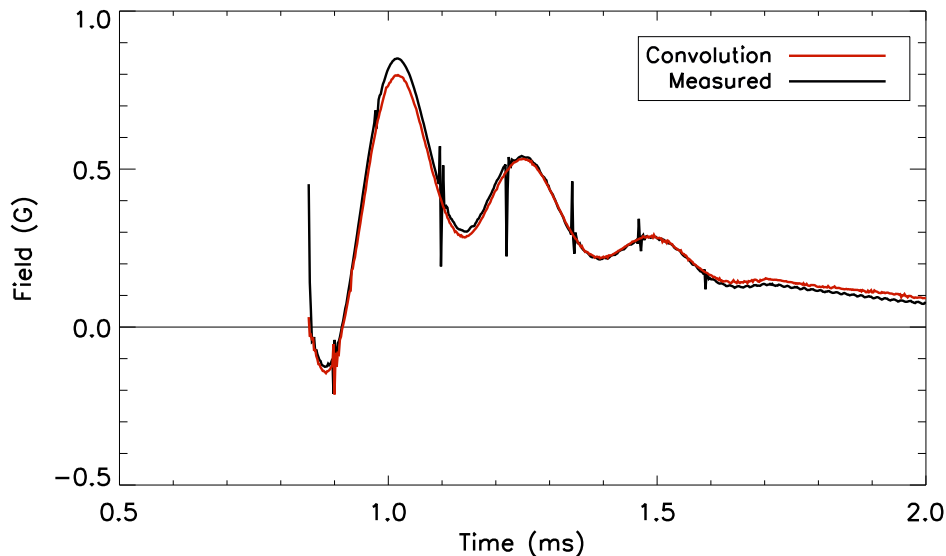
Figure 4.5: Convolution of the response function with the measured coil current accurately predicts the magnetic field seen by the sensor. Note that the timescale here is much shorter than that of the original response function (Figure 4.3).

4.4   Reconstructions

We can also use the measured coupling to multiple copper plasmas to reconstruct the position of each sensor. For this, we make several simplifying assumptions. If we assume that our calibration coils have been precisely aligned, then the Green's function is only a function of the sensor geometry. This can be parametrized by six variables: three spatial coordinates, two Euler angles, and a gain/sensitivity. The sensor gain (NA) can be eliminated as a variable if it is carefully calibrated on the bench (assuming it does not change during the installation process). Since the copper plasmas are toroidally symmetric, we are unable to resolve the ϕ coordinate from any measurements. Since we have four independent copper plasmas, it should be possible in principle to fit the remaining four unknowns. Unfortunately, due to electronics problems, data is available for only the three copper plasmas at the machine midplane. Thus here we take the ROMER-based Euler angles (ξ_1, ξ_2) to be correct, and only fit for the spatial coordinates (ρ, θ), leaving a two-parameter fit to the three measurements.
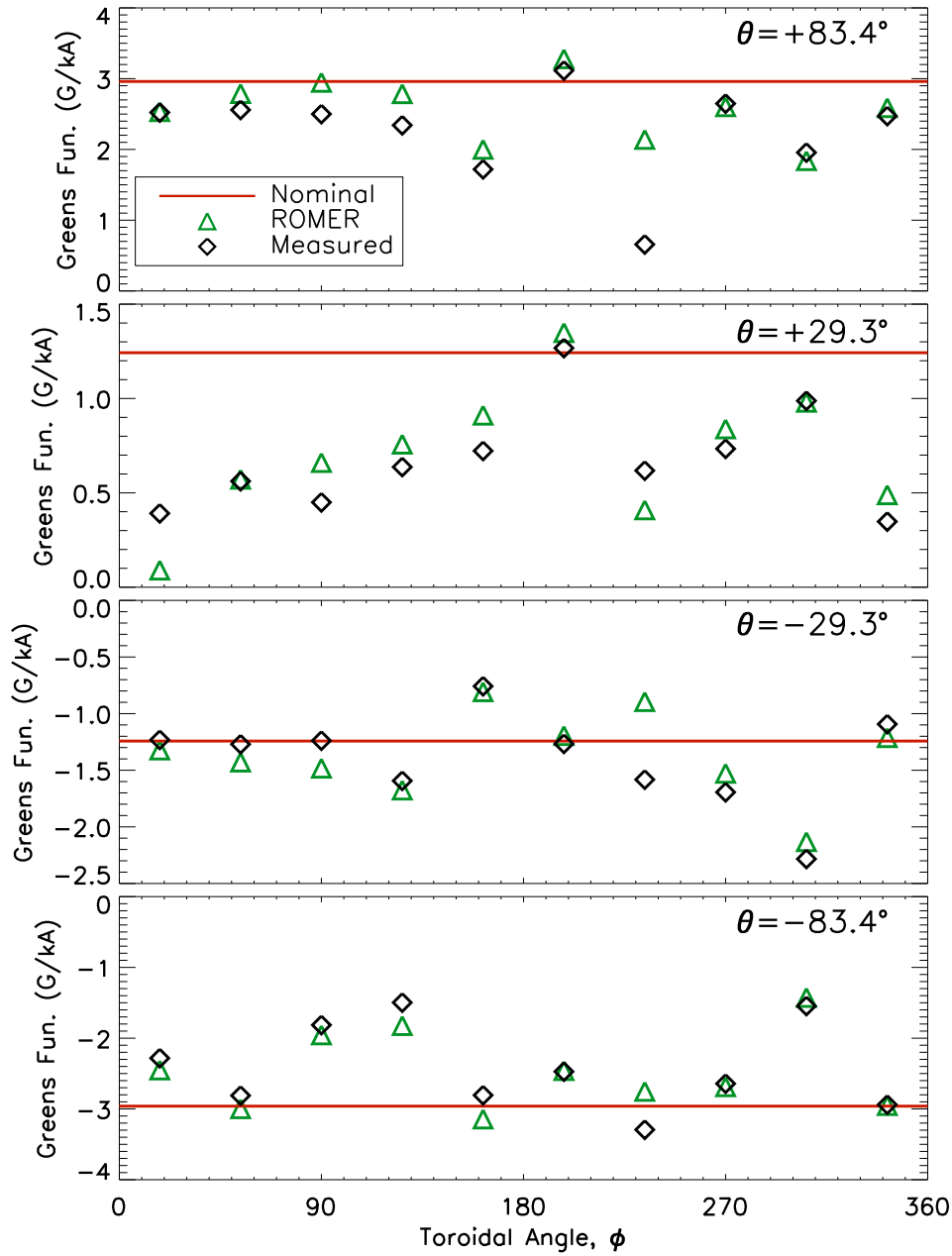
Figure 4.6: Comparison of experimentally measured Green's functions with values calculated using ROMER-measured sensor coordinates, for the $R = 92$ cm, $z = 0$ copper plasma. Error fields from the leads to the copper plasma cause the discrepancy at $\phi = 230°$.

Thus we minimize in a least-squares sense the residual between measured and computed Green's functions for the three copper plasmas:

$$E(\rho, \theta) = \left[\sum_i \left(G_{meas}(R_i) - G(\rho, \theta; \xi_1, \xi_2, R_i) \right)^2 \right]^{1/2} \tag{4.4}$$

The results of this minimization for four radial feedback sensors are shown in Figure 4.7. This fitting shows that small adjustments of the sensor position result in better overall agreement with the measurements from the various copper plasmas.
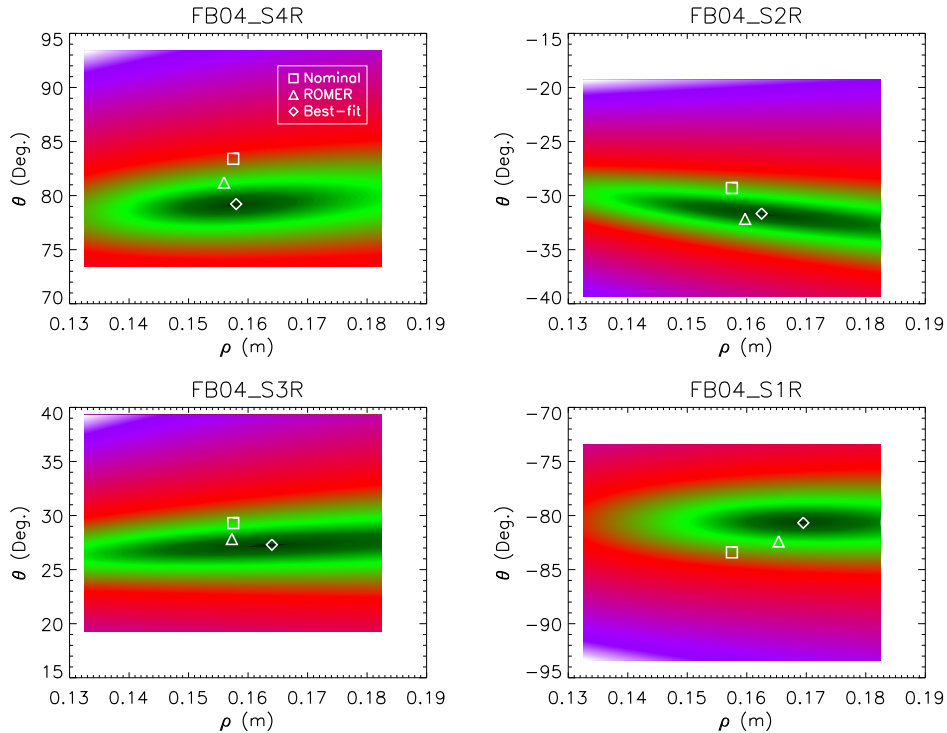
Figure 4.7: Contours of the residual (Eq. 4.4) in (ρ, θ) space, along with the nominal, ROMER, and best-fit sensor coordinates.

This can be seen again in Figure 4.8, where the expected Green's function is plotted as a function of copper plasma radius, using the nominal, ROMER, and best-fit sensor coordinates. This is overplotted with the measured Green's functions for the three copper plasmas.

This concept of determining the location of magnetic sensors by measuring the coupling to multiple coils has been previously implemented on the TCV tokamak, where the method
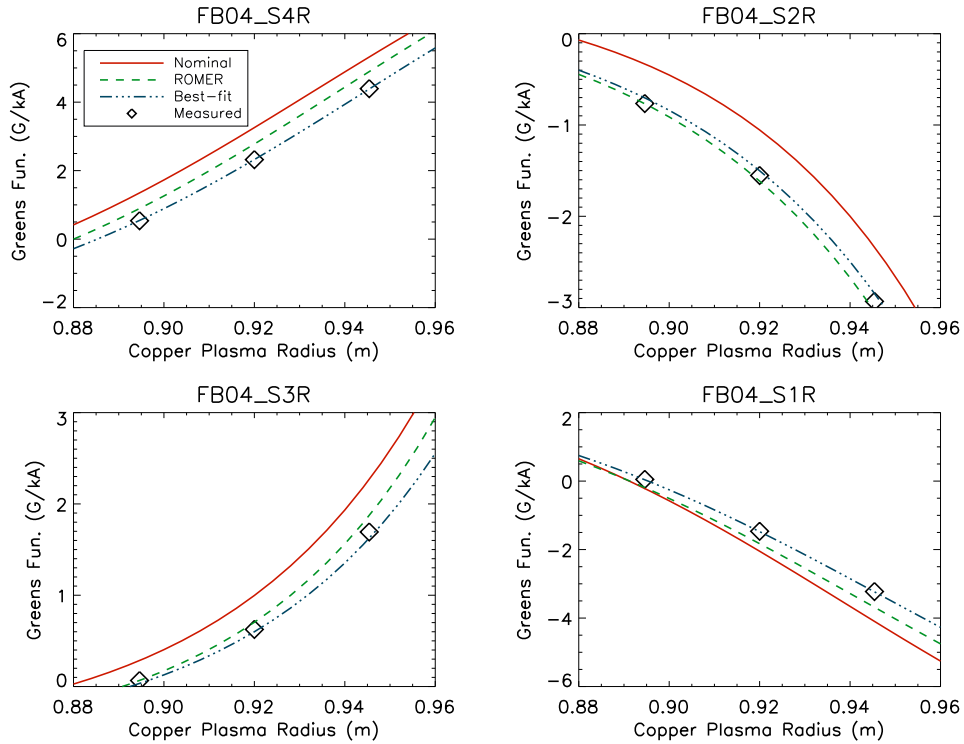
Figure 4.8: Comparison of measured Green's functions with calculated Green's functions using nominal, ROMER, and best-fit sensor coordinates, as a function of copper plasma radius.

was referred to as "magnetic triangulation" [54]. There, the coils used for this technique were the many poloidal field shaping coils of the device. The in-situ "copper plasma" coils are necessary for a device such as HBT-EP, which lacks numerous independently controlled equilibrium shaping coils. However, the "copper plasma" coils also have the advantage of having large coupling to almost all sensors by virtue of being installed at the location of the nominal plasma current centroid. In addition, devices with complicated coil geometries, such as stellarators, may also find this technique more practical.

4.5   Comparison with VALEN Modeling

The copper plasma experiment can be modeled with a time-domain VALEN simulation. Using the experimentally measured copper plasma current trace, we calculate the expected eddy currents in the surrounding conducting wall and the resulting magnetic field measured by all sensors. From this simulation, we can calculate the response function for each coil/sensor pair, and all resulting values such as the Green's function or eddy current decay time. For this simulation, we use the nominal locations and orientations of the sensors. We find that the measured decay times differ systematically from the nominal values, with most of the measured values tending to be higher. This is in agreement with the microscope measurements indicating excess copper over design values.

By varying the copper thickness profile in the VALEN model, we are able to more closely match the experimentally measured eddy current decay times. This is highlighted for a few sensors in Figure 4.9. In particular, the decay time in the poloidal sensors is predicted to be higher near the midplane ($\theta = 0$) with the nominal copper profile, whereas the experimental measurements are clearly lower there. This feature is only recreated when the modeled copper thickness profile is made hollow, with more copper at the edges. This too is consistent with microscope and bench micrometer measurements of the copper thickness. In addition, both the radial and poloidal decay times measured tend to be systematically higher or lower on different shells. This can be adjusted by changing the total amount of copper on each individual shell in the model. The adjustments made here are also consistent with the bench electromagnetic measurements of relative copper thicknesses between shells. The modifications made to the VALEN model of HBT-EP based on the copper plasma calibration have been incorporated into the latest computational model (shown in Figure 4.10) which has been used for all calculations and simulations of HBT-EP experiments.
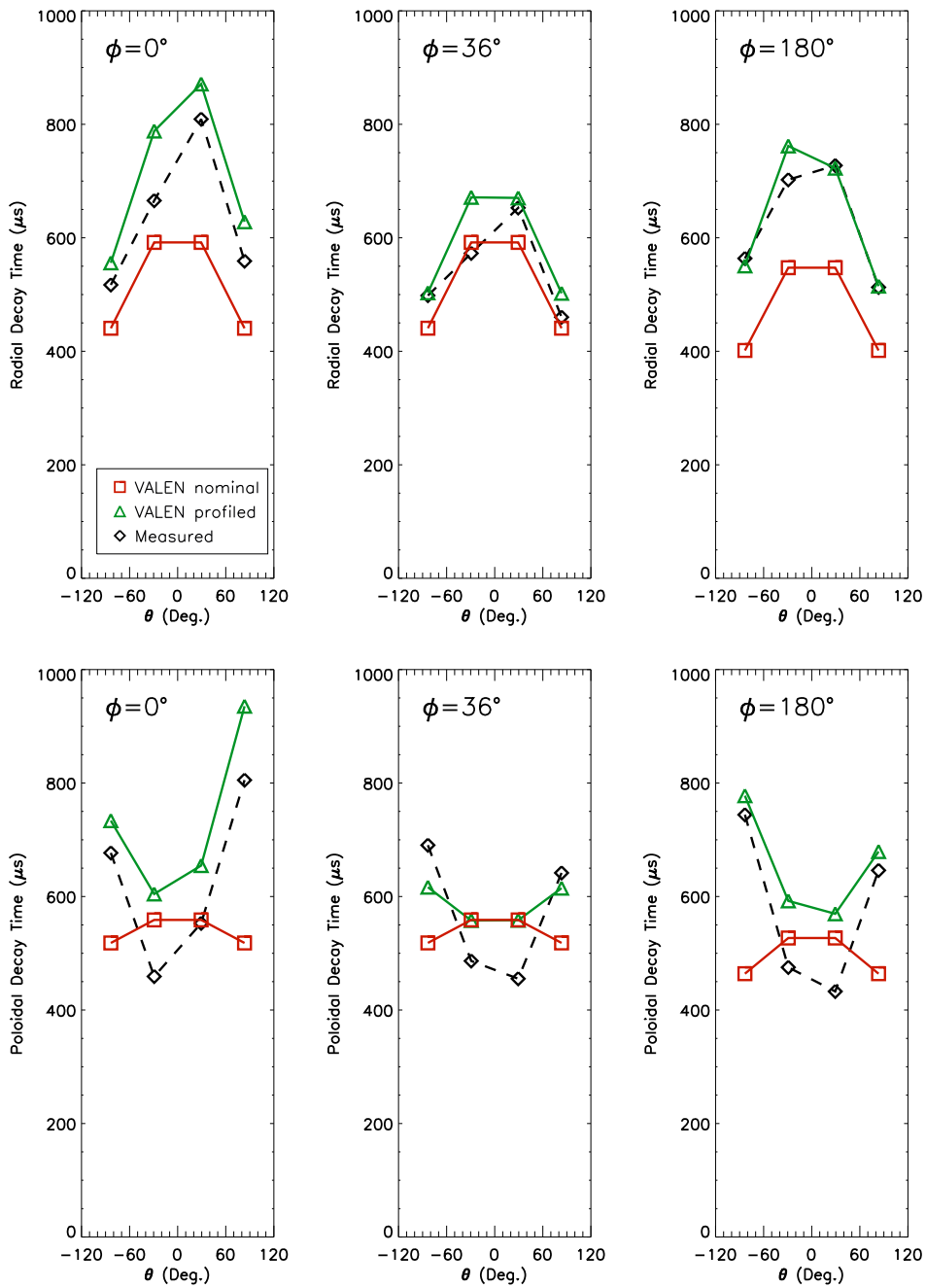
Figure 4.9: Comparison of measured and VALEN modeled single-pole eddy current decay times, for several feedback sensors. The top plots are for radial sensors and the bottom plots are for poloidal sensors. VALEN results are shown for two cases: with nominal uniform copper plating, and with adjusted copper profiles to better match the measured values.
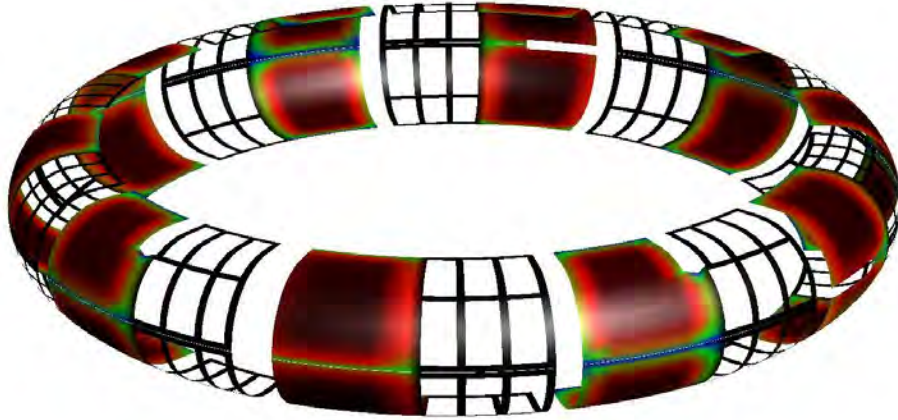
Figure 4.10: Contour plot of modeled copper thicknesses in the latest VALEN model of HBT-EP.

4.6 Major Radius Calibration

The copper plasmas of three different major radii also allows an in-situ calibration of the $cos(\theta)$ Rogowski coil, which is used to determine the major radius of the plasma. All experimental measurements of the plasma major radius, and hence edge q, are based on this calibration. The $cos(\theta)$ signal normalized to the total current is measured for the three copper plasmas of differing major radius, then interpolated with a first or second order polynomial to give the plasma major radius as a function of the $cos(\theta)$ Rogowski signal. This is in contrast to previous calibrations of the $cos(\theta)$ Rogowski coil based on detection of the poloidal field reversal using an internal magnetic probe over many plasma discharges [55].

In subsequent plasma discharges, the resulting edge q calculated from the measured major radius shows good correlation with the helicity and spatial structures of measured magnetic fluctuations. In addition, the location of the plasma edge can be directly measured by the presence of a Langmuir probe inside the plasma. In this case we use the unenergized bias probe, through which a large current is drawn when the probe is inside the plasma. This current goes to zero when the plasma moves past the probe, giving a direct measure of the

plasma edge at that one instant in time. This is compared to the location of the plasma edge as calculated from the major radius and known limiter positions, under the assumption of circular flux surfaces. This comparison is shown for several discharges in Figure 4.11, where the bias current measurements support the calculated values and hence the $cos(\theta)$ Rogowski calibration.
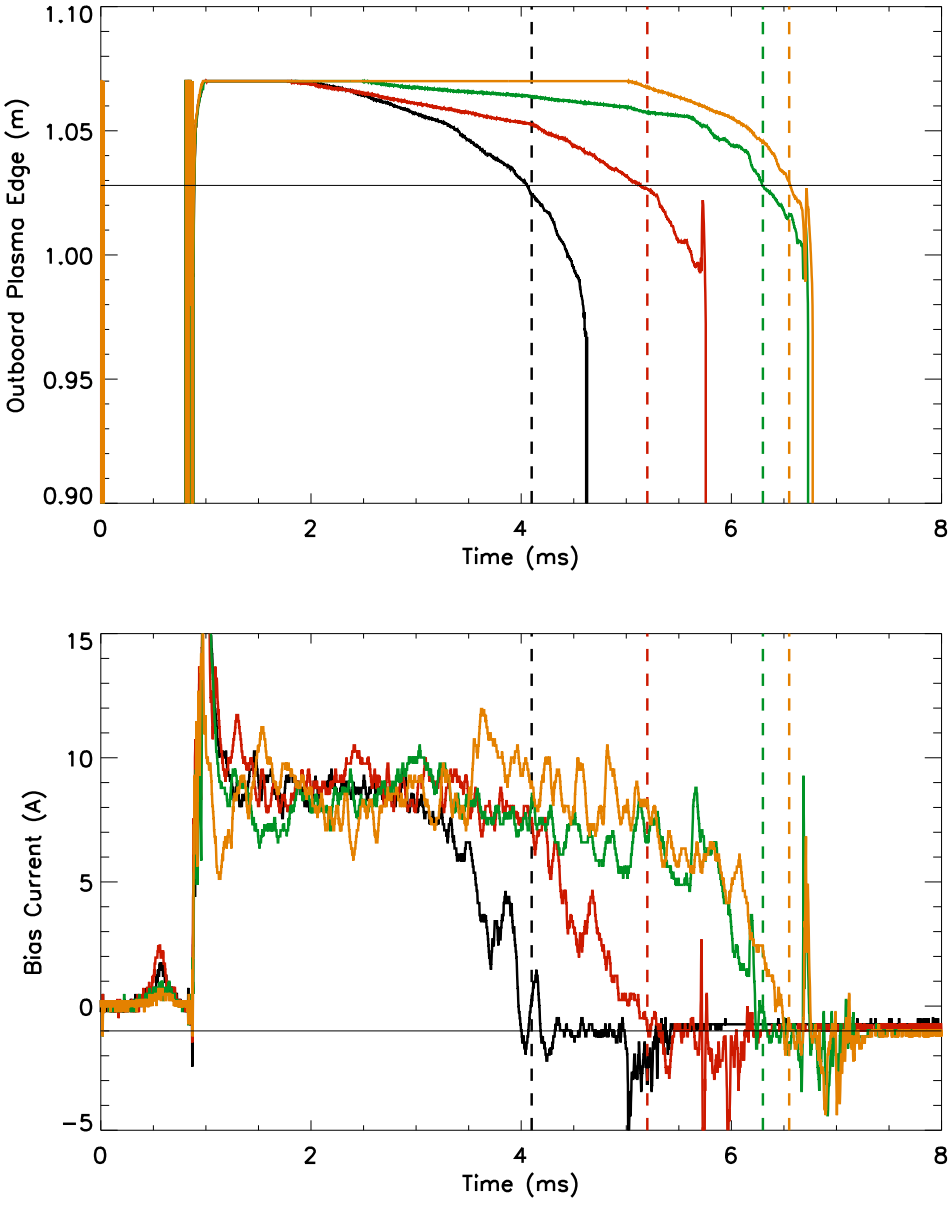
Figure 4.11: Calculated location of plasma edge, and bias probe current, as functions of time. The bias probe location is shown in the top plot as the solid line.

Chapter 5

Passive MHD Spectroscopy Measurements

The large number of new magnetic diagnostics on HBT-EP allows extremely detailed measurements of MHD phenomena. The resulting large spatio-temporal datasets routinely collected for every discharge are very well-suited for biorthogonal decomposition analysis, which decomposes the data into superpositions of independent orthogonal modes. Initial measurements with this diagnostic set clearly reveal the multimode nature of naturally occuring kink modes in HBT-EP plasmas. In addition, biorthogonal decomposition analysis of passive mode measurements provide an important basis for later work on active MHD spectroscopy experiments. These passive spectroscopy measurements and their analysis techniques are described, and worked out in detail for an example discharge.

5.1 Raw Data

A typical HBT-EP current ramp discharge is shown in Figure 5.1, which is designed to be unstable to current driven external kinks [48]. A rapid start-up initializes a high starting plasma current of 8-9 kA, in addition to generating a large current gradient near the plasma edge. This high edge current gradient leads to a large instability drive for the external kink.

The plasma current is then ramped at a rate of ~ 1 MA/s helping to maintain and sustain the broad current profile. During this current ramp, the plasma major radius slowly decreases, resulting in a q evolution that initializes at near 4, then crosses to below 3, bringing the $q = 3$ surface external to the plasma. The crossing of the $q = 3$ surface is accompanied by a large burst of magnetic fluctuations seen in the Fourier Rogowskis and Mirnov coils. These naturally occuring modes are studied here.
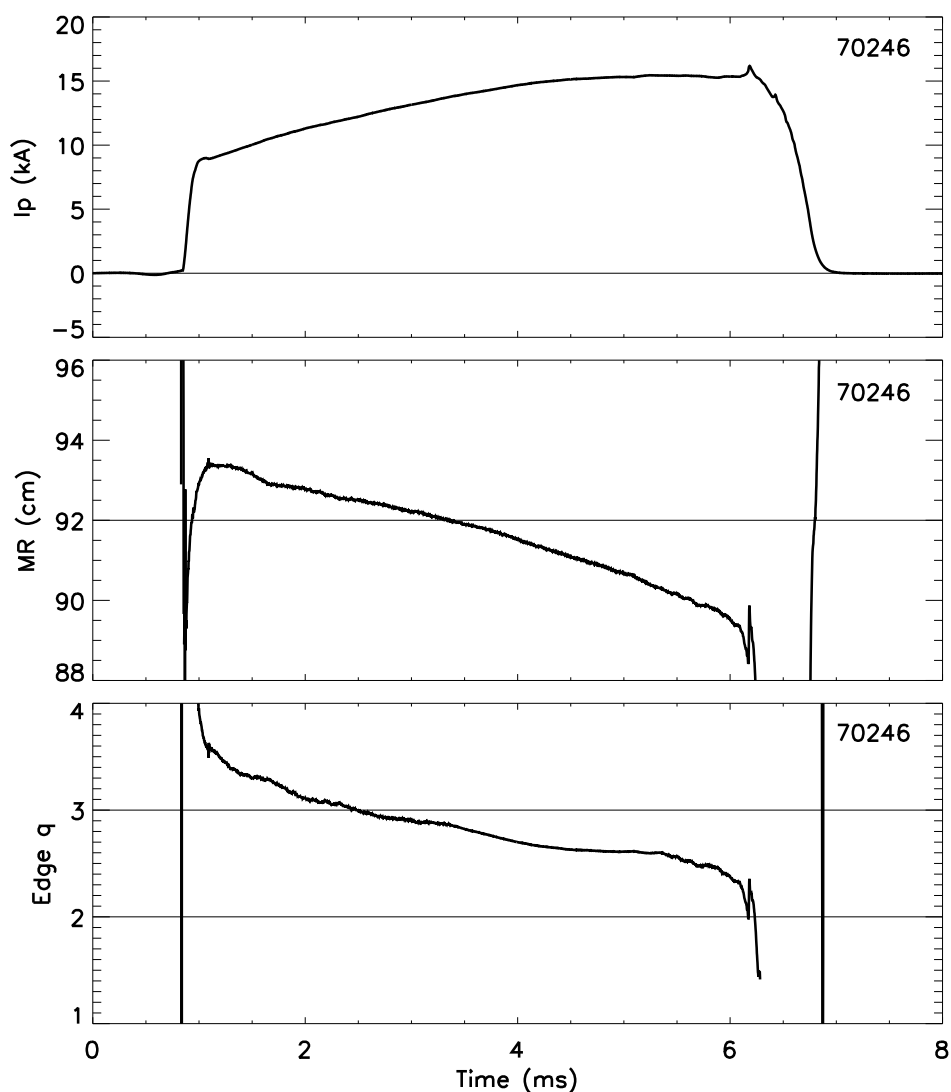
Figure 5.1: Plasma current, major radius, and edge q for a typical HBT-EP current ramp discharge (70246).

The total signal in a given magnetic sensor consists of both equilibrium and fluctuating fields. The equilibrium components are used for reconstructions of the plasma equilibrium [56], but the detection and study of MHD phenomena focuses on the fluctuating fields, which are perturbations from the equilibrium. The equilibrium fields are extracted from the total signal by temporal smoothing, since the equilibrium evolves over several milliseconds, while typical modes in HBT-EP plasmas rotate at 5-8 kHz. This separation of the equilibrium field by temporal smoothing is performed for each sensor individually, resulting in the full perturbed field dataset.

Figure 5.2 shows the fluctuating components of the high-density poloidal and toroidal array signals for discharge 70246 (Figure 5.1), during a half millisecond period shortly after the $q = 3$ surface goes external. The white diamonds on the left denote the location of each sen-
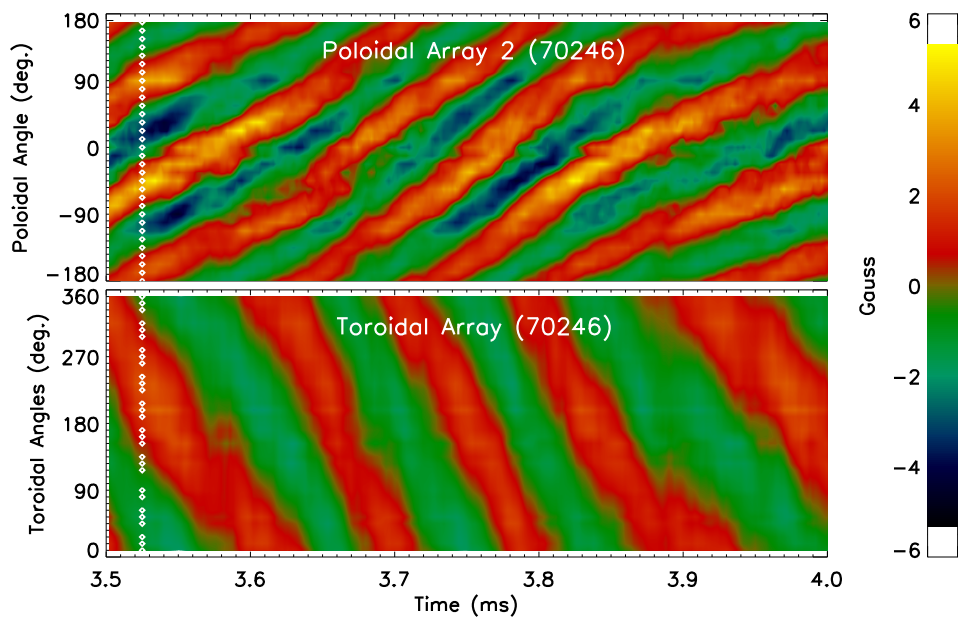
Figure 5.2: Perturbed poloidal field data from the high-density poloidal and toroidal arrays for shot 70246 (shown in Figure 5.1). The white diamonds on the left side of the plots show the locations of each individual sensor.

sor, while the temporal sampling is 500 kHz, resulting in an extremely rich spatio-temporal dataset collected for every HBT-EP discharge. It is clear from the high density array signals

that the dominant structure is a rotating $m/n = 3/1$ helical mode rotating in the negative ϕ direction, which is the direction of the electron fluid flow (counter I_p). The observation of magnetic fluctuations propagating in the electron fluid frame is seen in many experiments [31, 57]. As expected, this observed 3/1 structure is the longest wavelength structure that is resonant with the edge safety factor. However, full biorthogonal decomposition analysis reveals that, in fact, there is additional multimode structure to these modes.

5.2 Biorthogonal Decomposition

The high spatial and temporal resolution of the magnetics dataset lends itself very naturally to a biorthogonal decomposition (BD) analysis [58, 59], which decomposes a spatio-temporal data matrix into an ordered sum of products of spatial and temporal modes:

$$\delta B(x_i, t_j) = \sum_{k=1}^{n} \sigma_k u_k(t_j) v_k(x_i) \tag{5.1}$$

where the spatial and temporal modes are orthogonal: $u_k u^l = \delta_k{}^l$ and $v_k v^l = \delta_k{}^l$.

The biorthogonal decomposition is based on a Singular Value Decomposition (SVD) of the data matrix:

$$A = U\Sigma V^\dagger \tag{5.2}$$

where the columns of A are the time series from the various sensors. Because U and V are orthogonal matrices, the SVD of A is equivalent to the eigenvalue decomposition of the data covariance matrices (AA^T and $A^T A$). Thus the temporal modes $\{\vec{u}_k\}$ and spatial modes $\{\vec{v}_k\}$ (which are the columns of U and V) represent a list of the most coherent structures present in the dataset, and the corresponding singular values σ_k (which are the non-zero elements of the diagonal matrix Σ) tell the importance of each structure, with the power in the kth mode being proportioanl to σ_k^2. For a very coherent dataset, only a few singular values are of non-negligible value. Thus the singular value spectrum will reveal the number of physically meaningful coherent modes present in the data.

The decomposition in the form of Equation 5.1 is particularly useful when the data measures a traveling wave. This can be seen by the trigonometric identity

$$\cos(n\phi + \omega t) = \cos(n\phi)\cos(\omega t) - \sin(n\phi)\sin(\omega t) \tag{5.3}$$

which expresses a traveling wave as a sum of products of spatial and temporal functions. Note that in this case of a purely sinusoidal traveling wave, both terms in the sum are of equal weight, and that both the spatial and temporal modes are composed of quadrature pairs. This feature of degenerate quadrature pairs proves to be a characteristic signature of traveling waves in BD analysis. In such cases, the temporal modes can be thought of as time-dependent amplitudes of the quadrature spatial modes, so that there is a very natural interpretation of the amplitude and phase of the mode:

$$c_1(t)\cos(n\phi) + c_2(t)\sin(n\phi) = A(t)\cos(n\phi + \delta(t)) \tag{5.4}$$

where

$$A(t) = \sqrt{c_1^2(t) + c_2^2(t)} \tag{5.5}$$

$$\delta(t) = \arctan\left(\frac{c_2(t)}{c_1(t)}\right) \tag{5.6}$$

It follows from the properties of the SVD that the BD spatial and temporal modes form a complete and orthonormal set. Thus another interpretation of the biorthogonal decomposition is as an expansion of the data according to an orthonormal basis which itself is determined by the data. This is in contrast to an expansion using a pre-determined basis, such as a Fourier basis. Allowing the basis to be determined by the data itself has the advantage of being robust against some potential errors. For example, if there is a systematic or specific error associated with a subset of sensors, this error is accounted for by adjustment of the basis vectors themselves, rather than broadening of the the spectrum, as would occur for a fixed pre-determined basis. This, too, is easily understood in the example of a traveling

sinusoidal wave, where a weighting factor $f(\phi)$ in the sensors is absorbed into the spatial modes, which are simply modified from $cos(n\phi)$ to $f(\phi)cos(n\phi)$:

$$f(\phi)\cos(n\phi + \omega t) = f(\phi)\cos(n\phi) \cdot \cos(\omega t) - f(\phi)\sin(n\phi) \cdot \sin(\omega t) \tag{5.7}$$

This may happen, for instance, if the calibration of a specific sensor is inaccurate, or if the plasma is not centered within the poloidal array, enhancing the coupling to some sensors in the array and reducing the coupling to others.

5.3 Multimode RWM Behavior

Application of the biorthogonal decomposition technique to the RWM data shown in Figure 5.2 reveals the rich multimode nature of the mode. The singular value spectrum and the first six spatial modes are shown in Figure 5.3. The steep fall-off in singular values indicate a high amount of structure in the data, and the first six BD modes account for $\sum_{k=1}^{6} \sigma_k^2 / \sum_{k=1}^{n} \sigma_k^2 = 97\%$ of the fluctuation energy. Further, these six singular values are seen to occur in three (nearly) degenerate pairs, shown in orange, green, and red. The poloidal and toroidal structures of the corresponding spatial modes are shown on the right, and each of the (nearly) degenerate pairs is seen to be a quadrature pair of increasing wavenumber. The first and second pair are easily identified as $m/n = 3/1$ and $6/2$ respectively. The third pair is seen to be $n = 3$, although the poloidal structure is less clear. However, the clearest portion of the mode on the outboard portion (right side of the poloidal structure) is consistent with approximately $m = 9$. Thus both of the first two pairs, and possibly the third, are seen to be resonant with the equilibrium safety factor at the plasma edge. Of these three pairs, the fluctuation energy in each pair is 91, 4, and 2% of the total, showing strong ordering even within the physically meaningful modes. As expected, the power of these modes fall off with increasing modenumber, since the field line bending term in Equation 2.18 makes the longest wavelength MHD modes the most unstable.
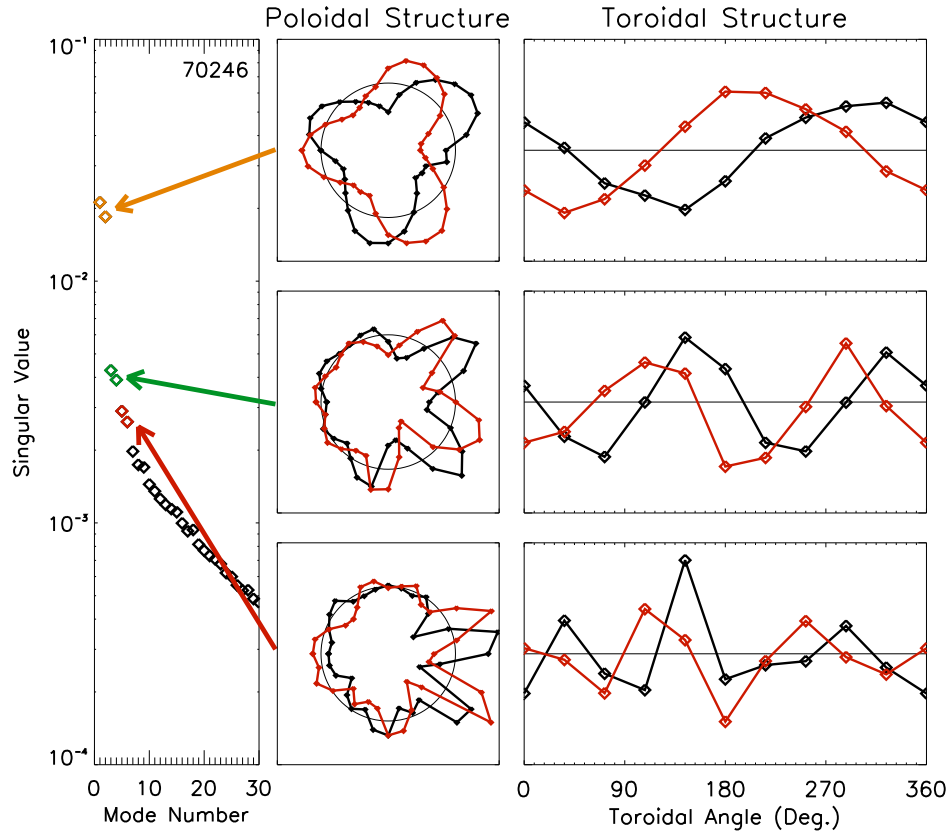
Figure 5.3: Singular value spectrum from Biorthogonal Decomposition of the data shown in Figure 5.2. Only the first 30 singular values are shown. The poloidal and toroidal structures of the first six spatial modes are also shown. For the poloidal structures, the machine center is to the left.

Due to the fixed sensor positions while the plasma position evolves, the plasma-sensor coupling is not constant. In particular, the two poloidal arrays are not always concentric with the flux surfaces of the plasma. Since many of the plasmas studied here are outboard limited, the coupling to the high-field side sensors can be small. This is precisely the situation described in Equation 5.7, and in fact, the spatial modes are seen to account for this in the poloidal structures shown in Figure 5.3. This effect is particularly large for high wavenumber modes, whose perturbed flux fall off as r^{-m} (Equation 2.21). This reduced coupling affects both the inboard portion of the poloidal array as well as the entire high-field side toroidal

array, often making the toroidal array data difficult to analyze. Similarly, the spatial mode is seen to be larger at the bottom of the poloidal array than at the top, indicating that the equilibrium plasma is centered below the machine midplane.

The first six temporal modes for this biorthogonal decomposition are shown in Figure 5.4, and these, too, are seen to be quadrature pairs. Thus our BD modes are made up of degen-
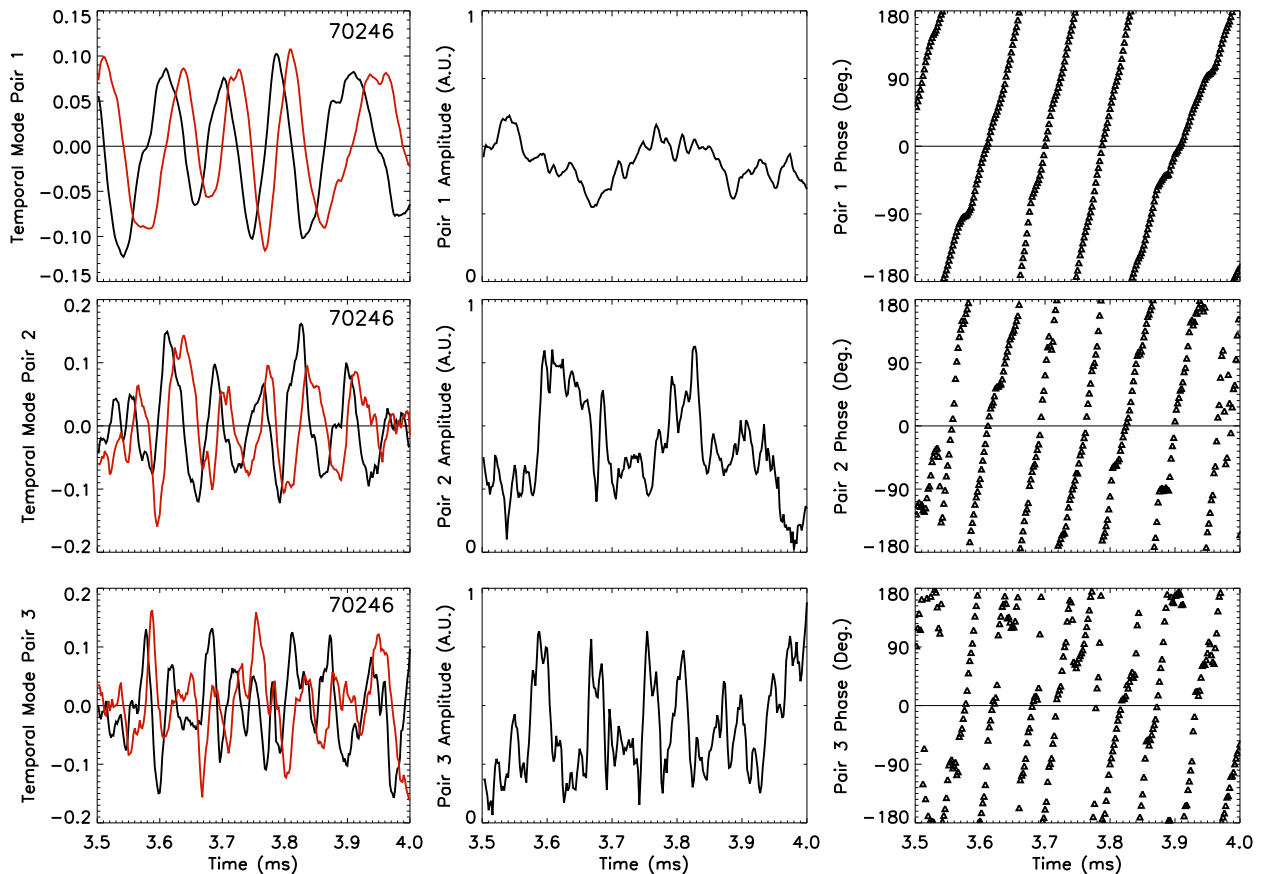
Figure 5.4: The first six temporal modes from biorthogonal decomposition analysis of shot 70246. These are interpreted as three quadrature pairs, with the resulting amplitudes and phases shown.

erate quadrature pairs of spatial and temporal modes, which, as discussed in Section 5.2, is the signature of traveling waves. Therefore we can interpret an amplitude and phase as defined in Equation 5.5-5.6, and these are also plotted in Figure 5.4. As expected, all of these

are seen to be traveling (rotating) structures. However, perhaps one of the most significant results of this BD analysis is the phase evolution of the 3/1 and 6/2 modes. The rotation of the two modes are observed to be different, with the 6/2 mode rotating slower than the 3/1. This is an unambiguous and direct observation that a naturally occurring RWM can evolve in a non-rigid multimode manner. And while the $n = 3$ phase is not as coherent, it appears to be rotating even more slowly than the $n = 2$ mode. The observed slowing of rotation with increasing mode numbers could be explained by the increased electromagnetic drag felt by each mode due to the wall. Therefore, it is conceivable that a similar dispersion of MHD modes could be caused by external coils, either intentionally in multimode MHD spectroscopy experiments, or unintentionally in control scenarios.

Using both the spatial and temporal modes, it is possible to reconstruct each pair of BD modes individually, which mathematically is just a truncation of the summation in Equation 5.1. These reconstructed modes for the poloidal field sensors of the poloidal array are shown in Figure 5.5. The coherence of these reconstructed structures indicate that they are physically relevant MHD modes; similar "reconstructions" using the lower power BD modes would appear as noise with no discernable structure. The dominance of the $m/n = 3/1$ mode is obvious by comparison with the original full dataset in Figure 5.2, which is expected since it accounts for 91% of the fluctuation energy. This last fact suggests one more advantage of the biorthogonal decomposition analysis, which is that it provides an empirically determined basis with which to fit modes in similar plasmas. This basis automatically takes into account such factors as differing coupling to various sensors, as shown already in Figure 5.3.

5.4 RWM Coupling to Control Coils

When the power amplifiers to the control coils are energized, but with no input signal, coupling from the rotating RWM is able to drive measurable currents in the control coil
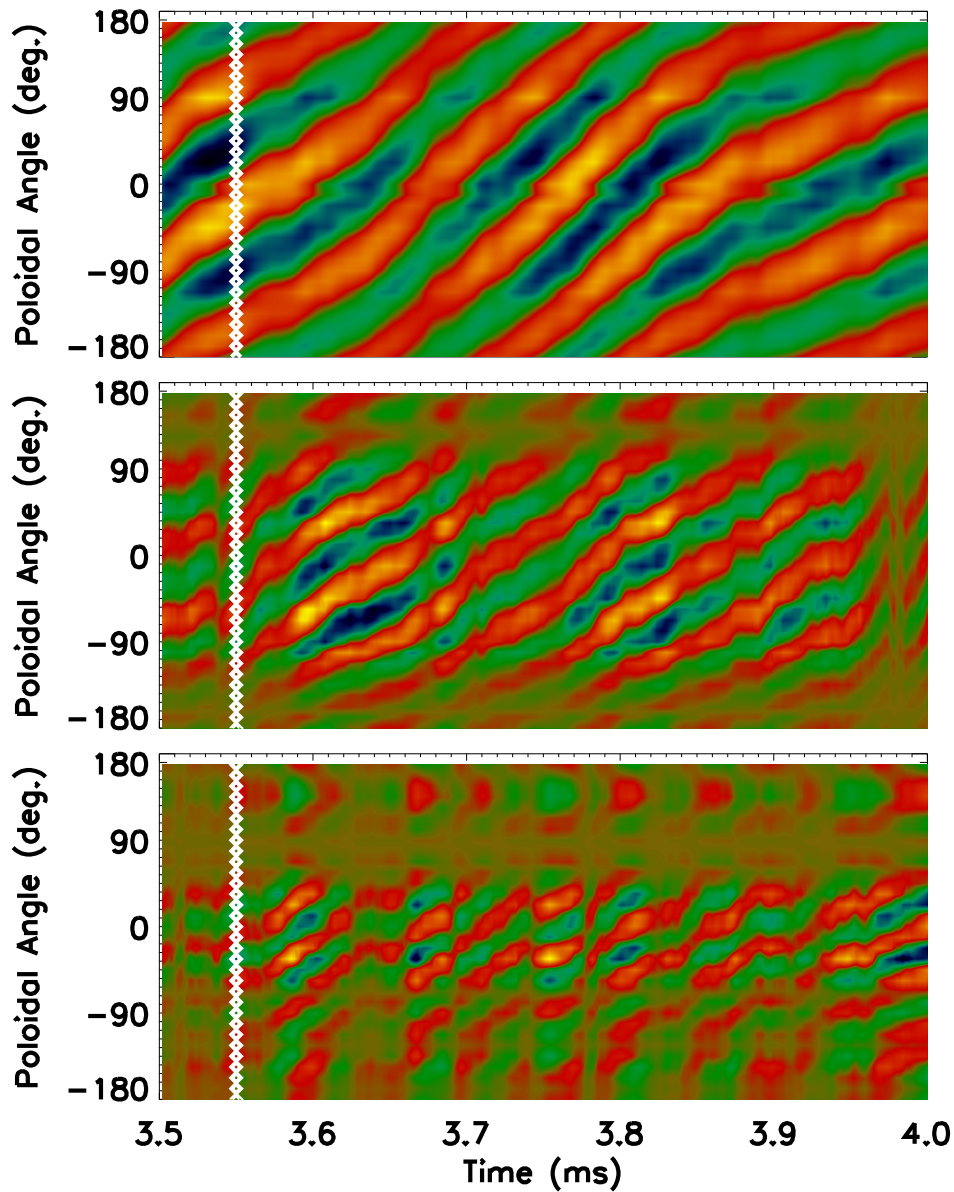
Figure 5.5: Reconstructed BD modes by quadrature pair, for the poloidal field sensors of the poloidal array.

circuit. Thus the control coils effectively act as radial saddle coils which detect the perturbed flux from the RWM. Since the control coils are spatially distributed over much of the plasma surface and are digitized individually, we can use this effect to passively measure the natural coupling between the coils and the plasma. As expected, biorthogonal decomposition of these

induced currents reveal a dominant $m/n = 3/1$ structure, with a degenerate quadrature pair due to the rotation of the mode. This pair of spatial modes, shown in Figure 5.6, is extremely useful, as it is an empirical measure of the coil current configuration which most optimally couples to the natural modes of the plasma. Linear combinations of these two quadrature modes allow arbitrary toroidal phasing to be chosen.
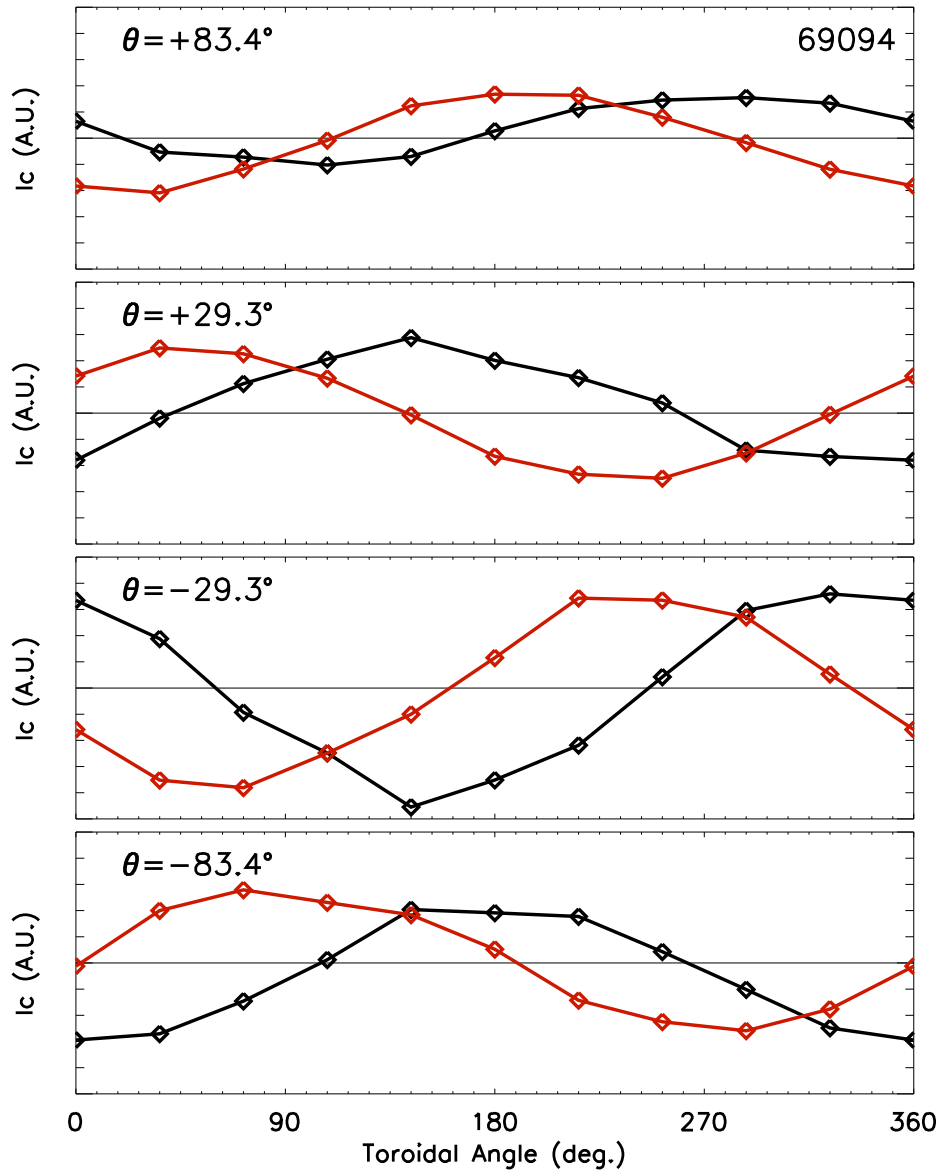
Figure 5.6: The two most dominant spatial modes from biorthogonal decomposition of the induced currents in the 40 control coils, from passive RWM measurements in shot 69094. This is an empirical measure of the configuration of coil currents which most optimally couples to the plasma.

Chapter 6

Excitation and Detection of Plasma Response

In addition to our passive measurements of natural modes, we are able to excite plasma response by applying an appropriate 3D external magnetic field. In this work, we use a "phase-flip" resonant magnetic perturbation (RMP) to excite a plasma response. The resonant nature of the field results in a large plasma response, and the phase-flip evolution of the RMP allows easy detection of this plasma response over a slowly evolving equilibrium. The resulting plasma response is observed to occur independent of the presence of a naturally rotating kink, consistent with the predictions of the Fitzpatrick-Aydemir model. Both the driven response and the rotating kink are observed to have identical spatial structure, with independent temporal evolution.

6.1 Phase-Flip RMPs

The "phase-flip" perturbation is a non-rotating external magnetic field which is applied for some period of time, then reversed in sign and held in the opposite polarity for an equal period of time, before being turned off [41]. This temporal evolution is shown in Figure 6.1. The roll-over in the current is due to a combination of the amplifier rise time and the control
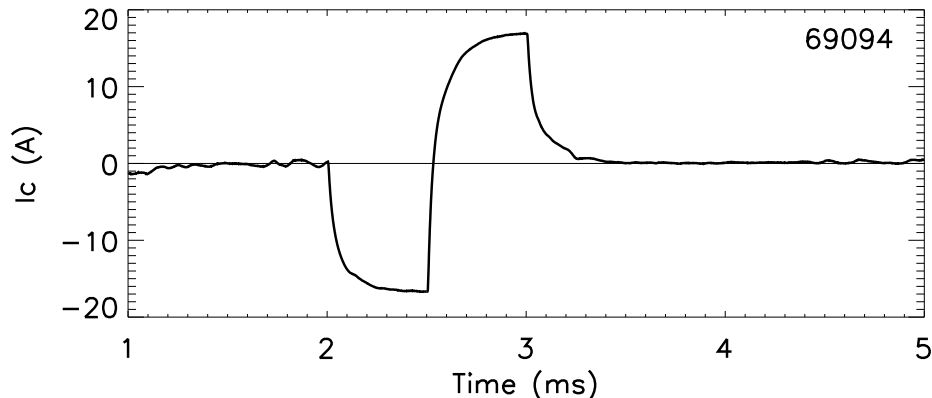
Figure 6.1: Temporal evolution of the applied field in a phase-flip perturbation.

coil inductance. The spatial distribution of the applied currents can vary, but is usually chosen to be a simple Fourier component, so that the current in a given control coil is given by:

$$I(\theta_i, \phi_j, t) = A(t)cos(m\theta_i + n\phi_j + \Delta\phi) \tag{6.1}$$

where $A(t)$ is the time evolution shown in Figure 6.1. In this work, we use only the large $15°$ control coils, which applies the most flux for a given amount of coil current, in addition to having the smallest sideband content. The resulting normal field at the plasma surface from a $m/n = 3/1$ configuration is shown in Figure 6.2.

Control coil currents of up to ~ 45 A can be driven through the 12 turns of the $15°$ coils for a maximum of 480 Ampere-turns. The applied resonant component for a $m/n = 3/1$ configuration is 0.33 G/A. Thus the maximum resonant RMP amplitude is ≈ 15 G, which represents a normalized perturbation amplitude of $B_r^{3/1}/B_\theta \sim 7 \times 10^{-2}$ or $B_r^{3/1}/B_T = 4.5 \times 10^{-3}$.

6.2 Detection of Plasma Response

When a resonant phase-flip is applied, the plasma response is clearly detected in the magnetic sensor signals. Figure 6.3 shows a typical discharge to which a phase-flip RMP is applied.
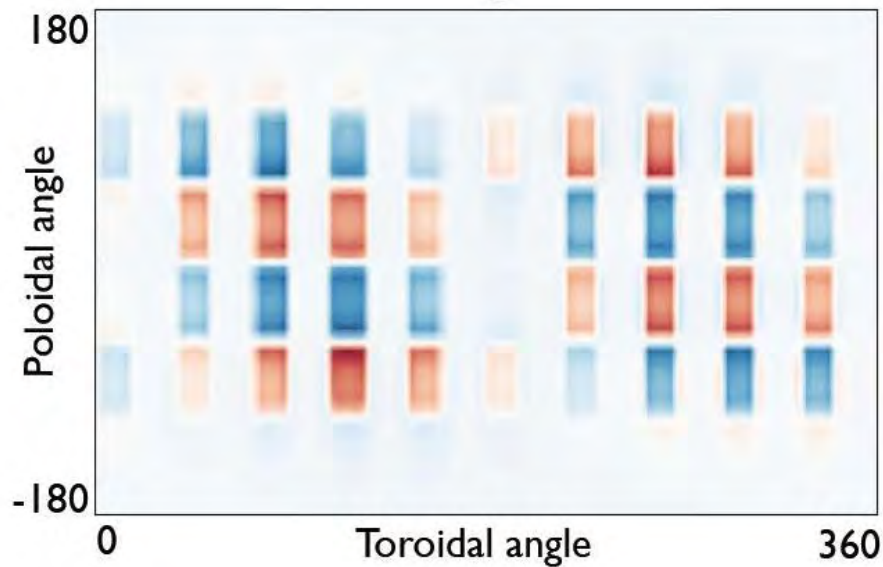
Figure 6.2: Calculated spatial structure of the applied radial field at the plasma surface for a $m/n = 3/1$ coil configuration.

At around 2 ms, the $q = 3$ surface becomes external, and a $m/n = 3/1$ phase-flip is applied at the time indicated by the vertical dashed lines. The bottom plot in Figure 6.3 shows the signals in a pair of poloidal field sensors separated toroidally by 180°, which shows a clear $n = 1$ "phase-flip like" response at the time that the phase-flip is applied. Note that even though the equilibrium poloidal field is evolving slowly relative to the RMP, the plasma response is still clearly observed.

Compared to the faster (6-8 kHz) RWMs analyzed in the previous chapter, the phase-flip RMP is relatively slow (~ 1 kHz), so that a simple smoothing algorithm for extracting the equilibrium field proves to be more difficult. We instead develop a new method using the following assumptions: that the plasma returns to the unperturbed state after the RMP is turned off, and that the equilibrium evolution is slower than the phase-flip evolution. This allows us to approximate the equilibrium signal using a low-order polynomial which fits the measured signal for a period of time before and after the phase-flip. An example of these
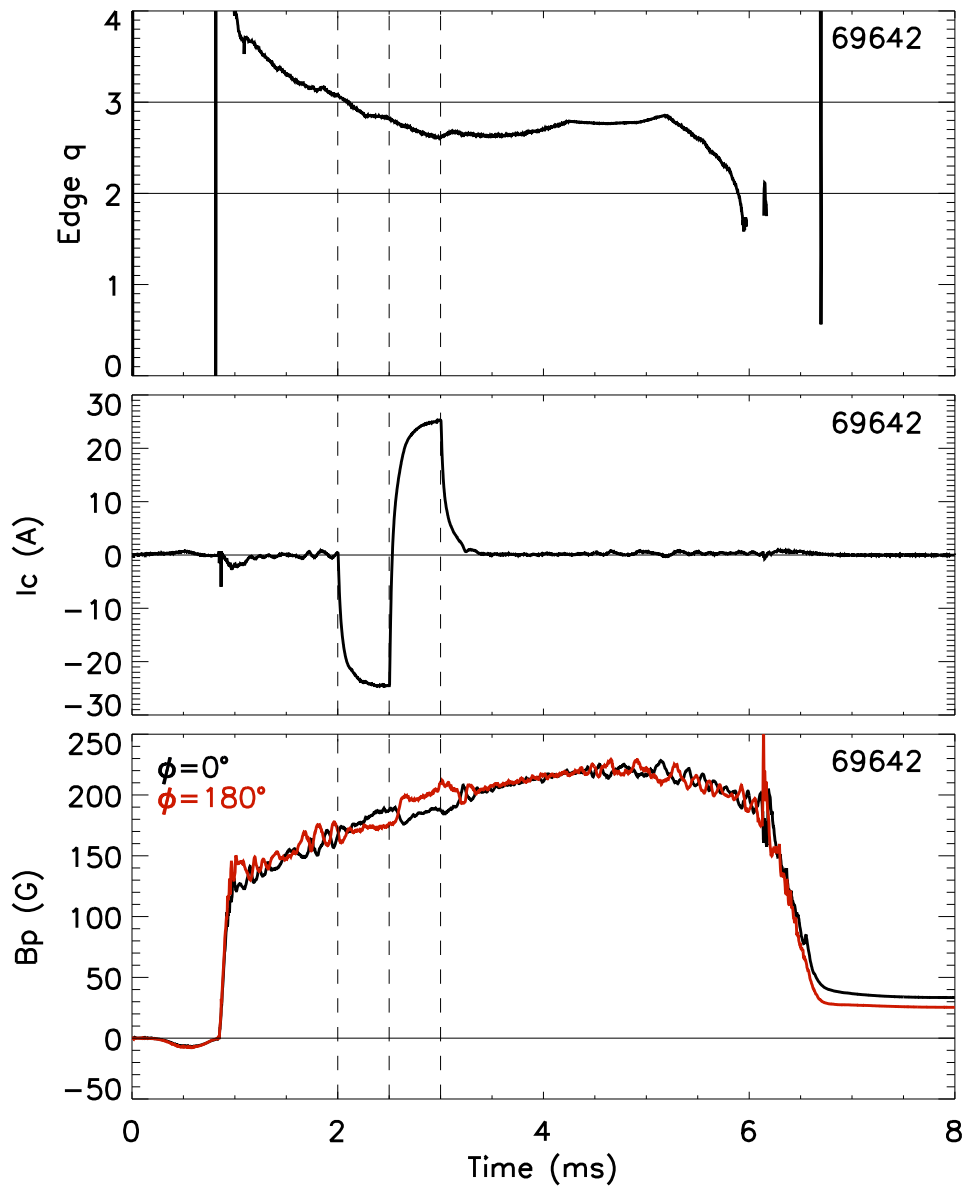
Figure 6.3: Typical q evolution, applied perturbation, and magnetic field for a phase-flip RMP shot.

assumptions being violated would be if the RMP triggers a major disruption, in which case the plasma does not return to the unperturbed state afterwards. It may still be possible in such cases to separate the 3D fields from the axisymmetric components, but each of these cases should be considered individually.

This method of polynomial fitting proves to be successful, but two arbitrary choices must be made in this process: the time period over which the fitting is performed, and the order of the fitting polynomial used. Based on trial and error, it was determined that the best results were given by fitting a fourth order polynomial over the 0.5 ms preceding the phase-flip and the 1.5 ms immediately following it. This is demonstrated in Figure 6.4, where the technique is applied to shots with and without a RMP. The timing of the polynomial fitting (which spans the duration of the RMP) is highlighted, so that the polynomial is being fit to the points shown in orange. This results in the green polynomial, which is the assumed evolution of the equilibrium field. This is seen to follow the measured field (black) well from 2 to 3 ms in the unperturbed case, verifying the validity of the method. In the perturbed case, the difference between measured (black) and fit (green) curves is then the perturbed magnetic field $\delta B(t)$, and this is seen to have a "phase-flip like" evolution. This polynomial fitting process is repeated for each of the magnetic sensors individually, to derive the full perturbed field dataset. Unless otherwise noted, these same parameters are used for the fitting of the equilibrium field in the remainder of this thesis.

We now have a measure of the perturbed field for each of the various arrays of magnetic sensors. This perturbed field data is shown for HBT-EP discharge 70000 in Figure 6.5, along with the timing of the applied phase-flip. Data from the poloidal and radial field sensors of the poloidal array, as well as a subset of the radial field feedback sensors are shown. Note the different color bars for poloidal and radial field. In all three arrays, a naturally rotating $m/n = 3/1$ mode is seen to exist prior to the applied phase-flip. For the poloidal field measurements, a $m = 3$ "phase-flip like" response, with two periods of opposing phase, is seen from 2 to 3 ms. After the RMP is turned off, the rotating mode is observed again. In the case of the radial field, the $m = 3$ structure of the response is seen clearly during the first half of the RMP. However, the effect of the conducting wall is more important for the radial field, and the response does not reverse until about 200 μs after the applied field
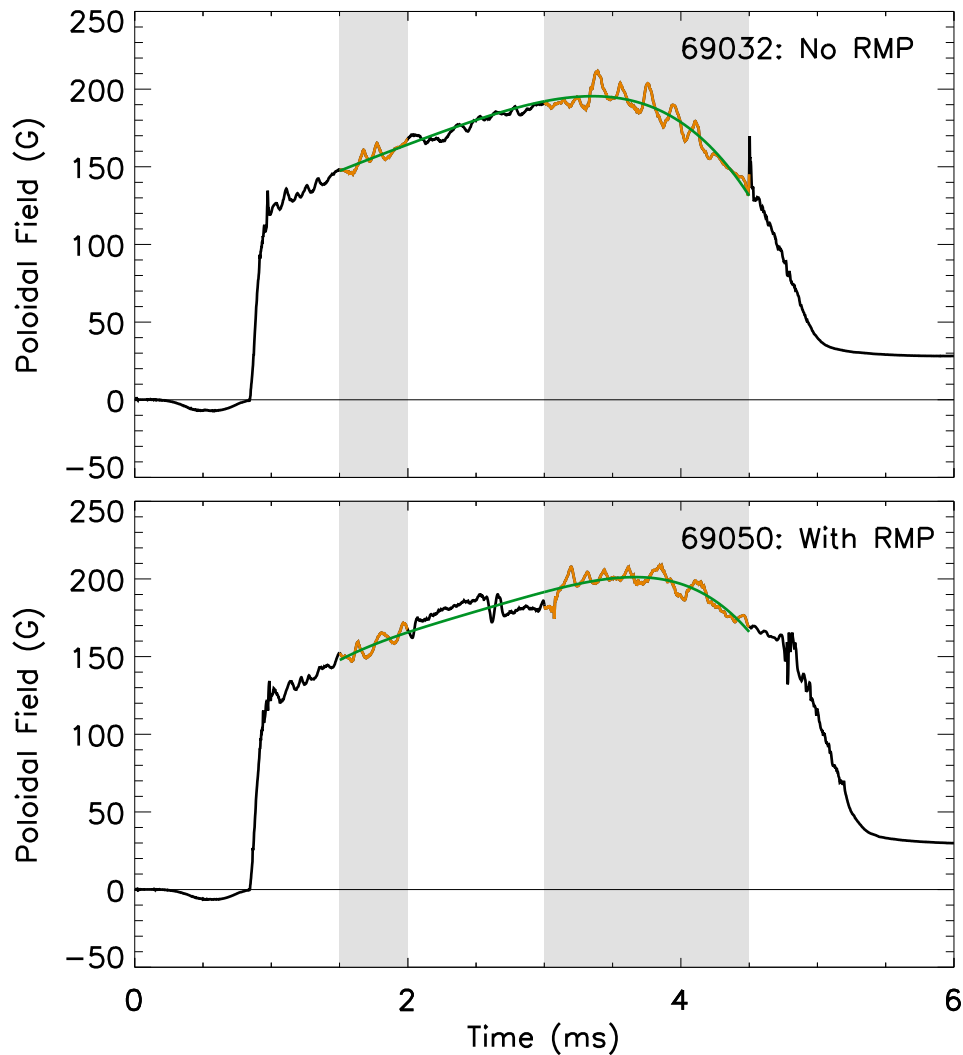
Figure 6.4: Examples of polynomial fitting of the equilibrium field, for an unperturbed shot (69032) and a shot with an applied RMP (69050). The highlighted region shows the period of the polynomial fitting. Thus the green polynomial is a fit to the points shown in orange, which occur before and after the RMP.

is reversed. Even at this point, the reversal of the radial field is slower than that of the poloidal field. This effect is most apparent for those radial sensors mounted directly on the conducting wall, which are those of the poloidal array located at $-90° < \theta < 90°$, and all of the feedback sensors.

Note that there are only 16 radial field sensors in the poloidal array, which is measuring
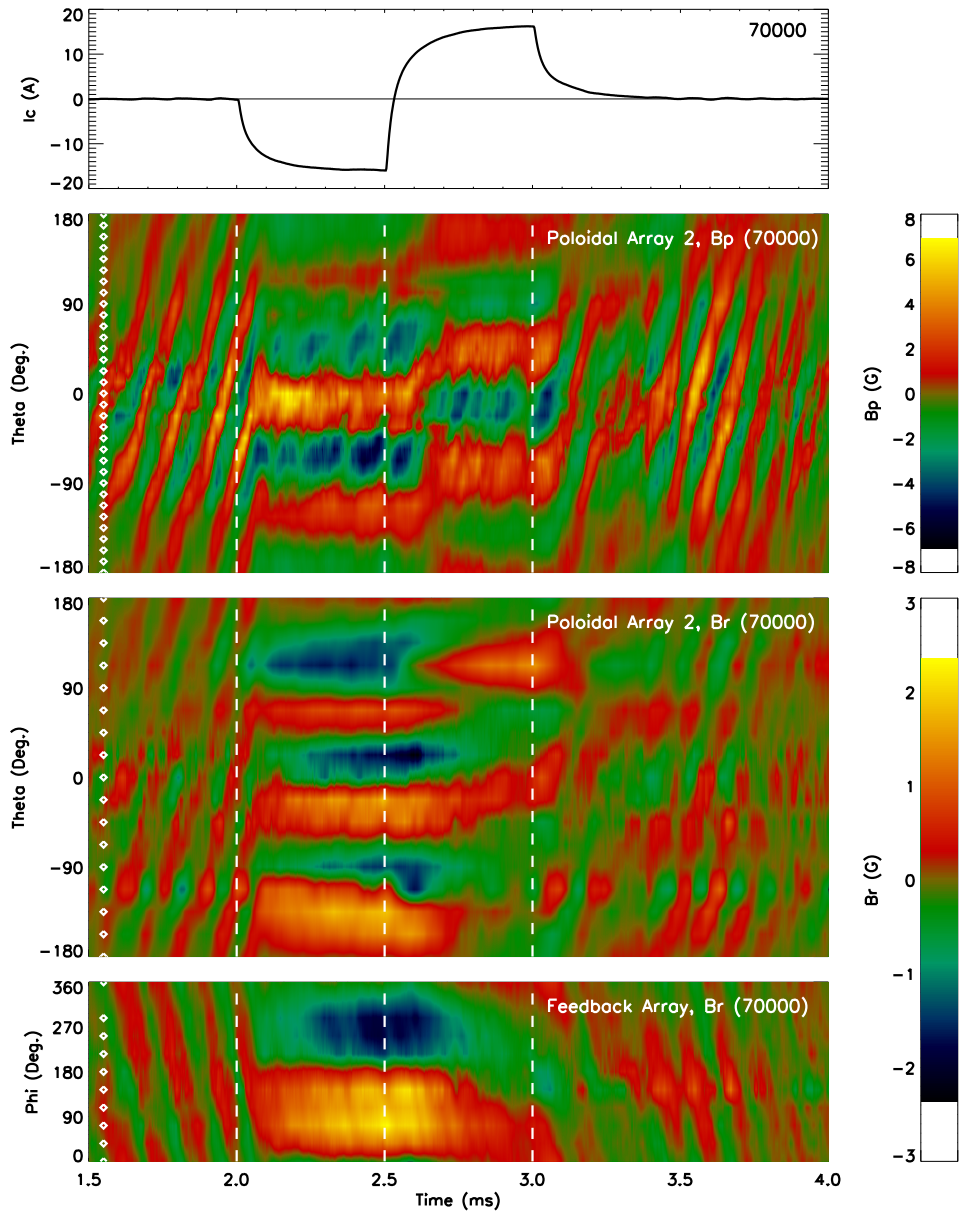
Figure 6.5: Measurements of the poloidal and radial field response to a phase-flip RMP, in HBT-EP discharge 70000. Note the different color bars for poloidal and radial field.

the $m = 3$ poloidal structure of the mode, while there are 10 sensors distributed toroidally in the feedback sensor array, which is measuring the $n = 1$ toroidal structure. Thus for radial field measurements, the feedback sensors actually have more phase-resolution than the "high-density" poloidal array, as can be seen during the radial field reversal ($\sim$2.7 to 3.2

ms) in Figure 6.5.

6.3   Plasma Response Phase

The plasma response to a phase-flip RMP has been clearly observed. Now we analyze the phase of this response relative to the applied field. Figure 6.6 shows the amplitude and phase of the Fourier $m/n = 3/1$ component of the control coil current, as well as of the radial and poloidal field feedback sensor signals. The feedback sensors are used here since they have
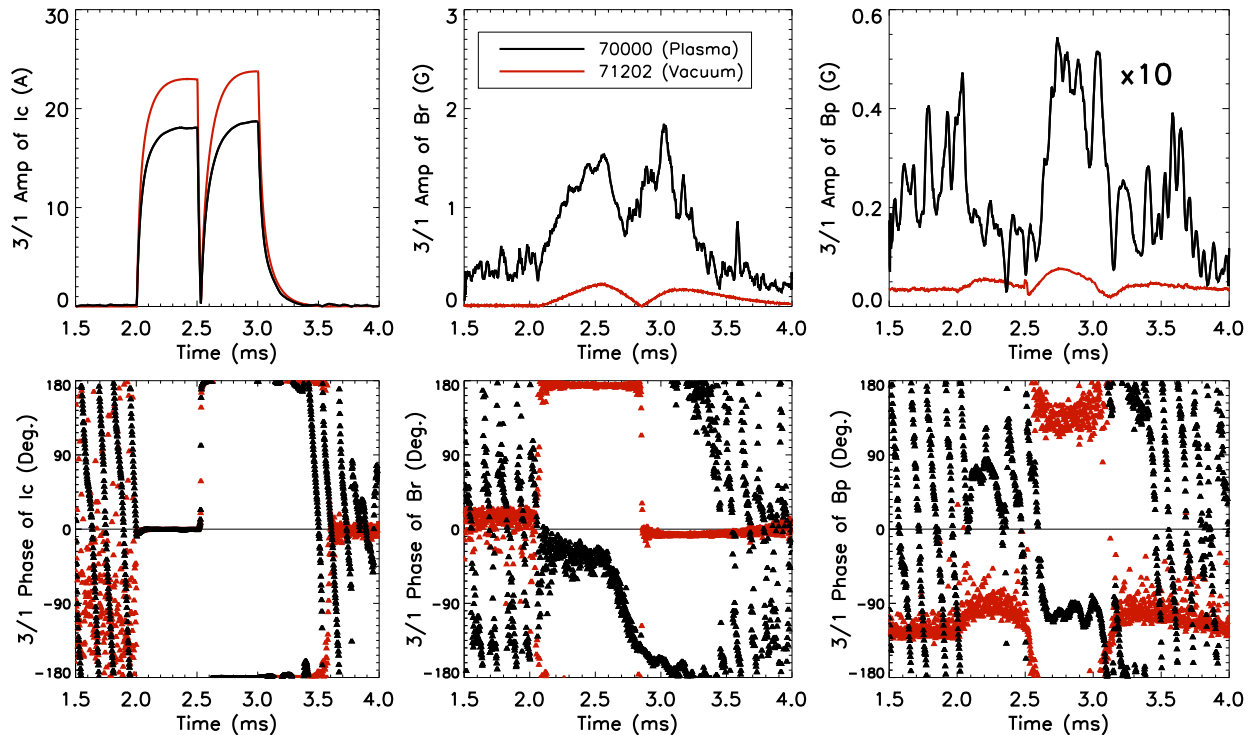
Figure 6.6: Amplitude and phase of the 3/1 component of coil current, radial field, and poloidal field. A vacuum shot and a plasma discharge are shown. Note that the amplitude of the poloidal field has been scaled down by a factor of 10 for the plasma discharge.

better phase-resolution for the radial field, as discussed previously. Data from a vacuum shot (red) and a plasma discharge (black) are compared. Since the sensors are mounted directly on the conducting wall, the detected radial field is delayed due to the effect of eddy currents.

In the vacuum case, the radial field pick-up is 180° out of phase with the coil current since each sensor is located midway between the toroidally adjacent coils, and thus measures the fringing return fields. Of course, the net applied 3/1 component of the radial field is aligned with the coil currents. Thus, since the measured radial field in the presence of a plasma is in this direction, the plasma response is seen to be an amplification of the applied resonant component. This same sign (180° from the vacuum pickup) is seen for the poloidal field sensors, and the radial and poloidal fields are approximately 90° apart.

The vacuum pick-up (which includes direct coupling as well as coupling to eddy currents) in the poloidal field sensors is seen to be quite negligible, having a maximum value of about 3.3×10^{-3} G/A in vacuum, compared to 0.28 G/A with plasma, or about 2 orders of magnitude lower than the measured plasma response. Similarly, the maximum value of the vacuum pickup in the radial field is about 10 times smaller than the measured plasma response.

6.4   Superposition of the Plasma Response

Because of the evolution of the plasmas studied here (a typical example being shown in Figure 6.3), which begin with the resonant $q = 3$ surface internal to the plasma and then moving outwards, the plasma becomes ideally unstable before the RMP is applied. Thus, as seen in Figure 6.5, a naturally rotating kink is usually observed prior to the RMP being applied. However, analysis of the plasma response at different RMP amplitudes is consistent with an externally driven response which is independent of the background MHD, and the total fluctuations can be described as a superposition of this rotating kink and the externally driven response. When the amplitude of the RMP is large, the total perturbed field is dominated by the phase-flip response, but at low amplitudes the rotating mode dominates.

This concept is illustrated by the following simple equation:

$$\delta B(\theta, \phi, t) = cos(m\theta + n\phi + \omega t) + A(t) \cdot cos(m\theta + n\phi + \delta) \tag{6.2}$$

where $A(t)$ is the phase-flip temporal evolution, and the plasma response is assumed to follow this evolution. δB has been scaled such that the amplitude of the rotating mode is normalized. Equation 6.2 is plotted in the left half of Figure 6.7 for the 0.5 ms preceding the phase-flip and for the first 0.5 ms of the RMP, corresponding to the "positive" phase of the phase-flip. Since the response is assumed to behave as $A(t)$, the plasma response is completely stationary during this phase. The helicity of the plotted mode is $m/n = 3/1$, and the results shown are for the poloidal array, with ϕ fixed. Three amplitudes for $A(t)$ are shown, ranging from 0.5 to 3.5.

When $A = 3.5$, the phase-flip response dominates, and the overall response of δB is non-rotating, although there are some small oscillations in the phase due to the effect of the rotating component. When $A = 1.5$ and the two modes become comparable in size, there is a more significant oscillation in the phase of the total 3/1 field, although there is still no net rotation. Finally, at $A = 0.5$, the rotating mode becomes dominant over the phase-flip response, and the total field is seen to undergo a full rotation around the plasma, although with significant modulations in the δB contours due to interference of the rotating kink and the stationary response.

These three cases of Equation 6.2 are compared to three experimental discharges with varying RMP amplitudes, shown in the right half of Figure 6.7. The same qualitative features described before are seen for the experimental data. At large amplitudes the phase-flip response dominates, although the periodicity of the rotating mode is still visible. At intermediate RMP amplitudes, the δB contours are seen to oscillate significantly. And at low amplitudes, the fluctuations make full rotations, but with significant modulation. These features of the experimental measurements are particularly clear near $\theta = -90°$, due to the low equilibrium position of the plasma.
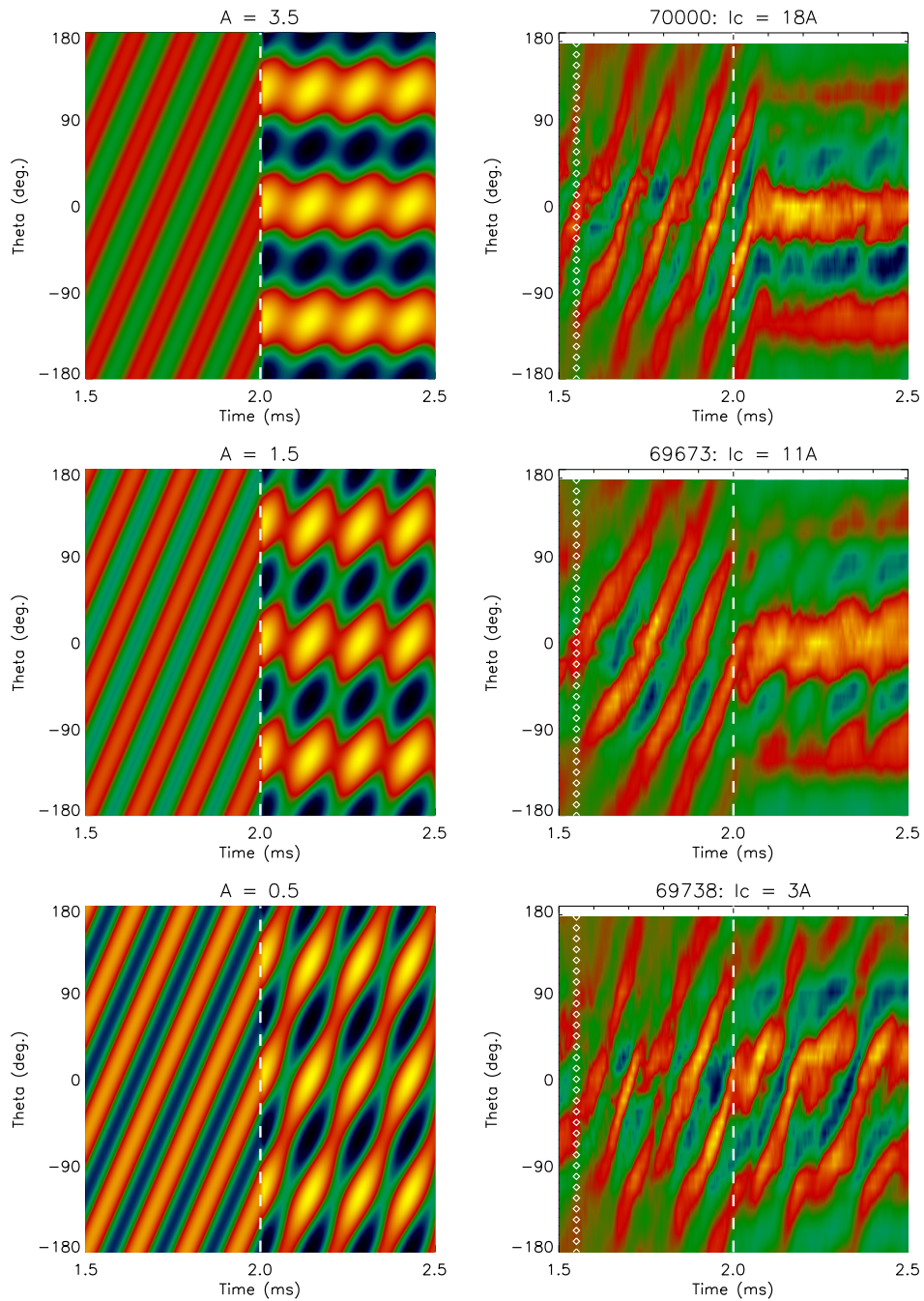
Figure 6.7: Superposition of rotating and non-rotating $m = 3$ modes of various amplitudes, as simulated by Equation 6.2 (left) and as detected experimentally (right).

Note that in Equation 6.2, both the rotating kink and the externally driven response are assumed to have identical spatial structures, each with their own temporal evolution. It is

the interference of these two identical spatial structures at different relative amplitudes and phases, which causes the modulations seen in the contours of δB.

6.5   Fitzpatrick-Aydemir Modeling

The equations of the Fitzpatrick-Aydemir model include the effects of external fields through the term ψ_c, so the dynamical plasma response to a phase-flip RMP can be modeled by integrating Equation 2.24. The parameters used in this simulation are summarized in Table 2.1.

This simulation is compared with the measured amplitude and phase of the 3/1 component of the radial and poloidal fields, as shown in Figure 6.8. An initial value of $\bar{y} = \bar{y}_1$ (the
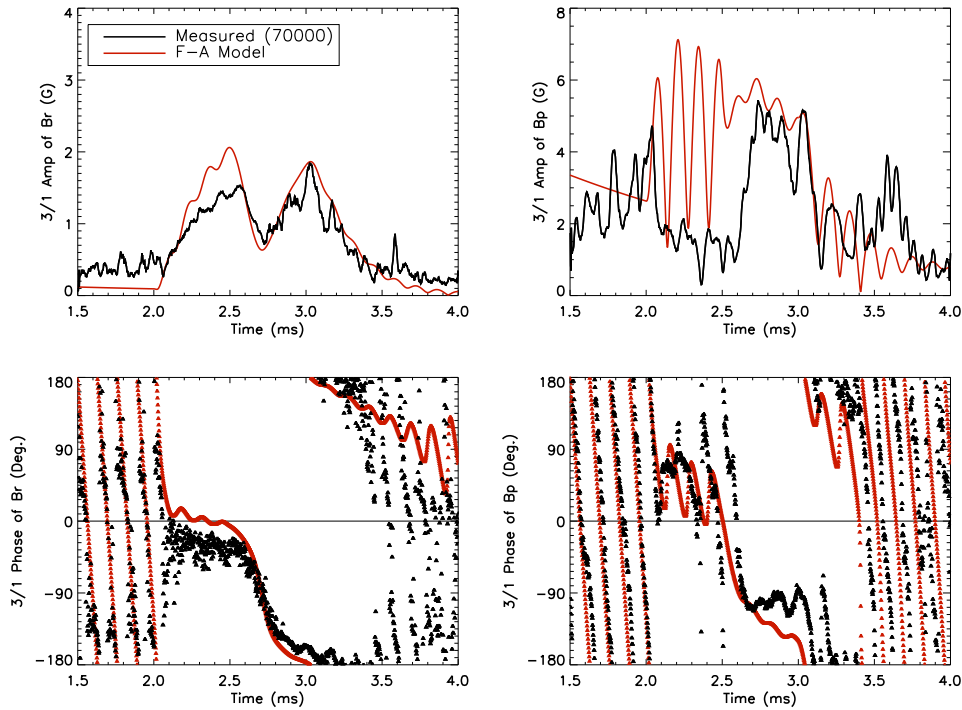
Figure 6.8: Comparison of Fitzpatrick-Aydemir modeling results with experimental measurements.

"plasma mode"), which has growth rate $\gamma_1 = (-0.49 + 2\pi7.6)$ ms^{-1}, is chosen. This is the naturally rotating kink observed before the the RMP is applied. The modeled phases of the poloidal and radial components of the plasma response agree well with measurements. The

relative and absolute phasing of the radial and poloidal fields in each of the two phases of the RMP, as well as the eddy current effects on the radial field reversal are all well captured. After the RMP, the mode returns to a rotating state, at least for the poloidal field. The amplitude of the radial response agrees well with the measured values, and the poloidal field amplitude is of the correct order.

One feature of this formulation of the Fitzpatrick-Aydemir model is its linearity, which means that in the presence of a ψ_c driving term, the total solution is a sum of the associated particular solution and the homogeneous solution. These are each interpreted as the externally driven response and the naturally rotating kink. Because the model is a single-helicity model, both solutions necessarily have identical spatial structures. This is precisely the physical picture presented in Section 6.4, where, for simplicity, the "particular solution" was assumed to have the temporal evolution $A(t)$. This empirical model was able to recreate many of the features of the poloidal field evolution. However, in the Fitzpatrick-Aydemir model, the particular solution behaves only approximately like $A(t)$, and has a slow drift as well as oscillations in phase and amplitude. This behavior is shown in Figure 6.9, along with the that of the empirical model. The slow drift and faster oscillation of the Fitzpatrick-
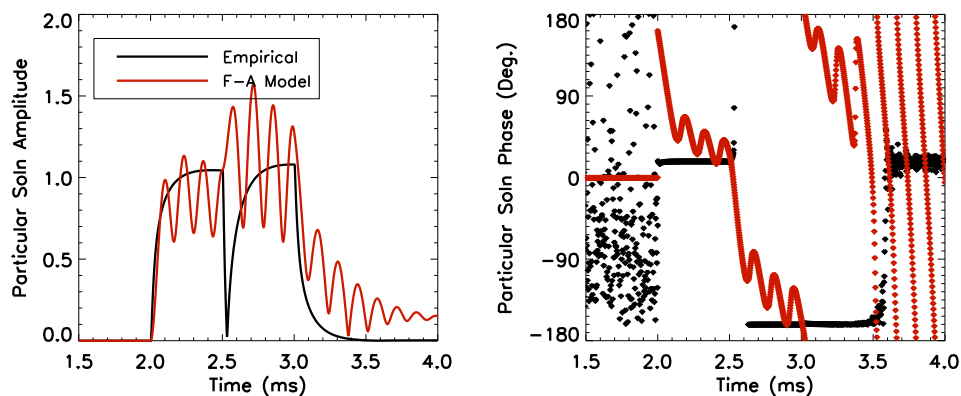
Figure 6.9: The temporal evolutions of the poloidal field particular solution, which corresponds to the externally driven plasma response, for the empirical model of Section 6.4 and for the Fitzpatrick-Aydemir simulation.

Aydemir solution is due to the excitation of both the slowly rotating "wall eigenmode" and rapidly rotating "plasma eigenmode", by the ψ_c driving term. The "wall mode" causes the slow drift during each phase of the RMP, while the "plasma mode" is responsible for the oscillations on top of this. However, the particular solution of the Fitzpatrick-Aydemir model is still approximately "phase-flip like", and despite their differences, both models are able to describe the qualitative features of the measurements shown in Figure 6.7, by the superposition of two independently evolving identically shaped modes. This was already shown for the empirical model, and is shown for the Fitzpatrick-Aydemir solutions in Figure 6.10. At different amplitudes of ψ_c, either the homogenous or the particular solutions become dominant, leading to the same qualitative differences in the δB contours seen experimentally.

6.6 Radial Field Response

Combining Equations 2.19 and 2.20 gives:

$$b_r(r) = \frac{im}{rR}\psi(r) \tag{6.3}$$

Since our sensors are mounted on the wall, the measured radial field will be $b_r = \frac{im}{bR}\psi_w$. Recall from Section 2.3, that the "plasma eigenmode", which was interpreted as the naturally rotating kink, has almost no ψ_w (relative to the magnitude of ψ_a), and thus almost no radial field (relative to the magnitude of the poloidal field). This is a reasonable result, since the rotation of this eigenmode is faster than the wall time ($f_1 > \gamma_w$), and can also observed experimentally in the first 0.5 ms of Figure 6.5. This means that the only way to see a large radial field (or equivalently, a large ψ_w), is to excite the "wall mode" by applying a RMP. However, this "wall mode" has a slow rotation rate (0.34 kHz), meaning that any large radial field signal seen by our diagnostics *must* be slow. In addition, there *cannot* be a faster oscillation on top of this, since such an oscillation would have to come from the "plasma mode", which has almost no ψ_w. In other words, the radial field from the "wall

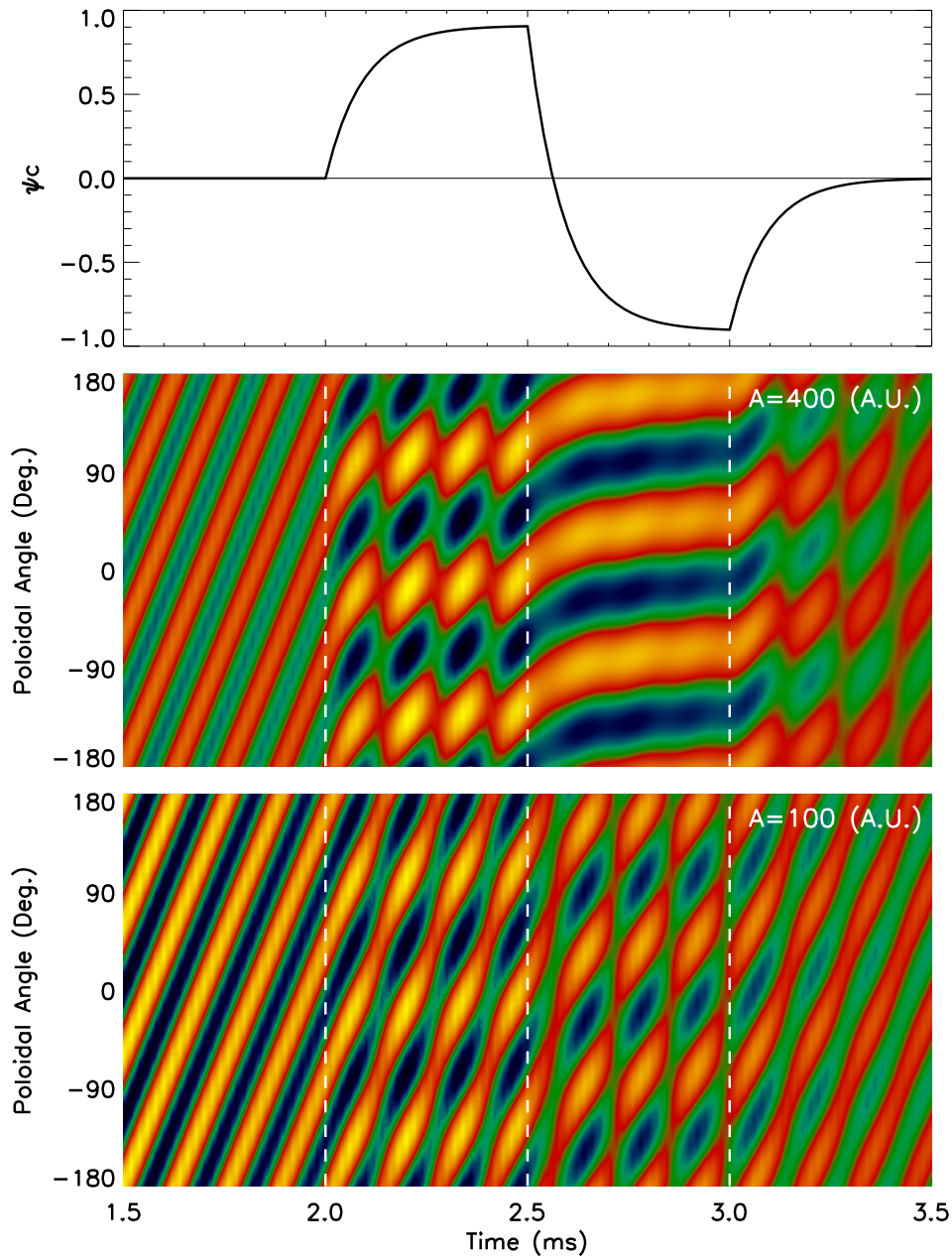Figure 6.10: Fitzpatrick-Aydemir simulations of phase-flip RMP response in the presence of a rotating kink, for two RMP amplitudes. The temporal evolution of the control coil flux is also shown.

mode" will almost always dominate over the radial field from the "plasma mode", and thus the measured resonant radial field will always have a very slow drift. The only exception

to this is in the special case that the "wall mode" amplitude is very small, so that the ψ_w which comes from the "plasma mode" and that which comes from the "wall mode" may be comparable, in which case there will be interference between these two frequencies. Thus the Fitzpatrick-Aydemir theory predicts that oscillations in the radial field will only be seen at low RMP amplitudes.

In Figure 6.11, we plot the radial field response from the same three plasmas shown in Figure 6.7. At the largest RMP amplitude, only the slow wall mode is observed. At the intermediate amplitude, a small component of the plasma mode may be seen, but the wall mode is still very dominant. Only in the lowest amplitude case are the ψ_w from the two eigenmodes comparable, and significant interference between the two are observed. This is in contrast to the poloidal field, which has order unity contributions from ψ_a and ψ_w, and thus usually has comparable components of the fast "plasma mode" and slow "wall mode", leading to more intereference effects over a wider range of RMP amplitudes, as seen in Figure 6.7, where the interference effects between the fast and slow eigenmodes can be seen even in the highest amplitude case.

6.7 Correlation Parameter

Since the plasma response is an amplification of the applied perturbation, we can quantify the amplitude of the plasma response at a sensor i using the following correlation parameter:

$$C_i = \frac{\int \delta B_i(t) I_c(t) dt / \int dt}{\sqrt{\int I_c^2(t) dt / \int dt}} \tag{6.4}$$

where $\delta B_i(t)$ is the perturbed field at sensor i, and $I_c(t)$ is simply the "phase-flip shape" shown in Figure 6.1, which does not depend on the choice of sensor index i. This parameter has units of Gauss, is independent of time, and represents the amplitude of the "phase-flip like" response at that location. If there is any oscillatory ($\gtrsim 1$ kHz of the phase-flip) component to the signal, such as a fast rotating mode, it will not contribute to this correlation
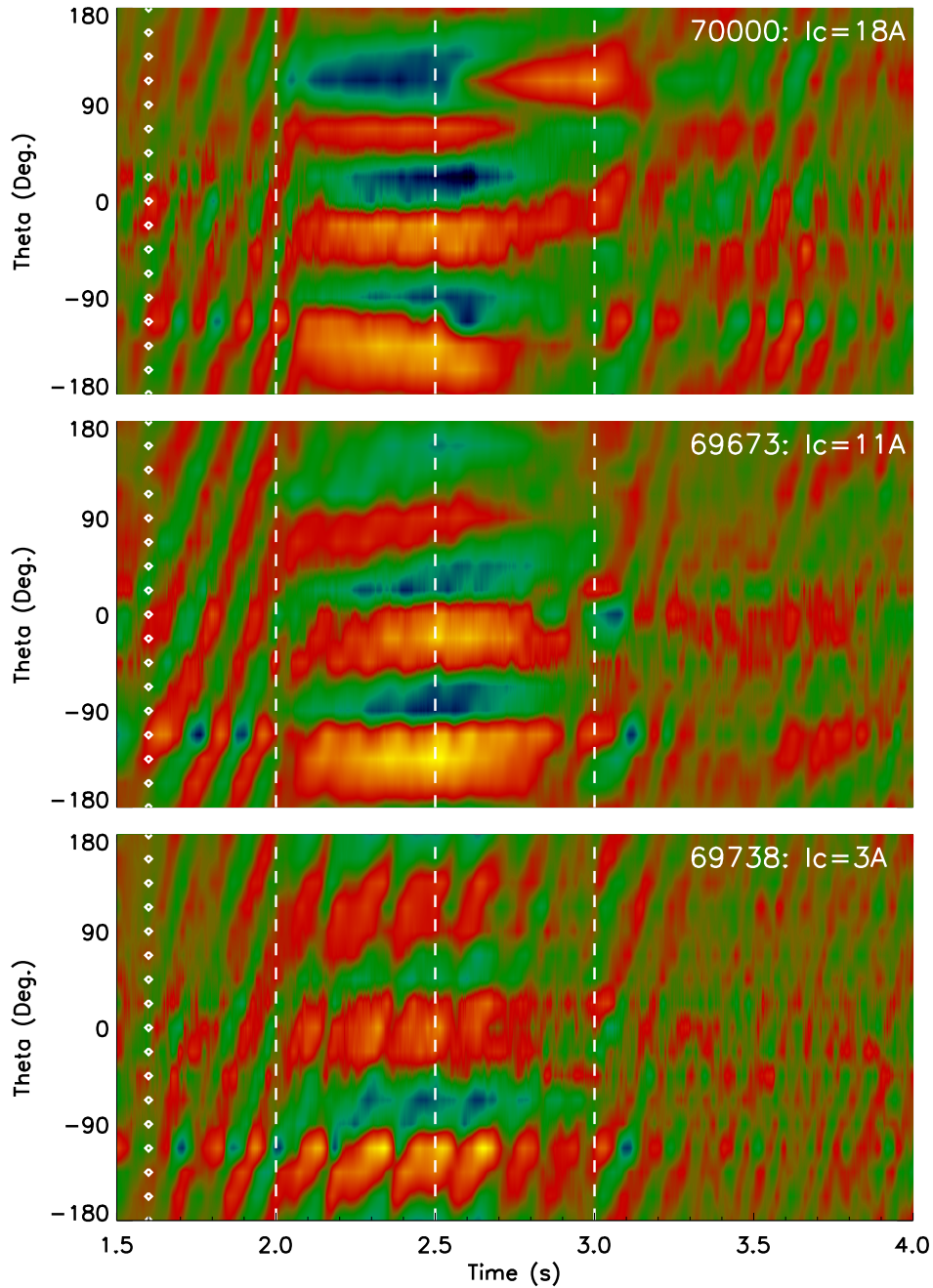
Figure 6.11: Radial field response to phase-flip RMPs at three different amplitudes.

parameter. Similarly, if there is any steady-state field in $\delta B_i(t)$ which is not removed by the polynomial fitting method, it should not contribute to C_i since $\int I_c(t)dt = 0$ for a phase-flip. The correlation parameter can take on positive or negative values based on the relative

phasing of $\delta B_i(t)$ and $I_c(t)$. Since this parameter is calculated individually for each sensor, we can determine the global structure (if any) of the plasma response.

Figure 6.12 shows (in blue diamonds) the correlation parameters for the 40 poloidal field feedback sensors, as calculated for shot 69103. The global structure of the plasma response to the applied phase-flip RMP is $m/n = 3/1$. In the previous chapter, the spatial structure of the rotating RWM was seen to also be $m/n = 3/1$. In fact, the BD spatial modes gave a direct measure of this mode structure, including a quadrature pair of modes that could describe any toroidal phasing of the mode. Thus it seems very natural to try to compare the mode structure of the naturally rotating kink and the RMP driven response. Using the BD spatial mode basis from shot 69094, we fit the correlation parameter measurements of shot 69103. This fit, also shown in Figure 6.12 as the red curve, is excellent. The two mode structures, measured in completely independent manners, and for different shots, are seen to be identical. This supports the empirical model described by Equation 6.2, which assumes a rotating kink and RMP response with identical spatial structures. It also justifies our use of a single-helicity model of kink mode dynamics.

It will be convenient in the future to continue to use this empirically determined BD basis to fit and quantify the phase-flip response, as shown here. The quality of the fit in Figure 6.12 demonstrates, once again, the advantage of using a BD basis. This basis also includes the next pair of 6/2 modes as well for the measurement of multimode effects.

Finally, several more features of this correlation parameter are also worth noting. Because this measure of the plasma response is based on a correlation, it will usually tend to underestimate the plasma response, for example, if there is a slight delay in the response relative to the applied field, or if the equilibrium evolves such that the response is larger in one half of the phase-flip than the other. Our parameter, as defined, is unable to account for such effects. Another nuance comes from the always present coupling between natural modes and the coil currents $I_c(t)$ as discussed in Section 5.4. This means that at low RMP amplitudes,
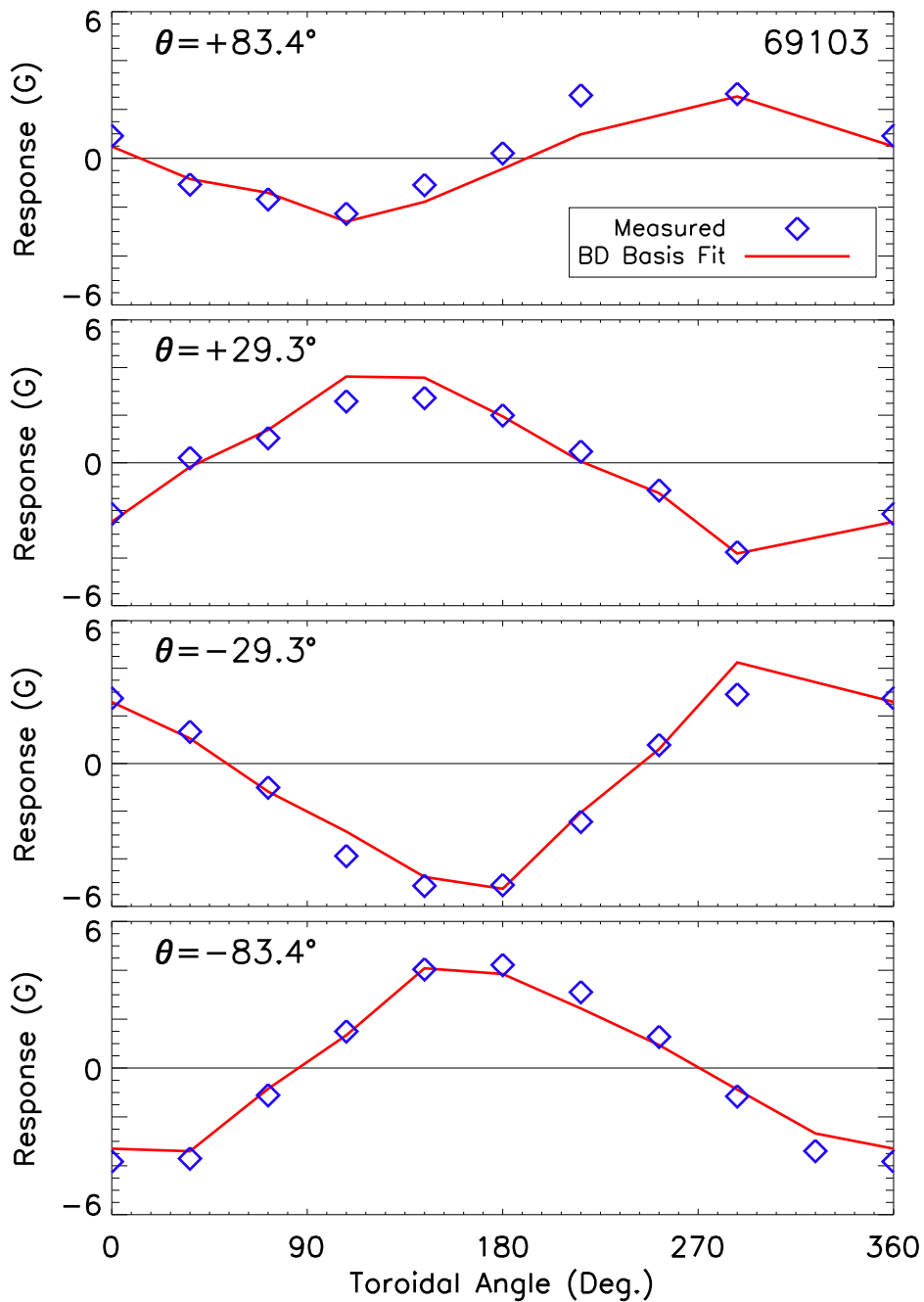
Figure 6.12: Correlation parameter measure of phase-flip response from shot 69103, and a fit of this structure with the BD basis from shot 69094.

much of the experimentally measured $I_c(t)$ could be due to coupling to a rotating mode. In this case both $I_c(t)$ and $\delta B_i(t)$ will be measuring the same rotating mode, resulting

in a large correlation between the two signals (numerator of Equation 6.4), inflating the measured response even when there is little or no "phase-flip like" response. This can be avoided by measuring $I_c(t)$ from an equivalent vacuum shot, for example. Finally, the limits of integration in Equation 6.4 were intentionally left ambiguous. Here we have simply used the duration of the phase-flip pulse as the limits, but different values could be used, for example if there were a delay in the plasma response.

Chapter 7

Active MHD Spectroscopy Experiments

The technique of active MHD spectroscopy probes the plasma by applying external magnetic fields to excite an MHD response [14, 15]. Here we apply the techniques developed in the previous chapter to understand, in detail, the plasma response to phase-flip perturbations. We describe the measured plasma response as a function of external field helicity and amplitude, as well as plasma q and rotation. Multimode effects in $m/n = 3/1$ as well as $6/2$ phase-flip experiments are described.

7.1 Helicity Scan

The resonant nature of the plasma amplification of the applied external field can be seen by varying the spectrum of the applied field. In this experiment, a series of $n = 1$ phase-flip magnetic perturbations are applied while varying the poloidal mode number spectrum on a shot-to-shot basis. Each control coil is energized with:

$$I(\theta_i, \phi_j, t) = A(t)cos(m\theta_i + \phi_j) \tag{7.1}$$

where $A(t)$ is the phase-flip evolution shown in Figure 6.1. The perturbation amplitude was chosen such that the peak value of $A(t)$ is 10 A. These perturbations are applied to the standard current ramp type shot shown in Figure 6.3. The phase-flip is applied in these shots after the $q = 3$ surface has gone external. The applied phase-flips are all dominantly $n = 1$, however the m number in Equation 7.1 is allowed to vary continuously between shots, rather than being limited to just integer values. This continuously varies the amplitude of the resonant 3/1 component applied to the plasma. The solid curve in Figure 7.1 shows the amplitude of the applied resonant component as a function of the m parameter used in Equation 7.1. This is calculated by taking the inner product between the applied currents
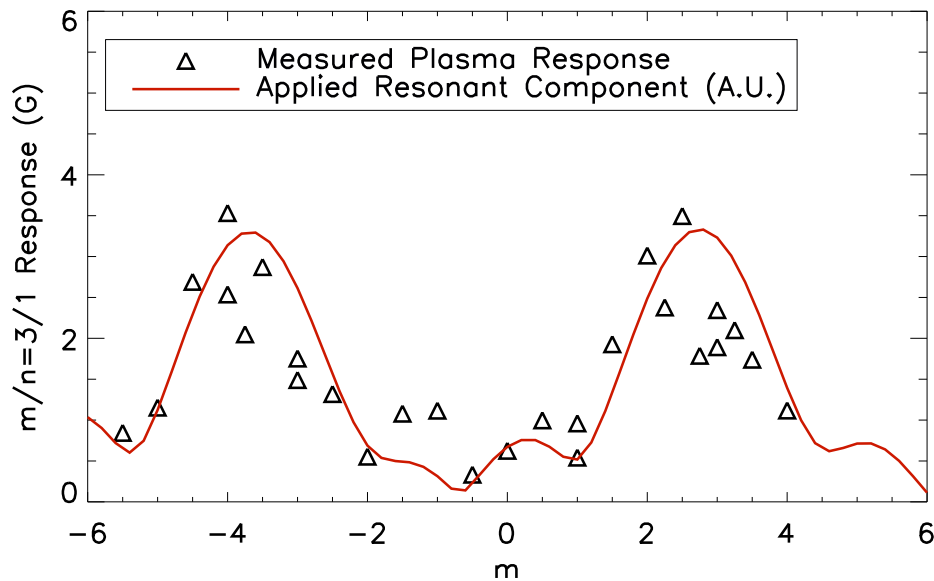
Figure 7.1: External perturbation helicity scan, parameterized by the continuous variable m in Equation 7.1. The solid curve is the calculated amplitude of the applied 3/1 component, and the triangles are the measured plasma response for each shot. Each triangle represents an individual discharge.

as given by Equation 7.1, and the empirically measured "optimal coupling" configuration determined by biorthogonal decomposition, as shown in Figure 5.6. The two peaks for positive and negative m values are the result of aliasing due to the limited poloidal resolution

of the control coil array.

Analysis of the detected plasma response in individual shots, in the manner of Figure 6.12, shows that the plasma response does in fact have a 3/1 structure, independent of the chosen m number. Overplotted in Figure 7.1 are the measured amplitudes of this 3/1 response from each of these shots, where each triangle represents an individual discharge. It is clear that the plasma response is proportional to the amplitude of the applied resonant field. Thus the "phase-flip like" response, which is superimposed with the natural rotating mode, is a resonant field amplification (RFA) [39]. This observation also justifies our use of a single-helicity model of kink mode dynamics in the previous chapter.

7.2 Edge q Scan

The RFA of the phase-flip is a resonance between the helicity of the applied magnetic perturbation and that of the equilibrium magnetic field, so that in addition to varying the helicity of the perturbation, there should be a similar trend as the plasma edge q varies. This is quite easy to do, since the applied field can be reproduced identically for each discharge, while the natural shot-to-shot variability in the plasma equilibrium (due to uncontrollable vacuum impurity levels, for example) provides a convenient scan of the edge q. Here we choose a fixed value of $m = 3$ in Equation 7.1, which is the configuration which, as shown in the previous helicity scan, gives close to the maximal plasma response. $A(t)$ is again chosen to have a peak current of 10 A, which results in a normalized resonant perturbation of $B_r^{3/1}/B_T = 0.001$. Unfortunately, the equilibrium in a typical HBT-EP plasma evolves on the order of milliseconds, so that the edge q is not truly constant during the 1 ms window when the phase-flip is applied. Thus, we characterize each plasma using the value of the time-averaged q during the applied phase-flip. Because the equilibrium evolution is slow compared to this time span, the time-average gives a good representation of the equilibrium during that period. Figure 7.2 shows the measured 3/1 response as a function of time-averaged edge q, where

again each datapoint is the measured response for a single discharge. The resonant nature
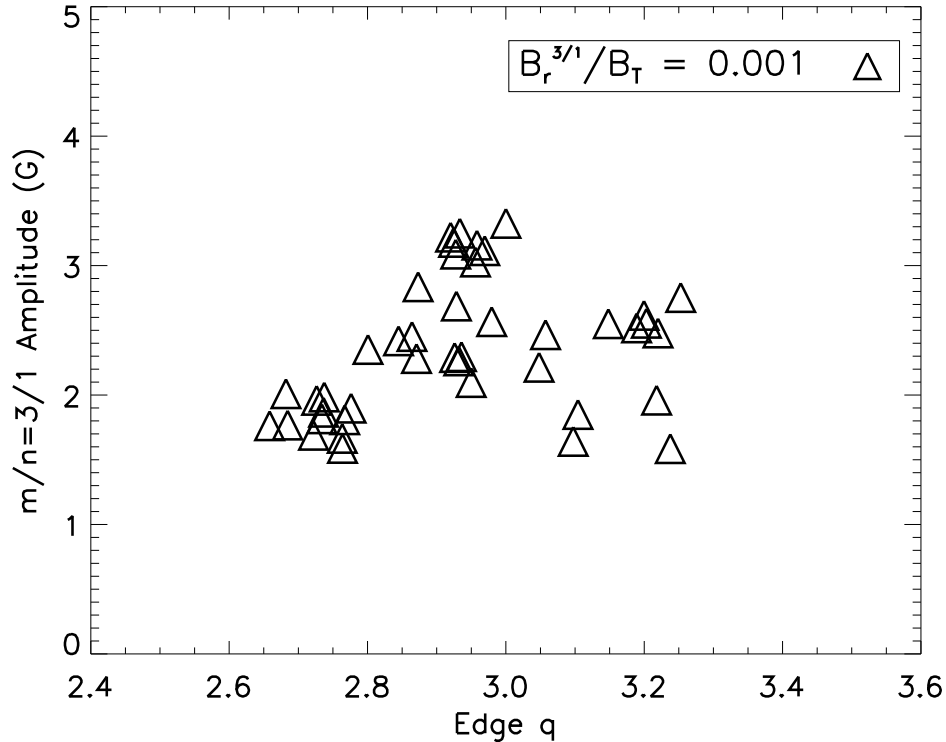
Figure 7.2: 3/1 plasma response as a function of time-averaged q, at fixed RMP amplitude. Each datapoint represents an individual discharge.

of the plasma response is once again evident. The peak in the response is seen to occur at slightly below $q = 3$, when the resonant surface is just outside the plasma surface.

7.3   Amplitude Scan

The plasma response was also measured as a function of the RMP amplitude, given by $A(t)$ from Equation 7.1. When the RMP amplitude is scanned, three different regimes of plasma response are observed: the linear, staturated, and disruptive regimes. Each of these are described here.

- In the *linear regime* of plasma response, which is observed in all plasmas, the amplitude

of the plasma response scales linearly with the applied field.

- In the *disruptive regime*, which occurs at the largest perturbation amplitudes, the phase-flip RMP causes a major disruption of the plasma either during or immediately following the RMP. This is observed to occur in all plasmas for perturbations larger than about $B_r^{3/1}/B_T > 0.003$.

- In the *saturated regime*, the plasma response no longer increases with increasing coil current. This regime is only observed in plasmas that are near resonance ($q \approx 3$). In this case, the plasma transitions from the linear to saturated regime for $B_r^{3/1}/B_T > 0.0015$, all the way up to the disruptive regime.

In plasmas which are further from resonance, the linear response is observed to continue right up to the onset of disruptions. This is shown in the top plot of Figure 7.3, where the discharges from the amplitude scan have been separated by the time-averaged edge q. Shown in the bottom plot are the plasmas near resonance, where both the linear and saturated regimes can be seen. Shots in the disruptive regime are not shown in either plot, as they violate the assumptions from Section 6.2 which are part of quantifying the plasma response.

7.4   Saturation of Plasma Response

The saturation mentioned in the previous section can be seen in another manner, by performing a q scan at higher amplitude. In Section 7.2, the plasma response was measured as a function of edge q at a RMP amplitude of $B_r^{3/1}/B_T = 0.001$, which falls in the linear regime for both near-resonance and lower q plasmas. We now perform the same scan but at twice the previous amplitude, $B_r^{3/1}/B_T = 0.002$, which should fall in the saturated regime for near-resonance plasmas. If the plasma response were always linear, then the new curve should have the same shape as before, but at twice the amplitude. If there is saturation,

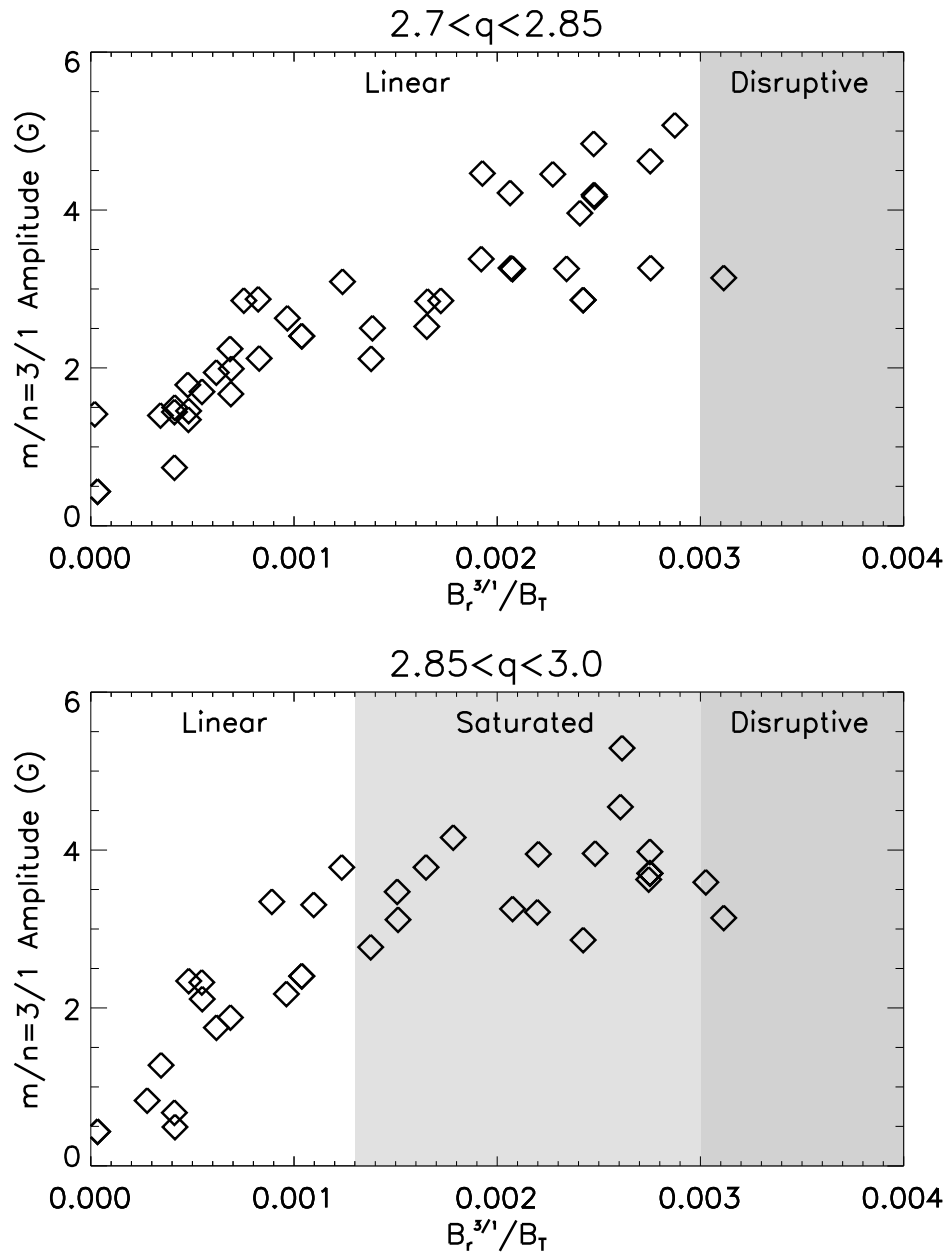Figure 7.3: Plasma response as a function of the applied RMP amplitude, sorted by time-averaged edge q. The three regimes of plasma response are shown.

the response would be less than twice the previous amplitude, resulting in a different shaped curve of plasma response as a function of RMP amplitude. Figure 7.4 shows the results of both scans. At lower q, the response is seen to double, indicating a linear scaling. However,
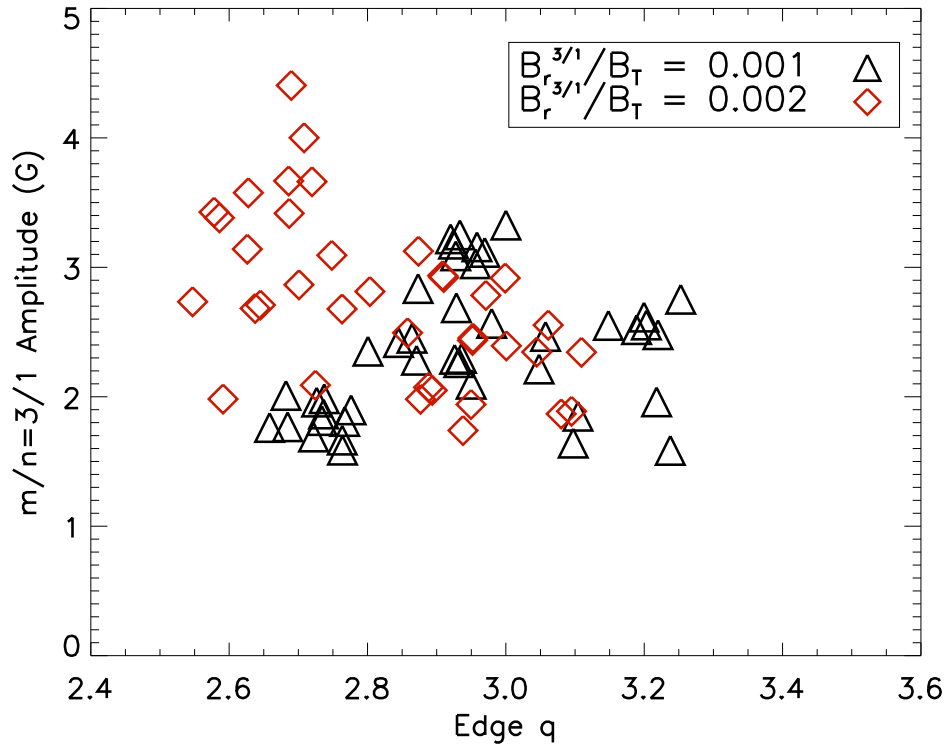
Figure 7.4: Comparison of 3/1 plasma response as a function of time-averaged edge q, for two values of RMP amplitude. The red points have double the amplitude of the black points, which were shown previously in Figure 7.2

near resonance, the measured response is the same level despite the larger perturbation, indicating saturation.

Thus the saturated response has now been observed through a full amplitude scan, as well as through more detailed sampling at two separate amplitudes, as a function of q. In both cases, the saturation is only observed to occur when the plasma is near resonance, and when the RMP amplitude is large. This is precisely when the distortion of the plasma edge will be the largest. Thus it seems possible that the saturation mechanism is related to increased edge interactions with limiting surfaces in the machine. This should lead to increased D_α light due to enhanced plasma-neutral interactions at the plasma edge. In fact, such an increase in D_α light for larger perturbations is observed, as shown in Figure 7.5. The

Figure 7.5: D_α light signal as a function of time, for several shots of varying RMP amplitude. The dotted lines denote the time period when the phase-flip RMP is applied.

top plot shows individual traces of D_α light for various RMP amplitudes, with the duration of the applied RMP highlighted. The largest of these coil currents, $I_c = 24A$, corresponds

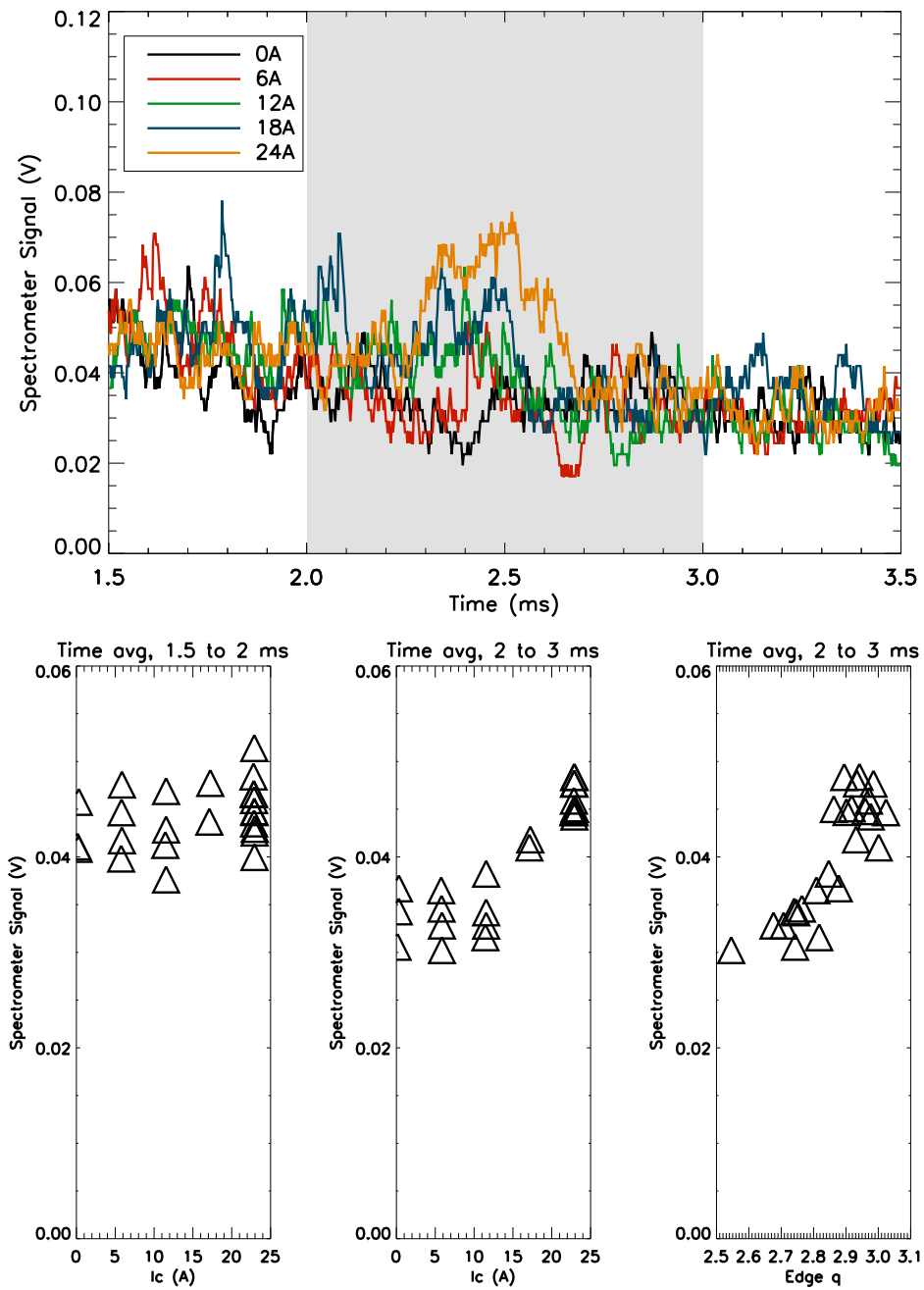to a perturbation of $B_r^{3/1}/B_T = 0.0024$, which is in the saturated regime. The bottom three plots summarize these results for a larger number of shots. The first of these shows that the average level of D_α light before the RMP is reproducible across all shots. When the average light level is calculated during the duration of the RMP, this level increases significantly with coil current, as the second of the three plots show. Finally, there is a similar increase in light as the $q = 3$ surface becomes closer to the plasma edge, or increased resonance.

Thus it seems plausible that the plasma response to the external magnetic perturbation is limited in amplitude by some mechanism involving physical distortion of the plasma edge and the resulting interaction with limiting surfaces. This leads to saturation of the plasma response at large perturbation amplitudes when the plasma is near resonance.

7.5 Rotation Scan

Theoretical models predict increased RFA at low plasma rotation [39]. As mentioned in Section 5.1, the magnetic fluctuations in HBT-EP are observed to travel with the electron fluid. Furthermore, we are able to control the rotation in the edge region of HBT-EP plasmas with an electrically biased probe which exerts a $j \times B$ torque on the plasma. While natural RWMs in HBT-EP plasmas rotate at 5-8 kHz, a bias probe current of 40 A is sufficient to bring the mode rotation to approximately zero. Bias currents larger than this are even able to reverse the direction of the mode rotation to the co-I_p direction.

Figure 7.6 plots the measured plasma response as a function of the bias probe current, at a perturbation amplitude of $B_r^{3/1}/B_T = 0.001$, which is still in the linear regime. The bias probe is at a fixed location 4 cm into the plasma edge for the duration of the discharge, but the bias is only applied 0.5 ms into the discharge, after which it remains biased for the duration of the shot. This application of the bias occurs about 0.5 ms prior to the start of the phase-flip. The value of the bias probe current used here is the time-average from the RMP duration.
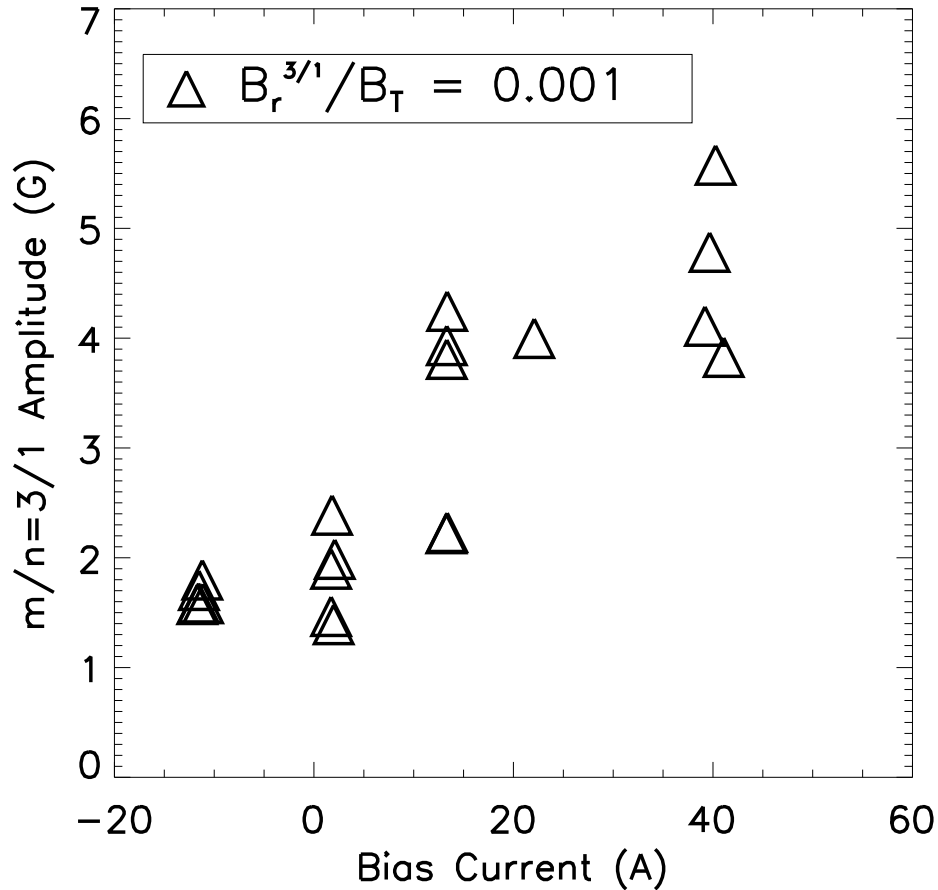
Figure 7.6: Effect of plasma bias and rotation on RFA.

As the edge plasma rotation is slowed, there is a dramatic rise in the plasma response. At near zero rotation ($\sim$40 A bias current), the response as calculated by the correlation parameter is nearly a factor of three larger than in the unbiased case. However, as discussed in Section 6.7, the correlation parameter can often underestimate the magnitude of the response. These biased shots are a good example of this, where the response can often rapidly increase, such that the correlation between $\delta B(t)$ and $I_c(t)$ is decreased. Nonetheless, the correlation parameter is still able to capture this increase in plasma response.

7.6   Multimode Effects

So far we have focused on both the application and detection of $m/n = 3/1$ fields. However, we know that there will always be sideband fields created by our modular coils. We have also seen in Chapter 5 that naturally occuring 3/1 RWMs are accompanied by a 6/2 RWM as well. Thus it seems natural to look for a 6/2 response in the 3/1 spectroscopy experiments.

Figure 7.7 shows the magnitude of the 6/2 plasma response in the same q scan dataset shown in Figure 7.2. Thus this is the 6/2 response to a 3/1 RMP, as a function of the
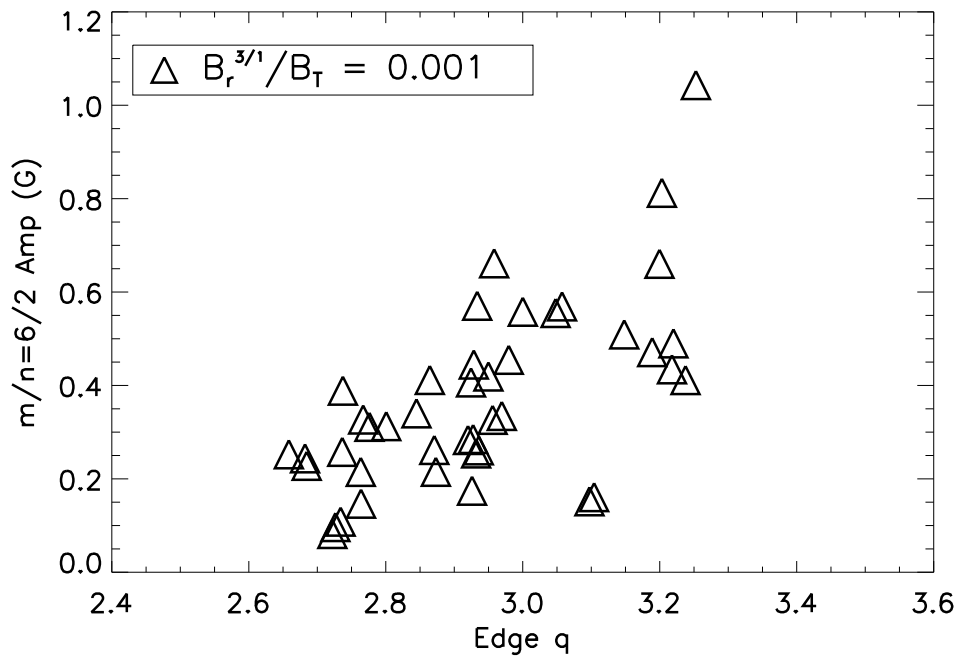
Figure 7.7: 6/2 response as function of edge q.

(time-averaged) edge q. As expected, the 6/2 response is much smaller, being below a Gauss for most shots. However, there appears to be a trend of increasing response with higher q, including values of q higher than 3. This is in contrast to the peaking of the 3/1 response at q values slightly below 3 (or the $q = 3$ surface just outside the plasma).

There is currently no theoretical basis by which to expect an increased 6/2 response at higher q. However, it seems clear that the 3/1 and 6/2 components of the response are

independent. This is in agreement with the observations of the independent evolution of the 3/1 and 6/2 RWMs in Chatper 5.

Given this observation of independent 3/1 and 6/2 behavior, it may be possible to apply a $n = 2$ magnetic perturbation to directly interact with the 6/2 mode, rather than through sideband harmonics of some other configuration. However, it should be noted that due to the limited (4 point) poloidal resolution of the control coil arrays, it is not possible to apply as large a resonant $m = 6$ component.

Figure 7.8 shows the results of this 6/2 phase-flip amplitude scan as a function of coil current. Direct measurements of the vacuum pickup, as well as total signals from plasma shots, are shown. The vacuum pickup behaves as expected, being proportional to the coil current and having a well-defined phase. When a plasma is present, the amplitude of the measured 6/2 component is elevated, and the phase is still well-defined, but distinct from the vacuum case. These facts indicate that there is some measurable 6/2 plasma response, although the amplitude is only fractions of a Gauss. Although the dataset is still small, there does not seem to be any indication of saturation of the 6/2 plasma response, nor were any disruptions induced with these perturbations. This is not surprising, since the amplitude of the applied 6/2 component is quite small.

While the detected responses were small, the evidence for direct interaction with the 6/2 mode is exciting. It raises the possibility of $n = 2$ feedback, possibly in conjunction with $n = 1$ feedback to prevent sideband destabilization of this mode. But as seen in this experiment, the coupling to this mode is quite small, likely due to the limited poloidal resolution of the control coils, which makes it difficult to apply much of a $m = 6$ structure. More detailed $n = 2$ feedback or MHD spectroscopy experiments would likely require increased poloidal resolution.
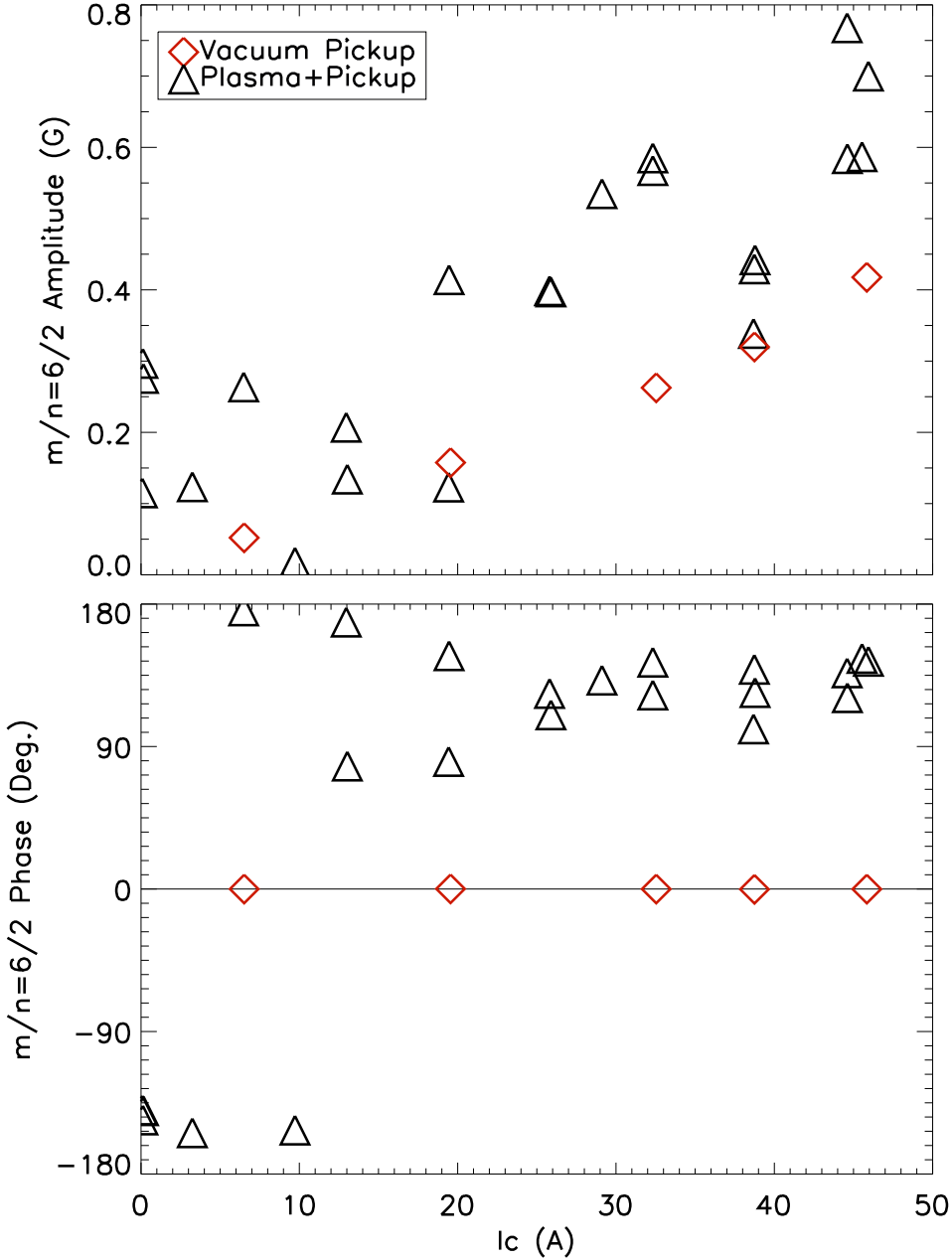
Figure 7.8: Applied 6/2 phase-flip, amplitude scan.

Chapter 8

Conclusions and Future Studies

The work presented in this thesis is the first set of passive and active MHD spectroscopy experiments conducted on the upgraded HBT-EP device. Here, the major technical and scientific results of this thesis are summarized. Due to the significant experimental upgrades, there is much potential for future work in this subject, and these possibilities are also outlined.

8.1   Conclusions

The design, construction, and calibration of a new array of magnetic diagnostics and coils were completed, and the first measurements and studies of natural and driven MHD phenomena have been reported. The key technical achievements of this work are:

- The capabilities of the HBT-EP experiment have been significantly extended with the construction of a new adjustable conducting wall, high-power modular control coil arrays, and an extensive magnetic diagnostic set. The large magnetic diagnostic system includes 216 magnetic sensors that allow high-accuracy, high-resolution detection of multimode MHD phenomena.

- A unique new in-situ calibration technique has been developed and implemented for

magnetic diagnostics in a tokamak device. This technique combines accurate measurements of eddy currents in the conducting wall with the "magnetic triangulation" method of reconstructing sensor positions, utilizing a set of calibration coils installed near the location of the nominal plasma current centroid. Results of this calibration have been validated with metrology data, and compared with VALEN simulations to characterize the electromagnetic properties of the conducting wall.

The major new physics results of this thesis are as follows:

- Detailed measurements of naturally rotating RWMs result in the first clear detection of multimode effects in HBT-EP plasmas, with the simultaneous existence of $m/n = 3/1$ and $6/2$ rotating modes. Mode numbers as high as $n = 3$ are also seen. The different toroidal rotations of the $3/1$ and $6/2$ modes unambiguously shows the independent nature of the two modes, demonstrating the non-rigid multimode nature of the current-driven external kink in HBT-EP plasmas.

- The resonant field amplification of a "phase-flip" RMP is observed simultaneously with the presence of an existing rotating kink. The spatial structures of both the naturally rotating kink and the externally driven plasma response are observed to be identical, while their temporal evolutions are approximately independent. This behavior is consistent with the predictions of a linear single-helicity model of kink mode dynamics.

- The externally driven plasma response is measured as a function of RMP amplitude, and three different regimes of plasma response are observed: linear, saturated, and disruptive response. The saturation of the plasma response occurs at large RMP amplitudes when the plasma is near resonance, and interaction of the perturbed plasma with limiting surfaces is proposed as a possible mechanism for the saturation.

8.2 Future Studies

Several immediate extensions of the work in this thesis are possible. This includes simple variations of these MHD spectroscopy experiments to study the effects of partial coverage (muting of various subsets of control coils), coil modularity (use of the differently sized coil arrays), or plasma-wall coupling (retraction of the shells). A planned installation of a divertor coil on HBT-EP is currently in the design phase, and is predicted to have a significant impact on the multimode spectrum of the plasma [45]. Both passive and active MHD spectroscopy experiments in the presence of a poloidal field null are likely to produce new results.

The detailed magnetic measurements made possible by the new diagnostic system, should also enable a wide range of future work in related areas. The simultaneous measurements of the radial and poloidal field over the surface of the plasma gives, in principle, a measure of the Maxwell stress tensor outside the plasma, and therefore the transfer of momentum between the wall, coils, and the plasma. This should give a measure of the torque exerted on the plasma and its MHD modes by the external coils, allowing a quantitative study of the momentum balance and rotation of the plasma.

The passive MHD spectroscopy techniques described here can also naturally be applied to the study of tokamak disruption physics. The high-resolution magnetics data now routinely collected on HBT-EP, where every discharge ends with disruption, provides an extremely large database from which to study the potentially complex MHD precursors which trigger these disruption events.

Finally, the experimental and analysis techniques developed here will be relevant to planned multimode RWM feedback studies and the development of advanced digital control algorithms, which have been identified as key goals of the HBT-EP research program [45].

Bibliography

[1] M. Shimada, D. Campbell, V. Mukhovatov, M. Fujiwara, N. Kirneva, K. Lackner, M. Nagami, V. Pustovitov, N. Uckan, J. Wesley, N. Asakura, A. Costley, A. Donn, E. Doyle, A. Fasoli, C. Gormezano, Y. Gribov, O. Gruber, T. Hender, W. Houlberg, S. Ide, Y. Kamada, A. Leonard, B. Lipschultz, A. Loarte, K. Miyamoto, V. Mukhovatov, T. Osborne, A. Polevoi, and A. Sips, Nuclear Fusion **47**, S1 (2007).

[2] J. Wesson and D. Campbell, *Tokamaks*, Oxford Engineering Science Series (Clarendon Press, 1997).

[3] E. J. Strait, Physics of Plasmas **1**, 1415 (1994).

[4] A. Bondeson and D. J. Ward, Phys. Rev. Lett. **72**, 2709 (1994).

[5] F. Troyon, R. Gruber, H. Saurenmann, S. Semenzato, and S. Succi, Plasma Physics and Controlled Fusion **26**, 209 (1984).

[6] C. M. Bishop, Plasma Physics and Controlled Fusion **31**, 1179 (1989).

[7] R. Fitzpatrick and T. H. Jensen, Physics of Plasmas **3**, 2641 (1996).

[8] A. H. Boozer, Physics of Plasmas **5**, 3350 (1998).

[9] C. Cates, M. Shilov, M. E. Mauel, G. A. Navratil, D. Maurer, S. Mukherjee, D. Nadle, J. Bialek, and A. Boozer, Physics of Plasmas **7**, 3133 (2000).

[10] E. J. Strait, J. M. Bialek, I. N. Bogatu, M. S. Chance, M. S. Chu, D. H. Edgell, A. M. Garofalo, G. L. Jackson, R. J. Jayakumar, T. H. Jensen, O. Katsuro-Hopkins, J. S. Kim, R. J. L. Haye, L. L. Lao, M. A. Makowski, G. A. Navratil, M. Okabayashi, H. Reimerdes, J. T. Scoville, A. D. Turnbull, and D.-D. Team, Physics of Plasmas **11**, 2505 (2004).

[11] S. A. Sabbagh, R. E. Bell, J. E. Menard, D. A. Gates, A. C. Sontag, J. M. Bialek, B. P. LeBlanc, F. M. Levinton, K. Tritz, and H. Yuh, Phys. Rev. Lett. **97**, 045004 (2006).

[12] J. P. Goedbloed, H. A. Holties, S. Poedts, G. T. A. Huysmans, and W. Kerner, Plasma Physics and Controlled Fusion **35**, B277 (1993).

[13] A. Fasoli, D. Testa, S. Sharapov, H. L. Berk, B. Breizman, A. Gondhalekar, R. F. Heeter, M. Mantsinen, and contributors to the EFDA-JET Workprogramme, Plasma Physics and Controlled Fusion **44**, B159 (2002).

[14] H. Reimerdes, M. S. Chu, A. M. Garofalo, G. L. Jackson, R. J. La Haye, G. A. Navratil, M. Okabayashi, J. T. Scoville, and E. J. Strait, Phys. Rev. Lett. **93**, 135002 (2004).

[15] J. M. Hanson, H. Reimerdes, M. J. Lanctot, Y. In, R. J. L. Haye, G. L. Jackson, G. A. Navratil, M. Okabayashi, P. E. Sieck, and E. J. Strait, Nuclear Fusion **52**, 013003 (2012).

[16] M. J. Lanctot, H. Reimerdes, A. M. Garofalo, M. S. Chu, Y. Q. Liu, E. J. Strait, G. L. Jackson, R. J. L. Haye, M. Okabayashi, T. H. Osborne, and M. J. Schaffer, Physics of Plasmas **17**, 030701 (2010).

[17] M. J. Lanctot, H. Reimerdes, A. M. Garofalo, M. S. Chu, J. M. Hanson, Y. Q. Liu, G. A. Navratil, I. N. Bogatu, Y. In, G. L. Jackson, R. J. L. Haye, M. Okayabashi, J.-K. Park, M. J. Schaffer, O. Schmitz, E. J. Strait, and A. D. Turnbull, Physics of Plasmas **18**, 056121 (2011).

[18] T. E. Evans, R. A. Moyer, P. R. Thomas, J. G. Watkins, T. H. Osborne, J. A. Boedo, E. J. Doyle, M. E. Fenstermacher, K. H. Finken, R. J. Groebner, M. Groth, J. H. Harris, R. J. La Haye, C. J. Lasnier, S. Masuzaki, N. Ohyabu, D. G. Pretty, T. L. Rhodes, H. Reimerdes, D. L. Rudakov, M. J. Schaffer, G. Wang, and L. Zeng, Phys. Rev. Lett. **92**, 235003 (2004).

[19] Y. Liang, H. R. Koslowski, P. R. Thomas, E. Nardon, B. Alper, P. Andrew, Y. Andrew, G. Arnoux, Y. Baranov, M. Bécoulet, M. Beurskens, T. Biewer, M. Bigi, K. Crombe, E. De La Luna, P. de Vries, W. Fundamenski, S. Gerasimov, C. Giroud, M. P. Gryaznevich, N. Hawkes, S. Hotchin, D. Howell, S. Jachmich, V. Kiptily, L. Moreira, V. Parail, S. D. Pinches, E. Rachlew, and O. Zimmermann, Phys. Rev. Lett. **98**, 265004 (2007).

[20] R. J. L. Haye, S. Günter, D. A. Humphreys, J. Lohr, T. C. Luce, M. E. Maraschek, C. C. Petty, R. Prater, J. T. Scoville, and E. J. Strait, Physics of Plasmas **9**, 2051 (2002).

[21] F. A. G. Volpe, M. E. Austin, R. J. L. Haye, J. Lohr, R. Prater, E. J. Strait, and A. S. Welander, Physics of Plasmas **16**, 102502 (2009).

[22] J. Scoville, R. L. Haye, A. Kellman, T. Osborne, R. Stambaugh, E. Strait, and T. Taylor, Nuclear Fusion **31**, 875 (1991).

[23] S. M. Wolfe, I. H. Hutchinson, R. S. Granetz, J. Rice, A. Hubbard, A. Lynn, P. Phillips, T. C. Hender, D. F. Howell, R. J. L. Haye, and J. T. Scoville, Physics of Plasmas **12**, 056110 (2005).

[24] R. J. Buttery, A. H. Boozer, Y. Q. Liu, J.-K. Park, N. M. Ferraro, V. Amoskov, Y. Gribov, R. J. L. Haye, E. Lamzin, J. E. Menard, M. J. Schaffer, E. J. Strait, and the DIII-D Team, Physics of Plasmas **19**, 056111 (2012).

[25] A. M. Garofalo, K. H. Burrell, J. C. DeBoo, J. S. deGrassie, G. L. Jackson, M. Lanctot, H. Reimerdes, M. J. Schaffer, W. M. Solomon, and E. J. Strait, Phys. Rev. Lett. **101**, 195005 (2008).

[26] A. J. Cole, J. D. Callen, W. M. Solomon, A. M. Garofalo, C. C. Hegna, M. J. Lanctot, and H. Reimerdes (the DIII-D Team), Phys. Rev. Lett. **106**, 225002 (2011).

[27] A. H. Boozer, Plasma Physics and Controlled Fusion **53**, 084002 (2011).

[28] M. Sankar, E. Eisner, A. Garofalo, D. Gates, T. Ivers, R. Kombargi, M. Mauel, D. Maurer, D. Nadle, G. Navratil, and Q. Xiao, Journal of Fusion Energy **12**, 303 (1993).

[29] A. Garofalo, E. Eisner, T. Ivers, R. Kombargi, M. Mauel, D. Maurer, D. Nadle, G. Navratil, M. V. Sankar, E. Taylor, and Q. Xiao, Nuclear Fusion **38**, 1029 (1998).

[30] J. P. Freidberg, *Ideal magnetohydrodynamics* (Plenum Press, 1987).

[31] G. Bateman, *MHD instabilities* (MIT Press, 1978).

[32] B. Hu and R. Betti, Phys. Rev. Lett. **93**, 105002 (2004).

[33] R. Betti and J. P. Freidberg, Phys. Rev. Lett. **74**, 2949 (1995).

[34] R. Fitzpatrick and A. Aydemir, Nuclear Fusion **36**, 11 (1996).

[35] R. Fitzpatrick, Physics of Plasmas **9**, 3459 (2002).

[36] M. Mauel, J. Bialek, A. Boozer, C. Cates, R. James, O. Katsuro-Hopkins, A. Klein, Y. Liu, D. Maurer, D. Maslovsky, G. Navratil, T. Pedersen, M. Shilov, and N. Stillits, Nuclear Fusion **45**, 285 (2005).

[37] M. E. Mauel and M. Shilov, "Comments on dynamical models for the rwm," (2004), unpublished.

[38] A. H. Boozer, Physics of Plasmas **6**, 3180 (1999).

[39] A. H. Boozer, Phys. Rev. Lett. **86**, 5059 (2001).

[40] A. H. Boozer, Physics of Plasmas **10**, 1458 (2003).

[41] M. Shilov, C. Cates, R. James, A. Klein, O. Katsuro-Hopkins, Y. Liu, M. E. Mauel, D. A. Maurer, G. A. Navratil, T. S. Pedersen, N. Stillits, R. Fitzpatrick, and S. F. Paul, Physics of Plasmas **11**, 2573 (2004).

[42] R. Fitzpatrick and J. Bialek, Physics of Plasmas **13**, 072512 (2006).

[43] J. M. Hanson, *A Kalman Filter for Active Feedback on Rotating External Kink Instabilities in a Tokamak Plasma*, Ph.D. thesis, Columbia University (2009).

[44] J. Bialek, A. H. Boozer, M. E. Mauel, and G. A. Navratil, Physics of Plasmas **8**, 2170 (2001).

[45] D. A. Maurer, J. Bialek, P. J. Byrne, B. D. Bono, J. P. Levesque, B. Q. Li, M. E. Mauel, G. A. Navratil, T. S. Pedersen, N. Rath, and D. Shiraki, Plasma Physics and Controlled Fusion **53**, 074016 (2011).

[46] T. H. Ivers, E. Eisner, A. Garofalo, R. Kombargi, M. E. Mauel, D. Maurer, D. Nadle, G. A. Navratil, M. K. V. Sankar, M. Su, E. Taylor, Q. Xiao, R. R. Bartsch, W. A. Reass, and G. A. Wurden, Physics of Plasmas **3**, 1926 (1996).

[47] A. J. Klein, D. A. Maurer, T. S. Pedersen, M. E. Mauel, G. A. Navratil, C. Cates, M. Shilov, Y. Liu, N. Stillits, and J. Bialek, Physics of Plasmas **12**, 040703 (2005).

[48] J. M. Hanson, B. D. Bono, R. W. James, J. P. Levesque, M. E. Mauel, D. A. Maurer, G. A. Navratil, T. S. Pedersen, and D. Shiraki, Physics of Plasmas **15**, 080704 (2008).

[49] J. P. Levesque, Bulletin of the American Physical Society , BP9.00086 (2010).

[50] T. S. Pedersen, D. Maurer, J. Bialek, O. Katsuro-Hopkins, J. Hanson, M. Mauel, R. James, A. Klein, Y. Liu, and G. Navratil, Nuclear Fusion **47**, 1293 (2007).

[51] I. Hutchinson, *Principles of Plasma Diagnostics* (Cambridge University Press, 2005).

[52] E. J. Strait, J. D. Broesch, R. T. Snider, and M. L. Walker, Review of Scientific Instruments **68**, 381 (1997).

[53] J. Spaleta, L. Zakharov, R. Kaita, R. Majeski, and T. Gray, Review of Scientific Instruments **77**, 10E305 (2006).

[54] J.-M. Moret, F. Buhlmann, D. Fasel, F. Hofmann, and G. Tonetti, Review of Scientific Instruments **69**, 2333 (1998).

[55] D. A. Gates, *Passive Stabilization of MHD Instabilities at High Beta Normal in the HBT-EP Tokamak*, Ph.D. thesis, Columbia University (1993).

[56] B. J. Braams, Plasma Physics and Controlled Fusion **33**, 715 (1991).

[57] O. Klber, H. Zohm, H. Bruhns, J. Gernhardt, A. Kallenbach, and H. Zehrfeld, Nuclear Fusion **31**, 907 (1991).

[58] T. D. de Wit, A.-L. Pecquet, J.-C. Vallet, and R. Lima, Physics of Plasmas **1**, 3288 (1994).

[59] S. Benkadda, T. D. de Wit, A. Verga, A. Sen, A. team, and X. Garbet, Phys. Rev. Lett. **73**, 3403 (1994).